Skolkovo Institute of Science and Technology

RADIATION SHIELDING OF ASTRONAUTS DURING INTERPLANETARY FLIGHTS

Doctoral Thesis

by

MIKHAIL IGOREVICH DOBYNDE

DOCTORAL PROGRAM IN ENGINEERING SYSTEMS

Supervisor
Professor Rupert Gerzer

Moscow - 2019

I hereby declare that the work presented in this thesis was carried out by myself at Skolkovo Institute of Science and Technology, Moscow, except where due acknowledgement is made, and has not been submitted for any other degree.

Mikhail I. Dobynde (Candidate)

Prof. Rupert Gerzer (Supervisor)

Date

Contents

Acknowledgments

The author appreciates all people and teams with whom he made this work, who gave him the possibility to make it and who inspired him on the way. Personally, the author would like to thank

Prof. Yuri Shprits for initiating the overall research, access to Hoffman2 cluster, discussion of the results and help with publications;

Prof. Vyacheslav Shurshakov for initiating the numeric modeling of MATROSHKA-R experiment, discussion of the results and help with publications;

Dr. Alexander Drozdov for his help with coding at the beginning of the research, discussion of the results and help with publications;

Dr. Elena Kronberg and Dr. Mikhail Rashev for collaboration in calculations for RAPID electron spectrometer;

Prof. Rupert Gerzer, for help with thesis manuscript and presentation;

Prof. Anton Ivanov for help while finalizing thesis;

Prof. Henni Ouerdane, Prof. Clement Fortin, Prof. Mikhail Panasyuk for reviewing thesis and constructive criticism;

Dr. Giorgio Baioco and Dr. Ondrej Ploc reviewing thesis, constructive criticism and coming to Moscow to the defense;

Prof. Jeffry Hoffman, Prof. Ju Le, Prof. Frederik Effenberger, Dr. Dominika Boneberg and Sharon Uy for help with reviewing the publications;

Prof. Alexander Shafirkin and Dr. Alexander Kartashov for results discussion;

This work used computational and storage services associated with the Hoffman2 Shared Cluster provided by UCLA's Institute for Digital Research and Education's Research Technology Group.

Abstract

Radiation impact is considered as one of the main concerns for the health of the astronauts during space missions. Two main groups of space radiation: high-energy and low-intense Galactic Cosmic Rays (GCR), low-energy and high-flux Solar Energetic Particles (SEP), and trapped radiation (TR) in the Earth magnetosphere require conflicting strategies to minimize the radiation dose rates to which astronauts are exposed during flight.

The main goal of the present work is to develop a method to significantly reduce radiation exposure of astronauts due to GCR, SEP, and TR during space flights. To achieve this goal, we consider the following problems:

- determination of the optimal combination of launch dates and spacecraft shielding to allow the longest possible mission duration before reaching the radiation dose limit of astronauts;
- calculation of the relative contributions of the different species to the net radiation dose and their dependence on spacecraft shielding;
- quantitive comparison of the radiation environment within a spacecraft, flying inside and outside of the Earth magnetosphere;
- calculation of depth-dose curves for urgent dose assessment and its validation;
- definition of the limitations of the depth-dose method in terms of particle energy and shielding thickness.

We use the GEANT4 Monte-Carlo code and simple spherical model of a spacecraft to calculate particle propagation and dose distribution in the spherical water phantom (a model of an astronaut). This approach allows us to quantify the radiation doses and dose composition and their dependencies on the flight conditions. The main outcomes of the work are as follows:

- The optimal time for the flight to Mars is during the period of a solar maximum in the decay phase, and the optimal aluminum shielding thickness is $\approx$30 g$\cdot$cm^{-2}. These parameters allow about 5.5 years of interplanetary flight duration before reaching the astronauts' career dose limit of 1 Sv.

- Indirectly scattered secondary radiation particles make up to 50% of the net GCR radiation dose in the Blood-Forming Organs (BFO), and up to 90% of the neutron dose. It means that at the spacecraft design stage, adding the extra shielding with hydrogen-reach composite materials in the direction with a large mass concentration can reduce the radiation dose due to the GCR.

- The radiation environment due to GCR inside a spacecraft on the Low-Earth Orbit (LEO) during solar minimum is similar to that in the interplanetary space during solar maximum, if the average spacecraft shielding is greater than 30 g$\cdot$cm^{-2}, although the net CS dose on the LEO is halved.

- The radiation dose distribution on the surface of the phantom, measured in the MATROSHKA-R experiment onboard the ISS, is well reproduced using depth-dose curves calculated in the present work.

- In light of our, we propose an extension of the depth-dose curve methodology to improve predictions of the dose in the near-surface layer of the phantom by taking into account "dose diffusion".

List of publications

Published

- **M.I Dobynde**, Y.Y. Shprits, (2019).
  "Radiation Environment Created With GCRs Inside a Spacecraft",
  Life Science in Space Research, doi.org/10.1016/j.lssr.2019.09.001;

- **M.I Dobynde**, F. Effenberger, D.A. Kartashov, Y.Y. Shprits, V.A. Shurshakov, (2019).
  "Ray-Tracing Simulation of the Radiation Dose Distribution on the Surface of the Spherical Phantom of the MATROSHKA-R experiment onboard the ISS",
  Life Science in Space Research, doi.org/10.1016/j.lssr.2019.04.001;

- E. A. Kronberg M. V. Rashev P. W. Daly Y. Y. Shprits D. L. Turner A. Drozdov **M. Dobynde** A. C. Kellerman T. A. Fritz V. Pierrard K. Borremans B. Klecker R. Friedel, (2016).
  "Contamination in electron observations of the silicon detector on board Cluster/RAPID/IES instrument in Earth's radiation belts and ring current",
  Space Weather, 14(6), 449-462, doi.org/10.1002/2016SW001369;

Under review

- **M.I Dobynde**, Y.Y. Shprits, A.Ivanov,
  "Low-Earth Orbit Radiation Environment As A Test Bed For Long-Duration Flights Outside Of The Earth Magnetosphere",
  under review in LSSR

- **M.I Dobynde**, Y.Y. Shprits, A. Drozdov, J. Hoffman , J. Li,
  "Beating 1 Sievert: Optimal Radiation Shielding of Astronauts in Mission to Mars" submitted,
  under review in Scientific Reports;

List of Presentations

- **M. Dobynde**, A. Drozdov, E. Kronberg, M. Rashev, D. Truner, Y. Sprits (2013), "Instrument response function simulation for CLUSTER RAPID instrument modeled with GEANT4", AGU fall Meeting, San Francisco,USA.
- **M. Dobynde**, A. Drozdov, Y. Sprits (2014), "Time-dependent radiation hazard estimations during space flights", 40th COSPAR Scientific Assembly, Moscow, Russia.
- **Dobynde, M. I.**, Y. Shprits, and A. Drozdov (2015), "Time-dependent radiation dose estimations during interplanetary space flights", Abstract SA43B-2363, AGU fall Meeting, San Francisco,USA, 4-18 December.
- **Dobynde, M. I.**, A. Y. Drozdov, and Y. Y. Shprits (2016), "Radiation equivalent dose simulations for long-term interplanetary flights", Abstract SA41B-2376, AGU fall Meeting, San Francisco, USA, 12-16 December.
- **Dobynde, M.**, A. Y. Drozdov, and Y. Y. Shprits (2014), "Time-dependent radiation dose simulations during interplanetary space flights", Abstract F2.3-0021-18, 42th COSPAR Scientific Assembly, Pasadena, USA, 12-22 August.
- **Dobynde, M.**, A. Y. Drozdov, D. A. Kartashev, Y. Y. Shprits, and V. A. Shurshakov (2018), "Radiation dose simulations for spherical tissue-equivalent phantom used in the MATROSHKA-R space experiment aboard ISS", Abstract F2.3-0008-18, 42th COSPAR Scientific Assembly, Pasadena, USA, 12-22 August.
- **Dobynde, M.**, A. Y. Drozdov, D. A. Kartashev, Y. Y. Shprits, and V. A. Shurshakov (2018), "Advanced depth-dose curves for fast space radiation dose calculation in a spacecraft with complex geometry", Abstract F2.2-0004-18, 42th COSPAR Scientific Assembly, Pasadena, USA, 12-22 August.

List of Symbols

- Q radiation quality factor
- R particle source radius
- r spherical shielding radius
- f radiation particles flux
- E particles energy
- D radiation dose
- δD radiation dose per primary particles
- δT radiation exposure time
- S irradiated surface area
- Δ normalized mean dose deviation used as the criteria for result convergence
- $\mathrm{R}_{\mathrm{Earth}}$ radius of the Earth
- $\mathrm{H}_{\mathrm{ISS}}$ altitude of the ISS
- $\mathrm{R}_{\mathrm{ISS}}$ distance between ISS position and the touchpoint of a tangent line build from the position of the ISS to the Earth
- $\Omega_{\mathrm{shielded}}$ the angular size of the space covered with the Earth as seen from the ISS

Abbreviations

- ACE Advanced Composition Explorer
- BFO Blood Forming Organs
- CME Coronal Mass Ejections
- CREME Cosmic Ray Effects on Micro-Electronics code
- CS Circulatory System
- DLR Deutsches Zentrum fur Luft (German Space Agency)
- DNA DeoxyriboNucleic Acid
- EVA ExtraVehicular Activity
- FLUKA FLUktuierende KAskade code
- GCR Galactic Cosmic Ray
- GEANT GEometry ANd Tracking code
- GOES Geostationary Operational Environmental Satellite
- HEAO High Energy Astrophysical Observatory
- HZETRN High-(Z)charge Energy (HZE) TRaNsport code
- ICRP International Comission onRadiobiological Protection
- IMP Interplanetary Monitoring Platform
- ISS International Space Station
- LEO Low-Earth Orbit
- LET Linear Energy Transfer

- LIS Local Interstellar Spectrum
- MATROSHKA(-R) experiment onboard the ISS aiming measurements of radiation dose distribution in the astronauts phantom
- MCNP Monte-Carlo N-particle code
- NASA National Aeronautics and Space Administration
- OLTARIS On-Line Tool for the Assessment of Radiation in Space
- PHITS Particle and Heavy Ion Transport System code
- RBE Relative Biological Effectiveness
- SAA South Atlantic Anomaly
- SHIELD Monte-Carlo Code for Simulating Interaction of High Energy Hadrons with Complex Macroscopic Targets
- SOHO Solar and Heliospheric Observatory
- SPENVIS SPace ENVironment Information System
- TE Trapped Electrons
- TP Trapped Protons
- TR Trapped Radiation

List of Figures

Chapter 1

Introduction

1.1 Radiation environment in space

The radiation environment in the inter-planetary space is different compared to the surface of the Earth. It is mainly formed by high-energy protons, electrons, and fully ionized ions. The radiation environment changes according to the solar cycle activity. The radiation environment composition also differs in different regions. In the near-Earth space outside the magnetosphere, the radiation environment is formed by GCR and SEP. On LEO, the radiation environment consists mainly of Trapped Protons (TP), Trapped Electrons (TE), and GCR. All radiation particle spectra in this section are presented as convenient differential flux and as binned integral flux, which is much more informative for the current research. The reason is that, finally, we are interested in the number of particles with kinetic energy within a certain rage. If the entire energy range is relatively small, for example, between 1 and 500 MeV$\cdot$nucleon^{-1} ad in the case of TP, the linear energy scaling can be used. In this case, both differential and binned integral flux spectra look identical. In the current research, consider a large energy range between 1 and 10^5 MeV$\cdot$nucleon^{-1}. Thus the logarithmic scale is used. Since the input information for dose calculation is the number of particles within a certain rage, the binned integral flux provides better information than the convenient differential flux. The notable thing is that the maximum in differential spectra is usually at lower energy than the corresponding maximum in binned integral spectrum.

1.1.1 GCR in the interplanetary space

GCR are particles originate from the interstellar medium and accelerated to high-energies in interaction processes with inhomogeneities of the interstellar magnetic

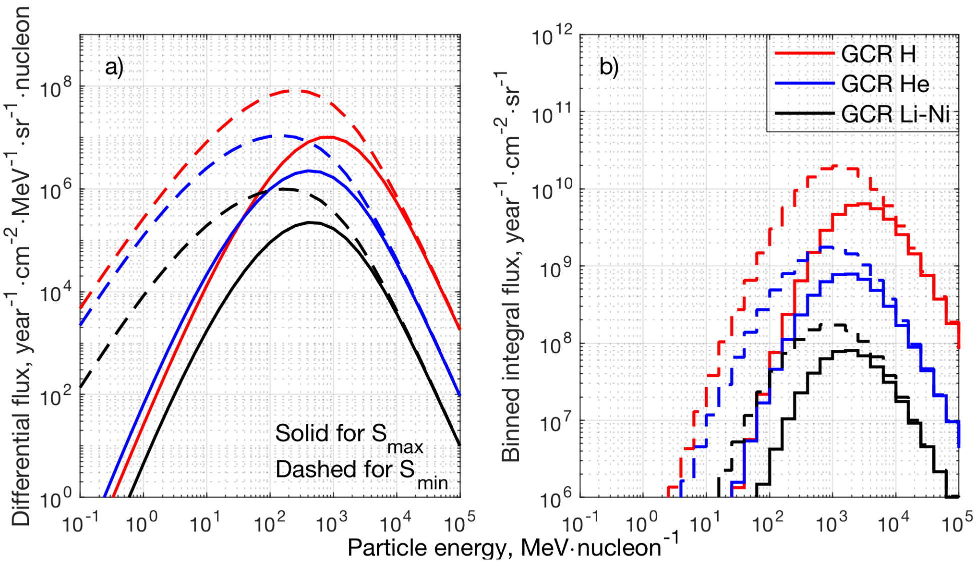

Figure 1.1: Differential (a) and binned integral (b) GCR spectra in the interplanetary space near the Earth during the period of solar max (solid curves) and solar min (dotted curves) described with Matthiä et al., 2013 model. Spectra for different particle species are shown in different color according to the legend.

field (Fermi, 1949). GCR particles are fully ionized ions, consisting of ≈86% protons and ≈12% alpha particles. Heavy ions (high charge (Z) and energy (E) (HZE) particles) make up to only 2% of the GCR flux. Most abundant HZE are B, C, N, O, Si, and Fe ions. The GCR consists of primary GCR and secondary GCR that are the result of the interaction of primary GCR with the matter in space (Zirakashvili, 2014). GCR propagate inside the heliosphere and form spatially homogeneous and angularly isotropic particle flux in the near-Earth interplanetary space.

The ability of GCR particles to propagate inside the heliosphere depends on their rigidity and the configuration of the heliosphere magnetic field, which changes according to the solar activity. The 11-year periodicity in solar activity was first discovered by Heinrich Schwabe in the evolution of sunspot numbers. Forbush, 1958 was the first who studied the dependence of GCR strength on solar activity. An increase in solar activity increases the solar wind strength as well as the occurrence rate of Coronal Mass Ejections (CME), both carriers of the embedded magnetic field. This increase results in an increase of modulation potential of the magnetic field in the heliosphere (Rahmanifard et al., 2017) that leads to GCR flux decrease. The situation is opposite during periods of solar activity minimum. The period between the nearest maxima in GCR flux is 11 years. There is an asymmetry in the GCR flux time evolution related to the orientation on Sun magnetic field. The period of solar activity maximum associated with upward orientation on the Sun magnetic moment is longer. The period of sun magnetic moment rotation is 22 years. At a larger timescale, there exists an 80 years Geilberg periodicity in large SEP events, which was discovered analyzing periodical enhancements of nitrogen deposition in polar ice core (Mccracken, 2001b; Mccracken, 2001a). Some minima in Geilberg periodicity correlate with Mauder (around 1700), Dalton (around 1800), and Gleisberg (around 1900) minimum in the evolution of sunspot number. Recent studies conclude that in our epoch, solar activity decreases, and we are approaching next "Mauder"-like minimum. This is an issue of concern for upcoming space missions because GCR fluxes during this period would be higher (Schwadron et al., 2014; Schwadron et al., 2018; Kuznetsov, Popova, and Panasyuk, 2017).

Figure 1.1a shows the differential spectra of different components of GCR in the near-Earth interplanetary space during the 2001 solar max and the 2010 solar min calculated with Matthiä et al., 2013 model. The GCR energy is usually presented in the units of MeV·nucleon^{-1}, also because of driving with the heliosphere magnetic field. The "low"-energy part of GCR spectra is more sensitive to changes in the heliosphere magnetic field; thus, variations with the solar activity are larger, comparing to the "'high"-energy part of the spectra. Fluxes of GCR particles with an energy higher than 400 MeV·nucleon^{-1} decrease by a factor of two during the period of solar activity maximum. The difference in modulation results in a variation of the position of the maximum of GCR spectra, namely, shifting to higher energies during solar maximum. Besides evolution associated with solar activity, there might be local short-time GCR variations, for example, a decrease in GCR flux after SEP passing. The intense flux of SEP coupled with the magnetic field increases modulation potential, thus reducing the GCR along its trajectory. It takes several days for GCR to relax to its initial level after SEP passing.

"Low"-energy GCR ($<$ 1000 MeV·nucleon^{-1}) have been studied with satellite missions like the Interplanetary Monitoring Platform (IMP) and Advanced Composition Explorer (ACE). Data on "high"-energy GCR (> 1000 MeV·nucleon^{-1}) was collected in High Energy Astrophysical Observatory (HEAO) missions and balloon missions like JUL and ORTH. Many data about GCR come from the measurements in the atmosphere, where high-energy GCR induce showers of secondary particles. These secondary particles can be detected with good accuracy using on-ground neutron monitors or balloon experiments. Neutron monitor measurements started in the thirties, and now there is a spread network of neutron monitors, covering the vast region of latitudes. However, for the reconstruction of the GCR spectra in the near-Earth interplanetary space, the most valuable are high-latitude monitors (IZMIRAN, OULU). The reason is that GCR are less disturbed by the Earth magnetic field in this region.

GCR spectrum Outside of the heliosphere is called Local Interstellar Spectrum (LIS). LIS can be described in several ways, one of which is a power-law:

$$j_{\mathrm{LIS}}(E) = j_0 \beta^{\delta} (E + E_0)^{-\gamma} \tag{1.1}$$

where E is particle kinetic energy per nucleon, E_0 is the rest mass per nucleon, and β is particle velocity relative to the speed of light. Coefficients j_0 and γ are defined using "high"-energy measurements data and δ is defined using "low"-energy data.

Propagation of GCR inside the magnetosphere is usually described with the Fokker-Planck equation that considers GCR diffusion, convection, and adiabatic deceleration inside the heliosphere. Solar activity is included in the model with modulation parameter (potential), which is proportional to particle rigidity necessary to penetrate in the heliosphere. The modulation parameter can be determined in several ways. The most convenient is using data on the radiation environment around the Earth and using data on solar activity. The advantage of deriving modulation potential from radiation environment around the Earth is that it provides actual data, which is important if there are local time-dependent variations that are hard to be described precisely, like variations due to SEP passing, which are very hard to describe. The main advantage of using solar activity parameters like sunspot number is the ability to predict modulation potential. The reason is the time lag between changes in solar activity and the state of the heliosphere (Nymmik, 2000). For the 1 AU distance, this lag is varying from 8 up to 14 months, depending on the phase of solar activity and the particle rigidity. The prediction can be extended to larger time scales using predictions for sunspot number (Norbury, 2011; Petrovay, 2010; Shepherd, Zharkov, and Zharkova, 2014; Zharkova et al., 2015).

The most common are NASA Badwhar-O'Neill (BON) model (O'Neill, 2010; Golge, O'Neill, and Slaba, 2015), SINP (Nymmik) model (Nymmik et al., 1992; Nymmik, Panasyuk, and Suslov, 1996), and DLR model (Matthiä et al., 2013). The main advantage of the BON model is the frequency of updating of the model coefficients according to new data and better coverage of the "low"-energy part of spectra. Nymmik model included time-lag and was driven with sunspot number. However, latter modifications of these models implemented best from each other and now are more or less similar. DLR model is based on simplified Nymmik with time lag excluded, but the coefficients were calculated using latest measurements data available at the date of publication, so it describes the period between 1997 and 2005 with high accuracy.

1.1.2 SEP in the interplanetary space

The second main component of the interplanetary radiation environment are SEP, which are ejected from the Sun during solar flares. Particle flux in these events is mostly formed by protons, although there are there is a minor ion component. Unlike GCR, SEP spectra have a maximum at ≈1 MeV and decrease exponentially (Nymmik, 1996) with the energy increase. Data on SEP spectra is usually provided up to 1 GeV·nucleon^{-1}. After SEP is ejected from the Sun surface, it propagates along magnetic field lines, so the SEP track is twisted in the ecliptic plane, and particle spectra vary along SEP track (Forstner et al., 2019). Particle spectra during these events in the interplanetary space are mainly measured by Solar and Helio-

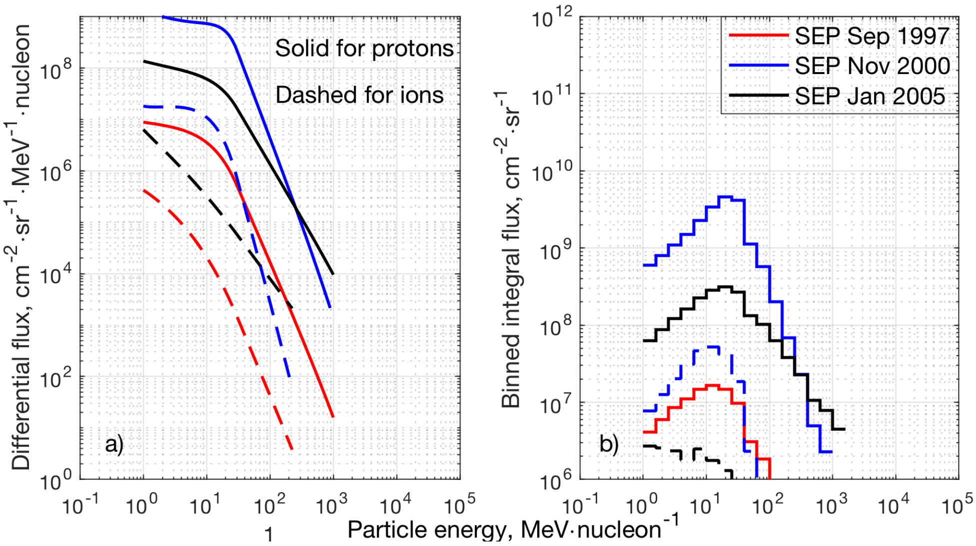

Figure 1.2: Differential (a) and binned integral (b) SPE spectra for September 1997, November 2000, and January 2005 events measured with GOES satellite. The data is taken from SINP, 2015.

spheric Observatory (SOHO) and GOES missions.

SEP events are spontaneous. Their probability increases during the maximum of solar activity. Prediction of the SEP event timing, strength, and direction is an extremely challenging task, as the dynamics of the active regions on the Sun and flare generation are not fully understood. A statistical study by Nymmik, 1999 provides a relatively accurate estimate of the frequency of occurrence and strength of SEP events. The model can be used to estimate the radiation dose during a given period. An alternative, but also a complicated way, is early alarm systems that analyze SEP events close to the Sun and then predict its location and strength for more distant areas. To describe SEP, we use spectra of the largest SEP events from August 1997 to 2006, obtained with instruments on the Geostationary Operational Environmental Satellite (GOES) and the Advanced Composition Explorer (ACE) satellite (SINP, 2015).

1.1.3 GCR on LEO

GCR spectra on LEO differ from spectra in the near-Earth interplanetary space. The magnetic field of the Earth deflects low-energy GCR particles. LEO GCR

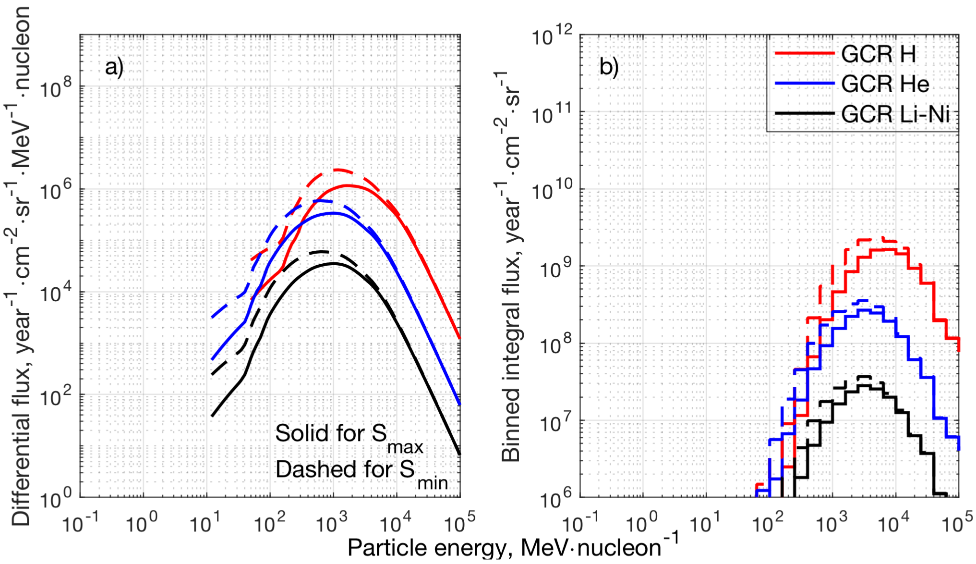

Figure 1.3: Differential (a) and binned integral (b) GCR spectra on the LEO during the period of solar max (solid curves) and solar min (dotted curves) described with Tylka et al., 1998 model. Spectra for different particle species are shown in different color according to the legend.

spectra have a maximum at 1 GeV·nucleon^{-1}. GCR spectra vary with altitude and latitude along the spacecraft trajectory. GCR fluxes at the ISS vary during each turn because the ISS orbit has an inclination of 56 degrees. GCR flux is maximal near the poles and minimal at the equator. In the current research, GCR spectra were taken from SPENVIS, for the actual ISS orbit.

1.1.4 Trapped radiation on the LEO

Trapped radiation is an important component of the radiation environment on LEO. It mainly consists of protons and electrons, which are trapped with the Earth's magnetic field and form radiation belts around the Earth. The stable trapping region is inside ≈7 R_E, while quasi-trapped region extends up to ≈12 R_E. The highest energy of trapped protons is ≈500 MeV, and ≈10 MeV for trapped electrons. Particles with higher energy cannot be trapped for a long time with the magnetic field of Earth. The movement of trapped particles in the radiation belts consists of spinning around magnetic field lines, movement along the magnetic field line between mirror points, and west-east drift around the Earth. The energy and spatial distribution of trapped particles are not homogenous. It is convent to describe trapped parti-

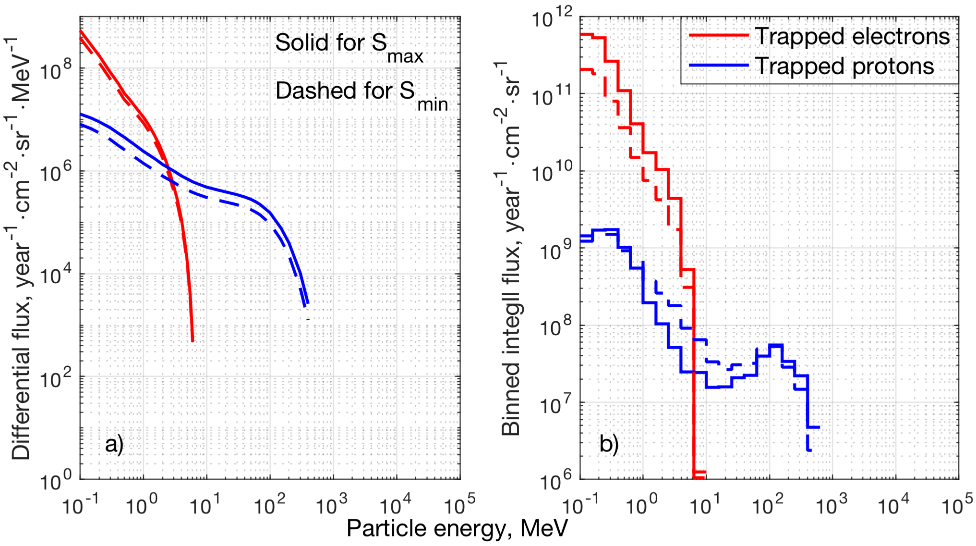

Figure 1.4: Differential (a) and binned integral (b) TR spectra averaged over the ISS orbit during the period of 2001 solar min (solid curves) and 2010 solar max (solid curves). Trapped protons (blue curves) are described with AP8 (M. Sawyer and I. Vette, 1977) and trapped electrons (red curves)- with AE8 (I. Vette, 1991) model.

cle distribution as L-shell (McIlwain, 1961) population and pitch-angle distribution, both depending on the particle energy. The pitch angle is an angle between particle momentum and magnetic field line at the geomagnetic equator. The L-shell is the surface of the geomagnetic potential. The distribution of trapped radiation in geodesic coordinates is not symmetric because of the shift of the magnetic dipole of the Earth respective to the center of the Earth. One of the consequences is the South Atlantic Anomaly (SAA)- region over Brazil and the western part of the Atlantic Ocean, where radiation comes closer to the Earth surface that in other regions. The SAA drifts north-west with the speed of 0.3° per year.

Because of the interaction of radiation particles with the atmosphere, there appears east-west asymmetry in particle fluxes. The atmosphere density decreases with the altitude, so trapped protons, which gyrate in the upper hemispace, are less attenuated, comparing to trapped protons, which gyrate in the down hemispace. Trapped protons from the upper hemispace come to the point of interest from the west direction, so trapped proton flux from the west is stronger than from the east. The asymmetry in the flux increases with the energy of the proton because the gyroradius increases with the energy, leading to an increase in the total thickness of the atmosphere along particle track and associated energy losses. During solar max, the asymmetry in the fluxes increases, due to the atmosphere expansion, which is caused by extra heating.

The solar cycle also influences the repopulation of the radiation belts. One of the mechanisms of the repopulation is trapping protons and electrons, which are produced when albedo neutron decay. The albedo neutrons are produced by GCR, which increase during the period of solar max.

The measurements of trapped radiation have started since the beginning of the space era in 1958. The first models (maps) of trapped radiation were a series of AP and AE models. They were created for certain energy ranges. Finally, they were summarised in AP8 and AE8 models, which described trapped particle fluxes during periods of solar max and solar min (Sawyer and Vette, 1976; Vette, 1991a; Vette, 1991b; Fung, 1996). This model was intensively used in space engineering for many years. Recently the next version AP9 and AE9 were presented (Ginet et al., 2013) and can be implemented now (Badavi, 2014). However, in the current work, AP8 and AE8 models are used because of their availability via SPENVIS web-site. The reason is that ISS orbit inclination is 51.63°, resulting in crossing different L-shells. SPENVIS facility allows getting trapped particle spectra averaged over the orbit, which was done using parameters of actual ISS orbit. The interpolation for the intermediate time points between solar max and solar min can be done as linear, sin-like, and according to sunspot number. In the current research, the AP8/AE8 model data was taken from SPENVIS for the actual ISS orbit. The interpolation was done according to the sunspot number.

In the continuation of the research procedure of converting orbital parameters into L-shell should be created, which would allow usage of the recent radiation environment models in more convenient way.

1.1.5 Other radiation sources

The radiation environment is also influenced by the solar wind, by albedo radiation that was backscattered from the atmosphere of the Earth, by Anomaly Cosmic Rays and other sources. We assume that their intensity is either very low, so their contribution to the radiation doses is much smaller compared to GCR, SEP, and TR, or particle energies are so low that they can be effectively stopped by 0.1 g$\cdot$cm^{-2} shielding.

1.2 Biological effects of space radiation

The radiation impact can be quantified with the absorbed dose, biologically weighted dose, dose equivalent, equivalent dose, and effective dose values. Absorbed dose is measured in units of gray (symbol: Gy). It is equal to the energy deposited by radiation in a volume (expressed in units of a joule) divided by volume mass (expressed in units of a kilogram). The absorbed dose is used to characterize the radiation impact on materials and system of a spacecraft.

The biological impact of radiation cannot be characterized by the absorbed dose, because the same absorbed dose deposited by different particles or with particles with different energies produce a different impact on biological tissues. That is because of differences in ionization density distribution created along the particle track, the difference in track structure, and differences in the biological response of different tissues and cells. In the radiobiology studies, the effect of radiation dose on cell cultures or animal models is characterized by the biologically weighted dose that is equal to the absorbed dose value multiplied by relative biological effectiveness (RBE). RBE depends on exposure rate, particle species, energy, and expected effect.

For radiation protection, the equivalent dose and the dose equivalent were introduced. They both are measured in units of sivert (symbol: Sv). The equivalent dose is calculated for each particle that enters the biological object. It is equal to the net deposited dose due to the particle and all induced particles multiplied by the radiation weighting factor w_{R} (ICRP, 1991; ICRP, 2007). The radiation weighting factor differs for different particle species and depends on the particle kinetic energy at the surface of an anthropomorphic phantom. The radiation weighting factors are determined using RBE data and represent the "worst-case" estimation of the radiation effect on a human. The last version of radiation weighting factors was introduced in ICRP recommendations (Petoussi-Henss et al., 2010).

The dose equivalent is used when there is a need to characterize the effect of "mixed radiation fields"- the radiation environment with a complex composition of particles with different particle and species. An example of such a radiation en-

LET	Q
LET<10	1
10≤LET≤100	0.32·LET-2.2
LET>100	$300/\sqrt{\mathrm{LET}}$

Table 1.1: Quality factor for different LET (ICRP, 1991)

vironment is one inside a spacecraft during the out-of-magnetosphere flight. The dose equivalent calculation requires modeling the full track of the particle inside the biological object, including all tracks of induced particles. The dose equivalent for charged particles is calculated for each segment of particle track multiplying the deposited energy by the radiation quality factor Q recommended by ICRP (ICRP, 1991). It depends on the linear energy transfer (LET) value (Table 1.1). LET is equal to the deposited energy density along the particle track in units of keV$\cdot\mu$m^{-1}. It is assumed that LET is proportional to the ionization density along the particle track. The LET varies in different parts of particle track, depending on particle energy, particle species, and medium characteristics. The major part of ionization due to gamma-rays and neutrons is associated with the secondary charged particles. For this reason, the ionization of gamma-rays and neutrons is called "indirect ionization". Neutrons do not have charge, thus they are able to collide with atom nuclei, producing protons, neutrons, and nuclei fragments. The ionization losses of induced protons and nuclear fragments maximize, when they are slowed down (the Brag peak, see Figure 3.6), so the LET and associated biological effect of the absorbed dose increases. Gamma-rays also ionize the medium, but most of the secondary particles are electrons from the outer shells. The energy losses of the electrons are monotonic and do not increase with the decrease in kinetic energy, so the quality factor is equal to 1.

Different organs have different sensitivity to the same radiation dose. Differences in organs' sensitivity are associated with differences in the significance of the organ for organism functioning and recovering potential, which is high for skin and almost absent in the brain. Radiation sensitivity is increased with stress, associated with microgravity conditions, for the Circulatory System (CS) and red bone marrow tissue, which is BFO. The effective dose was introduced to characterize the net damage to an organism. It is equal to the sum of equivalent dose or dose equivalent deposited in critical organs multiplied by organs' weighting factors. The sum of all organs' weighting factors is equal to 1.

Space radiation influence on the organisms can lead to deterministic or stochastic effects. Deterministic effects occur after short-time high-dose irradiation. They increase the risk during a space mission, as astronauts can lose the abilities which are important for mission running. Stochastic effects are caused by long-term low-dose irradiation. They increase the risk of post-flight illnesses like cancer, cataract, damage to reproductive functions, and associated life-shortening. The dose career limit for astronauts depends on astronauts' sex and age. The career limits increase with age and are higher for male astronauts.

1.2.1 Radiation doses due to the secondary neutrons

Among different species of secondary radiation particles, special attention is focused on secondary neutrons. Secondary neutrons are produced in inelastic scattering processes when incoming space radiation particles (mostly GCR, because of the high energy) interact with the target nucleus. Uncoupled neutrons have a relatively short lifetime of $\approx$900 seconds. A neutron decays on a proton, electron, and electron antineutrino. For these two reasons, neutron fluxes in space are significant in close vicinity of massive space objects or inside the spacecraft. Secondary neutrons do not have charge and associated ionization losses. For this reason, they can propagate deep into the tissues keeping high kinetic energy and induce damage to the inner organs. Neutrons ionize a medium differently than charged particles. They produce charged particles, interacting with the medium atoms, which ionize the medium. Such a mechanism is called “indirect” ionization. Most of the neutron dose is due to induced protons; the rest of the dose is due to induced gamma rays, electrons, alpha particles, and heavier ions. Detectors of secondary neutrons are different from charged particle detectors. Commonly they are based on scintillatora medium that produces flares with certain emission spectra that are detected with a photomultiplier tube or convenient photodiode.

1.3 Radiation exposure limits

Dose equivalent values are used in space agency policies of different countries to regulate astronauts' activity. One of the branch marks is the effective dose of 1 Sv. Russian Space Agency uses it as a career limit for the whole body exposure (RSA, 2004), which guarantees total radiation risk at the level of 10%. Although the limit is defined for the effective dose, a conservative estimation can be done calculating the dose equivalent averaged over the phantom (Grigoriev et al., 1983). The over-estimation, in this case, would be ≈10-15%. In NASA regulations (NASA, 2015) exposure limits are defined for cancer-induced mortality in values of effective dose (these limits depend on mission duration and astronauts age and sex and keep the probability of the radiation-induced death within 3% level with the confidence of 95%) and for non-cancer effects. The overall astronauts' exposure should fulfill all the requirements. For example, the career limit for CS, which is determined for RBE-weighted absorbed dose, is 1 Gy·Eq. The RBE-weight factors are different from Q(LET) factors implemented for dose equivalent calculations. Thus the direct comparison can not be made. However, since Q(LET) factors have been calculated using RBE-weight factors in case of low-rate exposure and taking into account uncertainties in dose calculations and measurements, 1 Sv in CS can be referred to as an estimation of career exposure limit. We will use 1 Sv dose equivalent value to analyze an interplanetary flight, although the limit is established for the low-Earth orbit missions. The reason is the absence of regulations for upcoming interplanetary flights and recent results (Zeitlin et al., 2019) that demonstrate the similarity of the radiation environment on the low-Earth orbit and in the interplanetary flight. If the dose limits would be reduced in future, the results presented in this work can be easily used to estimate new limits of the mission duration, while conclusions about the optimal flight conditions would be the same.

1.4 Numerical dose assessment

Numerical methods are a powerful tool for radiation dose predictions. The main difference between methods is in the approach to geometry simplification. They can be separated by the next large groups. The first group includes ray-tracing methods. The main advantage is low calculation time. The main disadvantage is low accuracy compared to other methods. The second group is Monte-Carlo based methods. They provide more detailed information on radiation dose and radiation environment. Also, electric or magnetic fields can be included in this model. The main disadvantage is that simulation time increases with the geometry complexity increase. Some methods try to combine stages used by the first two methods in an attempt to increase accuracy, keeping simulation time the same.

1.4.1 Monte-Carlo methods

Monte-Carlo code uses random numbers and probability distributions to obtain a close approximation to the exact solution. In a single Monte-Carlo simulation, the propagation of one particle through a geometry model is calculated. Particle-mater interactions are described by interaction cross-sections. This approach can be used for simulation of particle propagation through complex geometries described by voxels. The main disadvantage of Monte-Carlo calculations is a large number of simulation runs needed to model a realistic radiation environment. Simulation time increases with the increase of geometry model resolution. Primary particles with high kinetic energy produce a large number of secondary particles, and their propagation should also be calculated, thus increasing calculation time. There are many Monte-Carlo codes that are applied for space radiation modelling: FLUKA (Olsher, 2006), GEANT4 (Agostinelli et al., 2003), MCNP6 (Pelowitz et al., 2013), PHITS (Sato et al., 2017; Sato et al., 2018) and SHIELD(Dementyev and Sobolevsky, 1999). Their predictions are often intercompared, and generally, they provide more or less the same results. However, they have individual specifics, so researcher should clearly understand his needs to make the optimal choice.

1.4.2 Deterministic transport codes

Deterministic transport codes use time-independent linear Boltzmann equations for flux density of particles of certain species. The main advantage of such codes is low simulation time. The most advanced and well known in space radiation research in NASA High charge (Z) and Energy TRaNsport (HZETRN) code (Wilson et al., 2016). It can be used for radiation dose calculation in a multi-layer structure, or in a geometry model, which consists of simple shape objects.

1.4.3 Ray-tracing methods

In ray-tracing, radiation doses are calculated at the respective point of interest. Realistic geometry around the selected point is processed into shielding distribution function. This is done by building many rays from the point of interest in all directions. Then material and thickness composition along each ray is defined. The material and thickness composition can be used as it is or processed to one equivalent material (usually aluminum or polyethylene) using scaling coefficients. Next, the radiation dose is calculated in a thin detector layer (usually water) placed behind layer shielding. The layer thickness repeats shielding along each ray. The radiation dose is calculated by the transport code or Monte-Carlo code.

Chapter 2

Literature review

2.1 Radiation exposure on the way to Mars

Exposure of astronauts to space radiation is one of the major barriers to human exploration of the solar system and long-duration human space (Cucinotta et al., 2013; Zeitlin et al., 2013; Hassler et al., 2014a). In LEO, astronauts are protected from high-energy charged particle radiation by the magnetic field of the Earth. Outside of the magnetosphere, the spacecraft is exposed to particle radiation originating from the Sun, distant stars, and galaxies.

There are two main types of cosmic radiation inside the solar system: GCR and SEP. GCR particles originate from the interstellar medium and diffuse inside the heliosphere, forming a spatially homogeneous and angularly isotropic particle flux. GCR are fully ionized ions, consisting of 84% protons and 14% alpha particles. HZE particles make up only 2% of the GCR flux (Nymmik et al., 1992). SEP are ejected from the surface of the Sun during solar flares and propagate outwards into the solar system. SEP consist mostly of protons.

Both GCR and SEP intensities depend on the 11-year solar cycle. During solar minima, GCR fluxes increase, and during solar maxima, GCR are lower. Unlike persistent GCR radiation, SEP events are spontaneous. SEP event probability and intensity decrease during solar activity minima and increase during its maxima. Different SEP events have different risk levels for space missions because of the differences in particle spectra. Hu et al., 2009 have shown that no single event would lead to acute radiation death if the aluminum spacecraft shielding exceeds 5 g$\cdot$cm^{-2}. Thus, most risk due to SEP is associated with extravehicular activity (EVA). However, dose calculations with SHIELD code (Denisov et al., 2010; Kuznetsov et al., 2012; Denisov et al., 2011), which use the statistical model by Nymmik, 1999 for SEP description, provide much higher values of the radiation dose, which can lead to the acute effects on the astronaut's health. Almost all space agencies have prototypes of radiation protection garment, the most recent are AstroRad by NASA (Gaza, 2018) and PRESEO by the Italian Space Agency (Vuolo et al., 2017 and Baiocco et al., 2018). For radiation protection of crewed missions during solar flares, NASA also consider the creation of extra shielded areas during flight using onboard equipment.

Despite the relatively low fluxes of GCR particles, long exposure times to constant background radiation of GCR can result in a significant total radiation dose accumulated during the entire flight, resulting in dangerous biological effects. Shielding from GCR is a challenging task due to the high energies of the particles (Figure 1.1). The high kinetic energies of particles result in high penetration ability and in a large amount of energy being deposited in tissues and organs. Besides, high-energy particles produce significant amounts of secondary particles while propagating through the spacecraft shielding due to nuclear interactions with the shielding materials. These secondary particles propagate into the spacecraft interior and increase the radiation dose. The number of secondary particles and associated radiation damage is higher for shields made of materials with high atomic number (Z) elements, even if the shield surface densities are the same. For example, it has been shown experimentally that for 10^3 MeV·nucleon^{-1} iron ions, the radiation damage is reduced for low-Z materials such as polyethylene, and increased for high-Z materials such as lead (Durante and Kronenberg, 2005).

The dependence of the GCR dose on the shielding thickness is not monotonic. The results of simulation (Slaba, Mertens, and Blattnig, 2013) performed with the HZETRN code (Wilson et al., 2014; Wilson et al., 2015) for a point in the center of shielding sphere have shown that in the interplanetary space, the dependence of dose equivalent on the aluminum shielding thickness has a local minimum at 40 g·cm^{-2}. In recent calculations (Slaba et al., 2017) of the radiation dose in 1 mm thick water slab, placed between two plates of aluminum shielding, the minimum was found at 20 g·cm^{-2}. The results of the same calculations (Slaba et al., 2017) performed for a

30 cm water slab show monotonic decay of the radiation dose with the increase of shielding thickness without local minimum.

While most studies performed with HZETRN are focused on the thickness dependence of the dose for a specific phase of the solar cycle, the GCR dose evolution between 1997 and 2014 was calculated (Mrigakshi et al., 2013) with the GEANT4 Monte-Carlo code. The simulation shows a local minimum in the thickness dependence of the dose equivalent at 10 g$\cdot$cm^{-2} during 2001 solar maximum and an absence of such a minimum during the 2010 solar minimum. The simulations were performed for a 25 cm spherical water phantom placed in the center of a spherical aluminum shell.

The geometry used for dose calculations has a significant influence on the result of the calculations. All studies looking for optimal shielding simplify the actual geometry to a model. The most common simplifications for the homogeneous shielding are slab shielding geometry and spherical geometry, with spherical shielding layer and spherical water phantom inside it. However, spherical shielding looks more preferable for calculating radiation doses due to GCR. The first reason is that in the spherical geometry the "nominal" shielding thickness is passed only by particles that propagate toward the center of the shielding. However, the majority of the particles propagate in different directions. The "actual" shielding thickness for them would be higher, comparing to particles propagating to the center. Thus, the energy loss of primary particles and the production of secondary particles would be higher. For example, HZETRN calculations (Barthel and Sarigul-Klijn, 2019) show that the particle flux behind slab and spherical shielding would be different.

Previous studies of the radiation dose composition (Ballarini et al., 2006) were focused on the shielding range from 0 to 10 g$\cdot$cm^{-2}. In the current research, we would cover a broader range of thickness up to 60 g$\cdot$cm^{-2} for spherical geometry setup and up to 300 g$\cdot$cm^{-2} for slab geometry setup.

Spatial attention in radiation protection is always paid to secondary neutrons. The number of secondary neutrons increases with the shielding thickness (Ballarini et al., 2006; Trovati et al., 2006). One of the ways to reduce the neutron dose is by adding neutron absorber like ^{10}B. For 1 GeV protons Loffredo et al., 2018 have recently shown ≈14% reduction in secondary neutron spectra by adding 10% of ^{10}B to 20 g·cm^{-2} of Nomex shielding. However, the maximum in the absorption of the neutrons with ^{10}B is for thermal neutrons, and besides, the flux of alpha particles increases.

The spherical water phantom is a convenient (Wilson et al., 2015;Mrigakshi et al., 2013;RSA, 2004) simplification of human phantom. The main advantage is that one set of calculations provides dose distribution inside the phantom, and the effect of self-shielding is taken into account. Radiation doses at different depths can be attributed (Matthiä, Berger, and Reitz, 2013) to the radiation doses in anthropomorphic phantom, according to the average shielding value. Radiation doses calculated in thin water slab behind different shielding (so-called depth-dose curves) can be used itself only as an estimation of skin dose because the effect of body self-shielding is neglected. This is well demonstrated with HZETRN calculations (Slaba et al., 2017) when a local minimum is seen in dose dependence on thickness calculated for a 1 mm water slab detector and is absent in case of 30 cm water slab detector. The importance of depth-dose curves is that they are used as the input data for shielding function methodology of radiation dose calculation.

Most previous studies provide estimations of the radiation doses during solar cycle activity maxima or minima, and during the strongest SEP events. Several studies () consider radiation doses during 500 and 1000-day flights according to NASA plans (Drake, Hoffman, and Watts, 2009). However, there is still no clear answer about optimal flight conditions that would enable the longest mission duration. In this study, we present the net radiation doses from SEP and GCR radiation as an accumulated dose during a spaceflight, dependent on flight duration and launch date for the solar cycle between 1998 and 2006. For this purpose, using GEANT4 Monte-Carlo code, we calculate radiation dose distribution inside spherical water phantom and dependence of the dose and dose composition on the flight conditions (thickness of spherical aluminum shielding and phase of solar cycle). We show that the minimum radiation dose will be obtained for a flight started during solar maximum behind an aluminum shield with a thickness of 30 g$\cdot$cm^{-2}. Furthermore, we demonstrate that a local minimum in the dependence of the dose equivalent on the thickness of shielding is present during solar maximum and a further increase in shielding beyond this minimum results in an increase in dose equivalent.

2.2 Reproducing space radiation environment

GCR particles have high kinetic energies, which allow them to pass through the shell of a spacecraft and produce a lot of secondary particles inside the spacecraft. High-energy GCR particles can be stopped only with an unreasonably thick (higher than 100 g·cm^{-2}) spacecraft shielding (Dobynde et al., 2019). An increase of the shielding up to 200 g·cm^{-2} results in an increase of the secondary particle flux and associated radiation dose rates for the astronaut. The biological influence of GCR radiation is not fully understood because it is impossible to reproduce the same irradiation conditions on the Earth as in the interplanetary space.The first reason is that the flux of primary and induced particles inside the spacecraft is very complex to be reproduced with accelerator facilities. The second reason is that GCR dose rates are low ($\approx$1.2 mSv·day^{-1}) and irradiation elongates during the entire flight. The accelerator provides short-time irradiation in one or a few sessions with an approximate dose of 20 cSv per session. A short irradiation time results in a different organism reaction and reparation mechanisms, thus distorting the model of the space environment. The second reason is that on-ground experiments exclude the influence of microgravity and of the hypomagnetic field, which also changes the reactions of organisms compared to space. The only available place that combines all these three factors together is the ISS. Zeitlin et al., 2019 have just shown that LET spectra measured with the Radiation Assessment Detector (RAD) instrument (Hassler et al., 2012) on the ISS, during a flight to Mars and on the Mars surface are very similar.

2.3 Radiation exposure on the ISS

The radiation environment on LEO consists mainly of trapped radiation and GCR with sporadic SEP and minor contribution of albedo particles. Trapped radiation includes protons with energies up to ≈450 MeV and electrons with energies up to ≈10 MeV. On LEO, GCR differential spectra have a maximum flux value at approximately ≈1 GeV·nucleon^{-1} (Figure 1.4). The radiation spectra vary along the orbit, depending on the altitude and geographic position. The time variation of the radiation environment on the LEO is due to the on the solar activity and geomagnetic conditions. The concerns for astronauts health are associated with trapped proton radiation, SEP and GCR, as they can propagate inside the station and produce secondary radiation.

The average shielding on the ISS is estimated as ≈10-30 g·cm^{-2} (Tessa et al., 2009; Jadrníčková et al., 2009; Badavi, Nealy, and Wilson, 2011).

The radiation monitoring on the ISS is ongoing since the beginning of the mission with different detection systems by different groups. The radiation environment inside the ISS is non-uniform (Jadrníčková et al., 2009), so the radiation dose rate depends on the place. One of the reasons for the difference is the anisotropy in radiation particle fluxes especially in proton fluxes in the region of SAA ().

Another reason for the differences is to non-uniform shielding mass distribution due to the complexity of the ISS geometry. Information about the dose distribution in the spacecraft is essential for mitigating risks for astronauts associated with space radiation. Radiation dose in areas where astronauts provide significant time should be reduced in the first place. Trapped protons and most of SEP have energies lower than 1000 MeV, so they can be stopped with reasonable shielding mass. On the ISS, this concept was tested and implemented during the protective curtain experiment (Sato et al., 2011; Ploc et al., 2013; Kartashov and Shurshakov, 2018; Szántó et al., 2015; Kodaira et al., 2014; Kartashov et al., 2019). The protective curtain was assembled from wet towels and placed on the module wall near the astronauts' workplace. It reduces the radiation dose by 30% and now is used permanently. The concept of using onboard equipment to create a storm shelter in the case of SEP during interplanetary flight is actively discussed and tested now (Striepe, Simonsen, and Nealy, 1992; Simon et al., 2014; Cerro et al., 2015; Hanson, Clowdsley, and Thibeault, 2019).

A good example of the influence of mass distribution on the ISS on dose rates is dose measurements during 2008. Radiation dose rates associated with trapped proton radiation were reduced during the periods when Shuttle docked the ISS. The amount of radiation detectors on the ISS is limited so the radiation dose can be measured in a limited amount of points. Also, not all of the detectors provide detailed information on radiation dose equivalent in real-time. The total dose distribution can be obtained by applying numeric modeling. The accuracy of the dose assessment depends on the implemented method and the model of the ISS. The precise model is not publicly available if it exists. The detalisation of the engineering models down to a single screw is usually too large to use them in calculations. In most calculations are done with either simplified model of entire ISS, or with a more detailed model of a particular part, which is in focus of the research. The latter approach can thus overestimate doses due to trapped radiation as it has been shown during Shuttle missions,

Information provided with radiation detectors does not give the entire picture of the radiation environment on the ISS. The reason is that detectors do not measure energy and angular spectra for each type of particle, which accurately characterizes the radiation environment. Instead, detectors provide values measured according to their instrument response functions. However, the same value can correspond to different radiation environments, and the effect of these environments on the hardware and astronauts can be different. Usage on radiation detectors requires prior knowledge about the radiation environment where they would be used and damage effect of this environment and its correlation with values measured with the detector. This knowledge can be obtained either with modeling or in an experiment. Series of MATROSHKA experiments onboard the ISS is an example.

The MATROSHKA experiments aim to measure radiation dose distribution in biological tissues and astronauts' bodies. For these purposes are used phantoms: models of astronauts made of tissue-equivalent materials. Whole-body phantom was used on Zond-7 spacecraft, Fred on Shuttle missions, and spherical water-field phantom on Mir station. There were two types of phantoms in the MATROSHKA experiment: human torso phantom by DLR (Reitz et al., 2009; Berger et al., 2013) and spherical ICRU spherical phantom by IMBP (Shurshakov et al., 2014; Kodaira et al., 2014). The radiation environment was measured at different points at the phantom surface and in different depths inside it. Knowledge about the radiation dose distribution inside the phantom gives more information about the radiation damage. Also, this experiment provides a useful reference data to validate approaches, used for dose calculations, and radiation environment models.

In the MATROSHKA-R experiment, the radiation dose distribution was measured at the surface and inside spherical and anthropomorphic phantoms made of tissue-equivalent materials. Radiation doses were measured with active and passive detectors at different depths on and under the phantom's surface. Experimental data on the dose distribution at the surface of the spherical phantom was obtained for several ISS modules for 12 time periods. One of the goals of this work is to model experiment conditions for the first and the second session, started on January 29, 2004, and on August 11, 2004, and elongated for 92 and 425 days, respectively. The absorbed dose was measured with thermo-luminescent dosimeters (TLDs). The spherical phantom was located in the Service module cure cabin in the Russian segment of the ISS.

The average module mass of the ISS is about 20 tons, and the average size is 10-by-20 meters (Kartashov and Shurshakov, 2018). The inner geometry is exceptionally complicated. It contains different equipment, made of a variety of materials. Monte-Carlo radiation dose calculations with high accuracy for exact spacecraft geometries require unreasonably long simulation times. The geometry and composition complexity requires simplifying assumptions and the neglect of non-important details.

Sihver et al., 2009 calculated the radiation dose distribution for the MATROSHKA-R experiment with the PHITS Monte-Carlo code. The ISS model was simplified to an aluminum cylinder with 12.5 g·cm^{-2} walls. It was irradiated with an isotropic particle source distributed over a sphere surface. The absorbed radiation dose was calculated for the experiment session from August 11, 2004, to October 10, 2005. The simulation results exceeded the experimental data by a factor of 1.5-2. The authors attributed the discrepancy to the differences between the real and approximated simulation geometries.

An alternative approach to geometry simplification is the ray-tracing method. In a ray-tracing approach, the real geometry is processed into a shielding-distribution function that is a good trade-off between precision and simulation speed. This approach is currently widely used (Kartashov and Shurshakov, 2018; Sihver et al., 2009; Wilson et al., 2014). The shielding-distribution function is calculated for each point of interest. Next, each value of the shielding-distribution function is multiplied by a corresponding dose rate value that is usually calculated in a quasi-infinite layer geometry. The dependence of the radiation dose on the shield thickness is called the depth-dose curve. Kartashov and Shurshakov, 2018 gives a detailed description of the application of depth-dose curves in the context of ray-tracing methods and its application for dose calculation on the ISS. However, the depth-dose curves used in their work do not include neutron contributions and are interpolated between reference curves to cover the entire region of orbits and time.

Matthiä, Berger, and Reitz, 2013 provides an alternative method for the use of shielding-distribution functions. The radiation dose was calculated with GEANT4 for a spherical geometry under LEO radiation conditions. A water sphere with a radius of 20 cm was shielded with an aluminum spherical shell with a 110 cm outer radius. The shell thickness varied in the range from 1 to 100 g·cm^{-2}, according to a shielding-distribution function. The calculated radiation doses exceeded measurements by 20% on average.

In this work, we use a shielding-and-composition distribution function with depth-dose curves. The depth-dose curves are calculated for the actual ISS orbit parameters using SPENVIS system, which derived the radiation spectra using the AP8, AE8, and CREME92 models. We separate contributions of primary and secondary particle radiation to the dose-depth dependences and we distinguish contributions of trapped radiation and GCR to the net dose.

Chapter 3

Methodology

There are three simulation setups used in the current work. First is a spherical layer shielding with a spherical water phantom inside it. The shielding is exposed to isotropic irradiation. The setup is used to calculate radiation doses due to SEP and GCR during interplanetary flight. The second setup is a quasi-infinite planar shielding with a 1 mm thick water detector slab behind it, irradiated with a unidirectional point particle source. This setup is used for depth-dose curve calculations. The third is a simple model of the MATROSHKA-R experiment conditions: the ISS module is described by an aluminum cylinder filled with water foam with a spherical water phantom placed close to the module wall. The setup is used to calculate shielding functions.

3.1 Spherical geometry setup

The spherical setup on figure 3.1 is used to calculate the radiation dose during interplanetary flights. As far as the exact geometry of spacecraft is not known, we decided to use a spherical shielding. We consider only aluminum shielding, as it comprises most of the spacecraft mass. We made calculation for unshielded phantom, and for the shielding of 1, 5, 10, 20, 30, 40, 50, and 60 g·cm^{-2}. The inner radius of the shielding sphere was equal to 50 cm in calculations for section 4.1 and 50 and 100 cm in calculations for section 4.2. We use a 35 cm diameter water sphere with a 10 cm diameter cavity, which is recommended as an astronaut phantom by the Russian state standard (RSA, 2004). The phantom is located in the center of the spherical shielding. The radiation dose is detected in spherical layers with a thickness of 1 mm, except innermost and outermost, which are 0.5 mm thick. The dose in the outer surface layer is assumed to represent the skin dose. The dose in

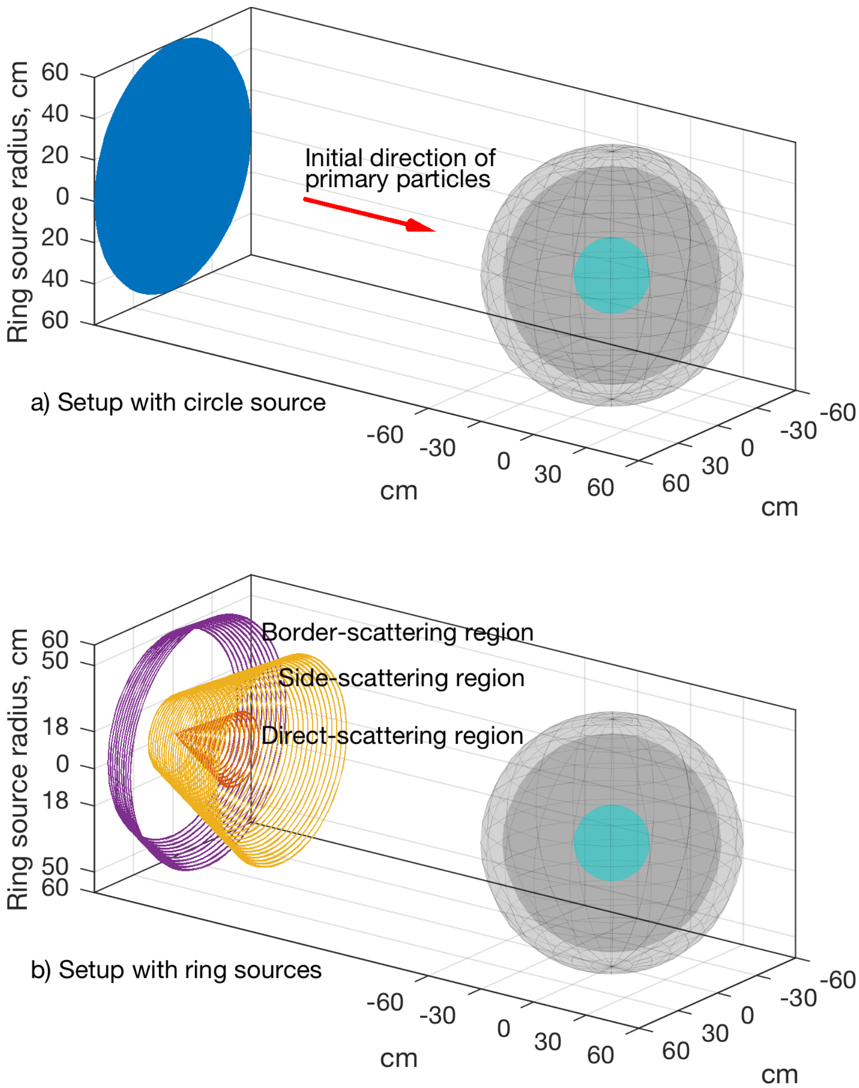

Figure 3.1: Schematic representation of simulation setups used for radiation dose calculations. Spherical water phantom (shown in cyan) is shielded with a spherical aluminum shielding (shown in grey) (a) Setup with a circular particle source (shown in blue). (b) Setup with ring sources; color shows three groups of sources (shown in red, yellow, and violet). For clarity, sources are shifted along the initial propagation direction of primary particles. The red arrow shows the initial direction of primary particle propagation. The figure is published in Dobynde and Shprits, 2019.

the spherical layer, which is 5 cm under the phantom surface, is considered as the BFO and the CS dose. The usage of radiation dose at 5 cm depth is convenient for the BFO. At the same time, we have not found in the literature the depth in spherical phantom, which corresponds to the CS. However, it was suggested by Prof. Shafirkin from the Institute of Biomedical Problems of the Russian Academy of Science also to use radiation dose at 5 cm depth in the spherical phantom. This uncertainty would be addressed in the future, calculating the effective shielding of CS in anthropomorphic phantom and the spherical phantom, in a similar way to Matthiä, Berger, and Reitz, 2013. The result of Matthiä, Berger, and Reitz, 2013 calculations can not be directly used in the current research because they were obtained for 20 cm spherical phantom.

We assume that GCR and SEP create an isotropic particle flux in the near-Earth interplanetary space. Spherical particle source with homogenous surface and angular distribution of generated particles should be used in the case of realistic and complex spacecraft geometry. However, it can be replaced by a planar unidirectional particle source in case of spherical shielding because of the symmetry of model geometry. Both spherical isotropic and planar unidirectional particle sources create the same angular distribution of incident particles on the surface of spherical shielding.

Figure 3.2 demonstrates the angular distribution of incident particles on the surface of the shielding for different particle sources. It can be seen that angular distributions created by isotropic spherical sources, with the diameter larger than five radii of the shielding, are identical to each other and planar unidirectional source and to point source with cosine angular distribution. For the same amount of launched particles, oscillations in normalized angular distribution are higher for the spherical sources with larger radii. That is due to the smaller number of particles that hit into the shielding. For the same amount of launched particles, angular distributions of planar unidirectional and point cosine sources do not have these fluctuations, because all launched particles hit into the shielding. Point isotropic source and spherical isotropic source with a radius equal to the shielding radius create a different angular distribution of primary particles on the shielding surface, with more primary particles directed to shielding edges.

The planar unidirectional particle source has an extra advantage comparing to other sources, besides the absence of fluctuation in angular distribution. One initial direction of primary particles makes it easier to distinguish between induced particles having a velocity component along and opposite to the initial direction of primary

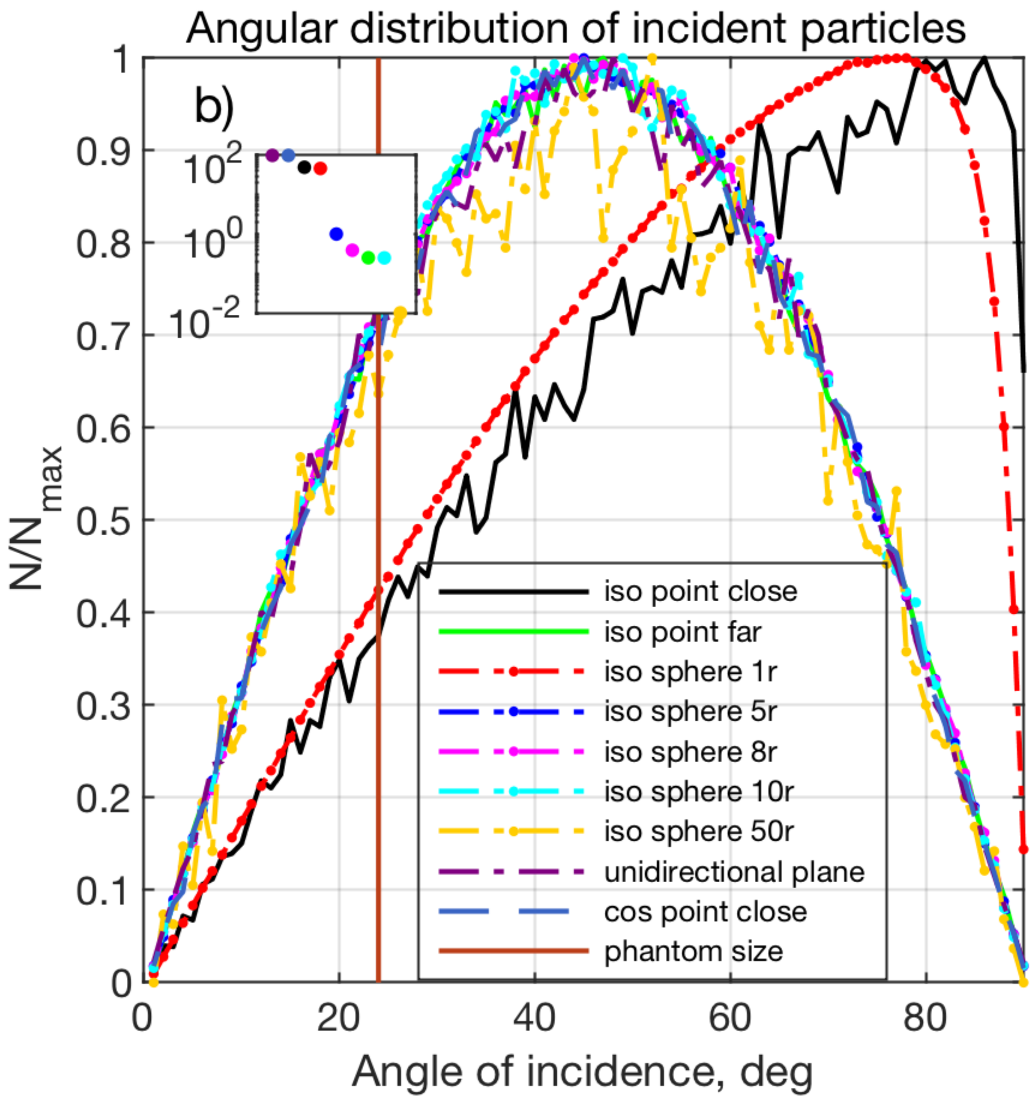

Figure 3.2: Angular distribution of incident particles created on the surface of spherical shielding by different sources.

particles. These two advantages motivated to use a planar unidirectional particle source in the spherical shielding setup.

A spherical source with the radius R creates isotropic irradiation on the shielding sphere with the radius r in case if $R >> r$. A dS surface on the R-sphere creates

$$4\pi \frac{\pi r^2}{4\pi R^2} f dS = \frac{\pi r^2}{R^2} f dS \tag{3.1}$$

almost parallel particle flux through the r-sphere. The net flux through the r-sphere is

$$\int \frac{\pi r^2}{R^2} f dS = 4\pi R^2 \frac{\pi r^2}{R^2} f = 4\pi^2 r^2 f \tag{3.2}$$

The final formula for the radiation dose $D(E)$ adsorbed during period δT due to particle flux f is

$$D(E) = 4\pi^2 r^2 f \delta T \delta D(E) \tag{3.3}$$

where δD is the average dose per one particle that hits into the shielding.

Particles for different parts of the circular source make different contributions to the net dose. Modeling with a circular source allows calculating the mean dose, averaged over particles coming from different regions of the source, and scattered at different angles. The contribution of side-scattered particles to the radiation dose can be calculated using irradiation with ring sources. The areal density of launched particles should be constant over the circular source. If the circular source is split into ring sources, the normalization coefficients should be used to scale doses due to the different ring sources. The coefficients are calculated as follow:

$$\frac{S_{\mathrm{i}}}{S_{\mathrm{net}}}, \sum \frac{S_{\mathrm{i}}}{S_{\mathrm{net}}} = 1 \tag{3.4}$$

was applied to calculate the net radiation dose. Formula 3.3 for dose calculation in the case of a ring source is modified to

$$D(E) = 4\pi^2 r^2 \delta T \sum \frac{S_{\mathrm{i}} \delta D_{\mathrm{i}}(E)}{S_{\mathrm{net}}} \tag{3.5}$$

The results of calculations with ring sources setup is presented and discussed in section 4.2.

3.2 Slab geometry setup

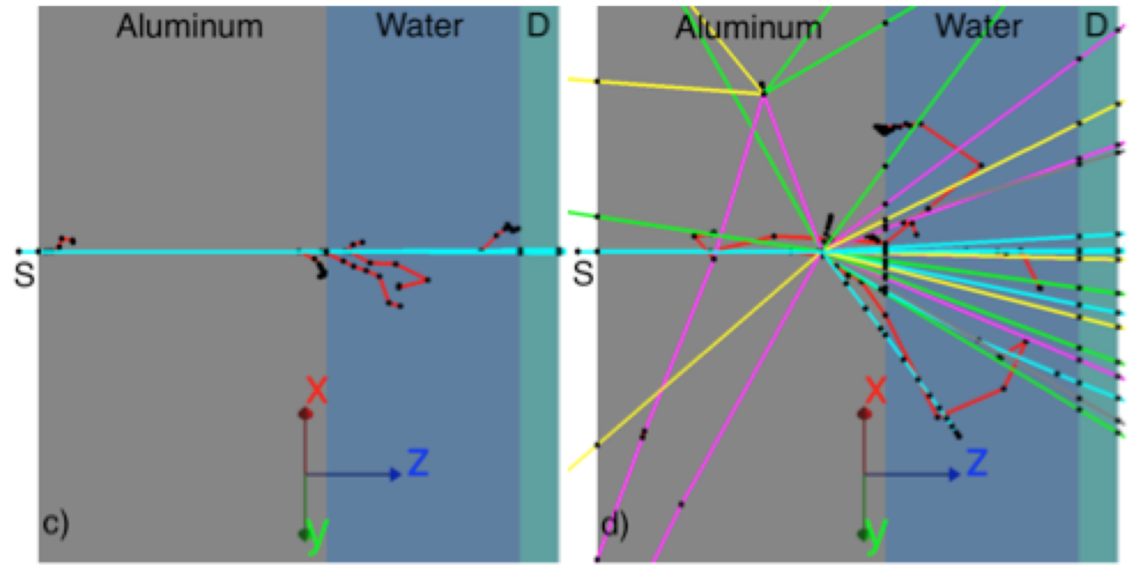

Figure 3.3: Slab geometry setup used for depth-dose curve calculation. The figure is published in Dobynde et al., 2019.

The quasi-infinite slab setup shown in Figure 3.3 is used to calculate depth-dose curves, which are used in section 4.4 and 4.5. The lateral size of the slabs is 10 by 10 meters. Such a large size of slabs guarantees that all particles induced in the shielding hit into the detector slab. The initial direction of the momentum of primary particles is perpendicular to the shielding surface. There are two types of particle source, which can be used for the depth-dose calculations. The first approach is to model planar unidirectional irradiation and to record the radiation dose in a small volume in the detector layer. This approach is used, for example, by Slaba et al., 2017, and is implemented in OLTARIS and SPENVIS systems. The second approach is to use point unidirectional particle source and to detect dose in the entire detector layer. The main advantage of the second option is that it allows obtaining the radial distribution of the dose regarding the initial direction of the momentum of primary particles. The radiation dose in the entire detector is used in section 4.4 and is the same as in the first approach. The radial distribution is used in section 4.5 to determine application limitations of the ray-tracing method, and to improve dose calculation in the near-surface layer of the spherical phantom.

The radiation dose for an incoming flux $f(E)$ is simply calculated

$$D(E) = f(E)\delta T \delta D(E) \tag{3.6}$$

where δD is the average dose per one particle that hits into the shielding, and δT is the irradiation period .

3.3 The ray-tracing method

Monte-Carlo codes are powerful tools that provide detailed information on energy deposition and particle spectra. Unfortunately, they require a lot of machine time to accumulate necessary particle statistics. There are cases when such detailed information about the radiation field is exceptional and can be changed to shorter simulation times. One of the approaches to fast radiation dose calculation is the ray-tracing method.

The ray-tracing method considers primary particle propagation to the point of interest along with many rays passing through it. The main assumption in this simulation methodology is that both primary and secondary particles deposit energy close to the ray and do not deviate significantly from the ray. This assumption is correct for trapped particles (Figure 1c) that have kinetic energy lower than 1 GeV. However, for high-energy GCR particles (Figure 1d), the deposited energy distribution in the detector plane cannot be neglected. However, the ray-tracing method still works, if the shielding composition and thickness along nearby parallel rays are not changing significantly. That is because, in realistic conditions, there is a large and quasi-parallel particle flux instead of a single ray. Primary particles that propagate in the direction parallel to the ray create similar energy distributions in the lateral plane around the point of interest, contributing to the net deposited energy at the point of interest. The net deposited energy at the point of interest is equal to the net energy deposited with a point source in the lateral plane if shielding composition and thickness along nearby parallel rays are not changing significantly. As soon as there are variations, the simulation results will deviate from the actual values.

On the ISS orbit, most of the radiation dose is deposited with trapped protons with an energy lower than 1 GeV and trapped electrons with an energy lower than 10 MeV. Therefore the ray-tracing method was chosen for dose calculation in the MATROSHKA-R experiment in section 4.4. It the experiment, absorbed dose distribution was measured on the surface of a spherical phantom placed close to the

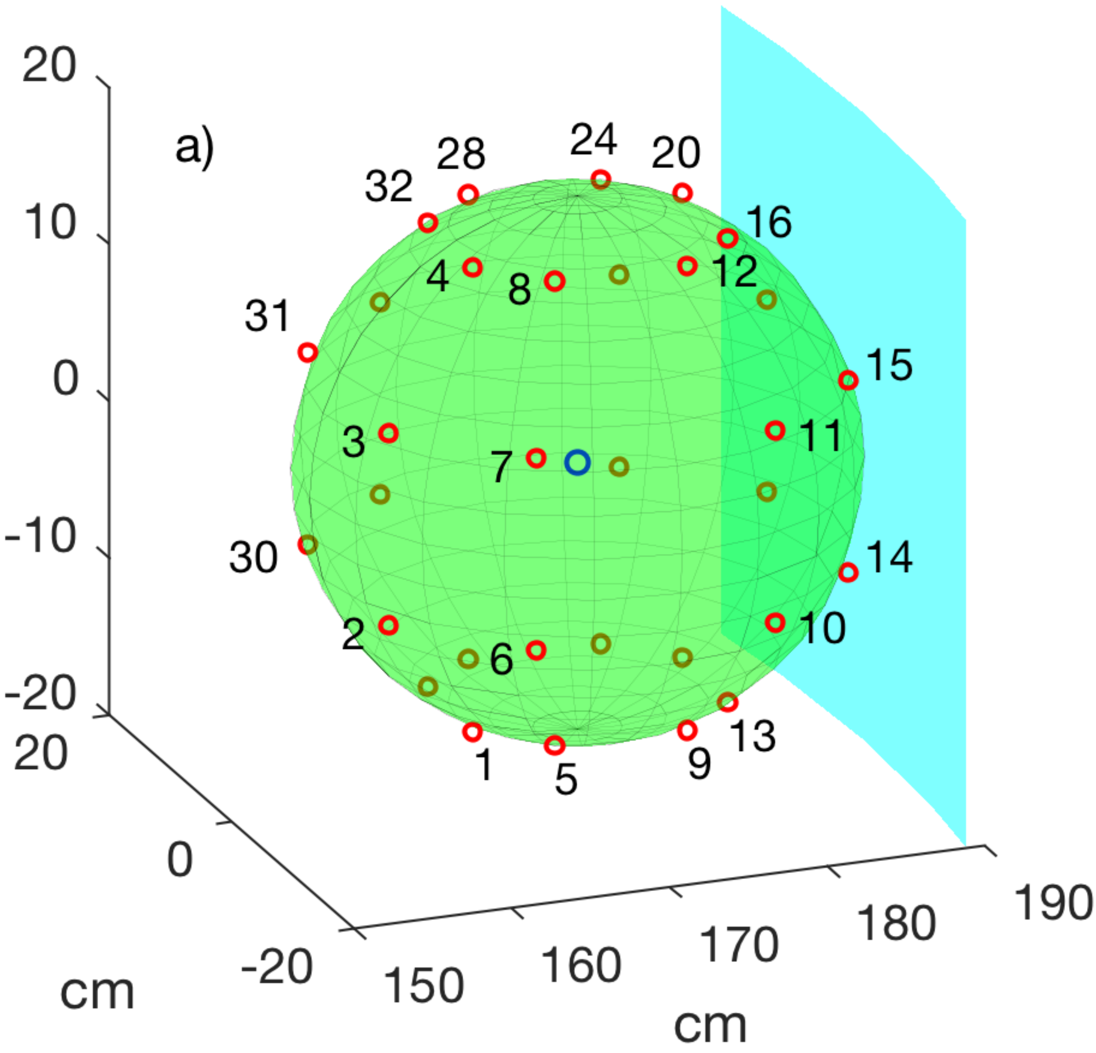

Figure 3.4: Geometry setup used for modelling the MATROSHKA-R experiment. Spherical phantom (shown in green) is placed closed to module wall (shown in blue). Numbered red dots show detectors positions.The figure is published in Dobynde et al., 2019.

ISS outer wall (Figure 3.4). The ray-tracing itself is used to define the shielding structure around the point of interest. The radiation dose at the point of interest is usually calculated, converging shielding function with depth-dose curves. The depth-dose curves are calculated in slab geometry, which repeats shielding structure along the ray. The slab structure is often simplified even more by recalculating different materials into an equivalent one that is usually water or aluminum. However, cross-sections for all particle species and all processes cannot be scaled by the same factor. That was a motivation to calculate the depth-dose curves behind double-

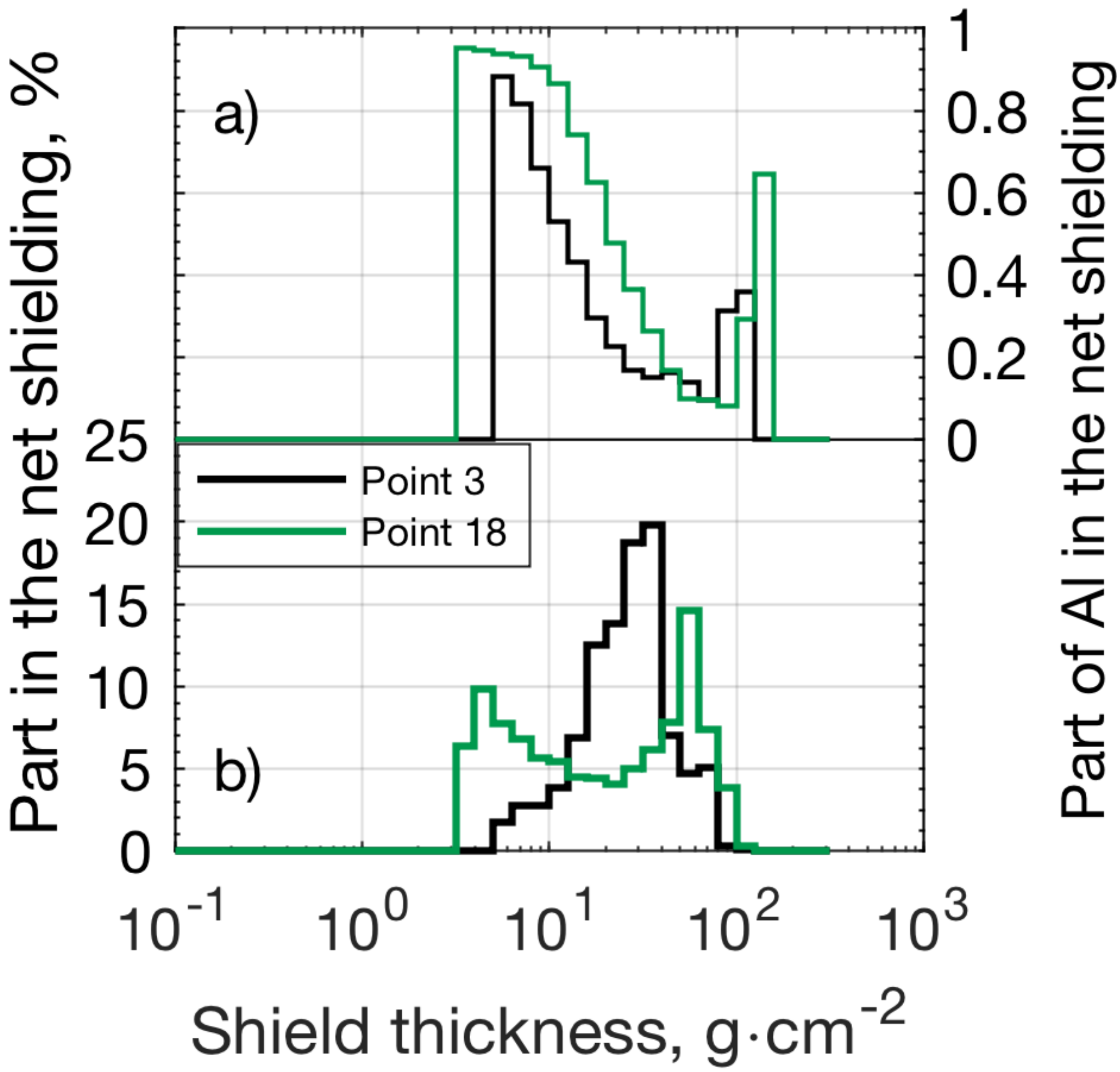

Figure 3.5: Net-shielding function and part of aluminum in the shielding for point 18 that is nearest to the shell (black curve) and point 3 that is most distant from the shell (green curve). The figure is published in Dobynde et al., 2019.

layer aluminum-water shielding with energy deposition in a 1 mm thick water layer. Aluminum makes most of the mass of the ISS, and the spherical phantom is made from tissue-equivalent material, similar to water. Figure 3.5 show as an example shielding-and-composition functions calculated from most distant from the wall and most close to the wall detector positions on the spherical phantom.

3.4 Considering issues of the ray-tracing

Although the results of the calculations in section 4.4 are in good agreement with the experimental results, usage of the ray-tracing method for dose calculation in interplanetary space requires addressing several issues. First, we modified ray-tracing to include lateral energy distribution in dose calculation. Instead of one ray per direction, we launched 100 rays parallel to each other and passing at different distances from the point of interest. Then doses created by rays at the point of interest were summed with corresponding weighting factors. This method was applied to calculate dose distribution inside the spherical geometry setup, used in the first part.

3.5 Programming

3.5.1 GEANT4 simulations

Radiation doses in this research were calculated with the GEANT4 (GEometry ANd Transport) Monte-Carlo code Agostinelli et al., 2003. It was used to simulate particle propagation through the spacecraft shielding and energy deposition in the phantom. The main advantage of GEANT4 comparing to other Monte-Carlo and transport codes is the flexibility that allows users to control almost every aspect of calculations. In this work, particle-matter interactions were described by the FTFP-BERT-HP physical processes list. This physical model includes the Fritiof model for particles with energies higher than 10 GeV, the Bertini Cascade model for energies lower than 10 GeV, and the High Precision Neutron model for energies lower than 20 MeV. It is optimized for radiation protection and shielding simulations.

The largest part of simulations was performed by computational and storage services associated with the Hoffman2 Shared Cluster provided by UCLA's Institute for Digital Research and Education's Research Technology Group. The least part, including preliminary calculations, was performed on a personal laptop. Monte-Carlo simulations in the current research can be performed using multiple cores. Each core executes calculations threads for one type of primary particle, with initial energy from one energy beam, propagation in one of the geometry models. The output data array is generated for each thread. Afterward, the output of all calculation threads was analyzed using Matlab.

3.5.2 Convergency of the calculations

In calculations with spherical setup standard deviation cannot be used to evaluate calculation errors, because it is of the order or even exceeds the mean value. The reason is due to the differences in particle track length in the phantom: particles that propagate closer to the center of the phantom would deposit much more energy than particles propagating more close to the phantom boundary. That's why we decided to use normalized mean dose deviation as the criteria for result convergence. Namely, we use the value of normalized deviation Δ, which is calculated on iteration N+1 as:

$$\Delta_{\mathrm{N+1}} = \frac{D_{\mathrm{N+1}} - D_{\mathrm{N}}}{D_{\mathrm{N+1}} + D_{\mathrm{N}}} \tag{3.7}$$

where $D_{\mathrm{N+1}}$ is the average dose after N+1 iteration and D_{N} is the average dose after N iteration. We start calculating the normalized deviation on 1001 iteration. As soon as Δ keeps less than 0.001 during 1000 iterations we assume that we get a stable solution. Thus minimum iteration number is 2000 while the maximum is set to keep particle density on the source surface equal to 40 cm^{-2}. For the smallest shielding thickness of 5 g·cm^{-2} the maximal number is 107500 and for 60 g·cm^{-2} shielding this is 208600. For the unshielded sphere, this value is 100000.

The regulations of usage of Hoffman2 Shared Cluster allowed running 24-hours jobs with acceptable job priority, and the maximum number of running jobs was limited. For this reason, in the first run, each job parameters of geometry, particle type, and source parameters were fixed, while particle energy was changed one by one in the whole energy range. Usually, the 24-hour time was insufficient to complete calculations for the whole energy range. The missed data has been identified at the stage of data upload in Matlab, and the next set of calculations has been initialized and launched. Depending on the amount of missing data it was organized either as one energy per job calculation or as a set of energy per job calculation.

3.5.3 Features of C++ code

In this research simulation setup, geometry was described using GDML files. GDML is an XML based language used for geometry description. It allows describing geometry using simple shapes, like spheres, cubes, etc. It also supports surface description with surface elements (triangles). The main advantage that would be used in further research is the possibility to convert CAD files into GDML. CAD files are essential for calculations with a realistic spacecraft geometry. It was also helpful to generate large sets of similar geometry files with Matlab at the step of C++ project generation. All information for each calculation thread such as particle type, energy, direction, etc. was uploaded to program from corresponding files, that were pre-generated by Matlab.

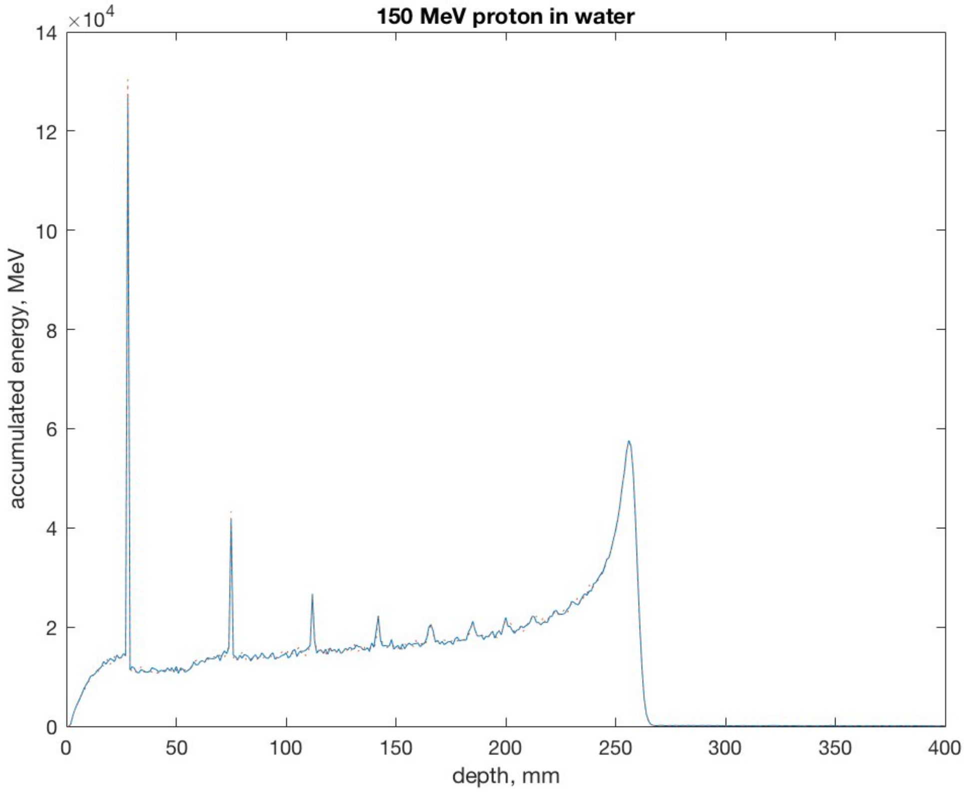

Figure 3.6: Artefact peaks in absorbed energy distribution (the Brag curve) due to insufficient spatial resolution (large step length limit). Calculations are performed for protons with the initial energy of 150 MeV propagating in a water slab.

GEANT4 allows setting the maximum step length limit. A large step limit reduces the calculation time but can result in artifacts like extra peaks in energy deposition shown in Figure 3.6. The step limit value can be set separately for each volume in the geometry. In this work, the limit values for each volume were stored in a separate file and used by the program during calculations. For data storage and analyze GEANT4 allows setting a region of interest in the geometry model as a "DetectorVolume". It can be useful for modeling instrument response functions. However, the "DetectorVolume" limits flexibility for data output and was not used in this research. Instead, different conditions in the "SteppingAction" file were used to track particle propagation though the model and energy deposition inside the phantom.

3.5.4 Output data

The main output data in this research are spatial distributions of absorbed dose and dose equivalent distribution inside the phantom. In a spherical phantom, these are dose dependencies on the radial distance and the z-coordinate. In water slab, these are dose dependencies on the lateral distance from the initial primary particle direction and the z-coordinate (for calculations with back shielding in part 3). Also, particle energy, rigidity, and angular spectra were calculated at the entrance of the phantom and at the exit from shielding into outer space.

All dependencies were classified according to 8 particle species (protons, neutrons, ions, gammas, leptons, mesons, other baryons, and "other particles") and into 4 general groups. The general groups are primary particles, secondary particles propagating in forward (having a velocity component along the initial direction of primary particles) and backward directions (having a velocity component opposite to the initial direction of primary particles) and multi-pass particles that passed through the phantom for a second time or more often. By primary particles, we mean particles that were generated in the source, and by secondary, we mean all particles that enter the phantom and are not primary. All particles generated in the phantom are classified according to their generation tree from the particle that entered the phantom.

Uncompressed output files required vast disk space, so they were stored as compressed archives. The output files were written in folders according to the data type during the calculations. These folders were common for all calculation threads. Folders were compressed to archives when all calculation threads are finished. This approach significantly simplified data transfer, processing, and storage. Grouping files according to data type give an extreme advantage in time at the processing stage because only one archive should be extracted to get data of a certain type. Each output file contained information on particle type, energy bin, direction, etc.

in its title.

3.5.5 Data processing

Output datasets of GEANT4 calculations are vast. They were processed in Matlab. Matlab is excellent for the current research because it is optimized for matrix processing. Matlab was also used for:

- C++ projects and bash scripts generation
- Input datasets for C++ generation
- Particle spectra generation
- Merging output data
- Radiation dose calculation and other data processing
- Figure plot

Each type of output data is stored in a single archive. If there is a need to process a certain type of data, the archive is extracted, and the list of files is created. Each filename contains all information about the calculation parameters, which is extracted using parsing. The data list of the calculation set is created, processing all filenames. At the next stage variable for data is created according to the dimensions of the data list and dimensions of data in the first file. Then, data from all files in the list is uploaded. The variable with data is stored, and the extracted archive is removed. Next, the data on deposited dose and dose equivalent is multiplied by particle flux, exposure time, exposed area, and scaling coefficients according to formulas in previous sections. All operations are made with matrixes to reduce the calculation time.

Matlab functions have been widely used for routine procedures, namely: creation for file list, data list, prolongation list; creating figures with unified style for the regular plot, color plot, and multiple plots; a bunch of functions for initialization of GEANT4 projects.

3.6 Dose calculation methodology

In a single simulation run, one space radiation particle (primary particle) through the model geometry was simulated. Also, all secondary particles that were generated were considered. For primary particles we considered kinetic energy ranges from 0.0075 MeV to 450 MeV for trapped protons, 0.01 MeV to 7.25 MeV for trapped electrons and from 7.9 MeV$\cdot$nucleon^{-1} to 125000 MeV$\cdot$nucleon^{-1} for 28 GCR particles from hydrogen to nickel. The energy range was divided into 30 bins for trapped radiation particles and onto 21 bins in a logarithmic scale for the GCR particles. Energy distribution in each bin was flat.

The dose equivalent was calculated for each particle-matter interaction event using deposited energy and radiation quality factors dependent on the LET value and recommended by the ICRP, 1991 (see Table 1.1).

dose values for energy bins were multiplied by particles' integral flux in this energy bin to get the radiation dose for a certain particle spectrum. Monte-Carlo simulations are time-consuming, especially for high-energy GCR particles. This technique allows for avoiding expensive simulations for each particle spectrum. From this perspective, the results of Monte-Carlo calculations can be treated as "instrument response functions".

Chapter 4

Results and discussion

4.1 Optimal time and shielding for a flight to Mars

This section presents results of radiation exposure due to GCR and SEP in an interplanetary flight calculated with spherical geometry setup irradiated with circular source.

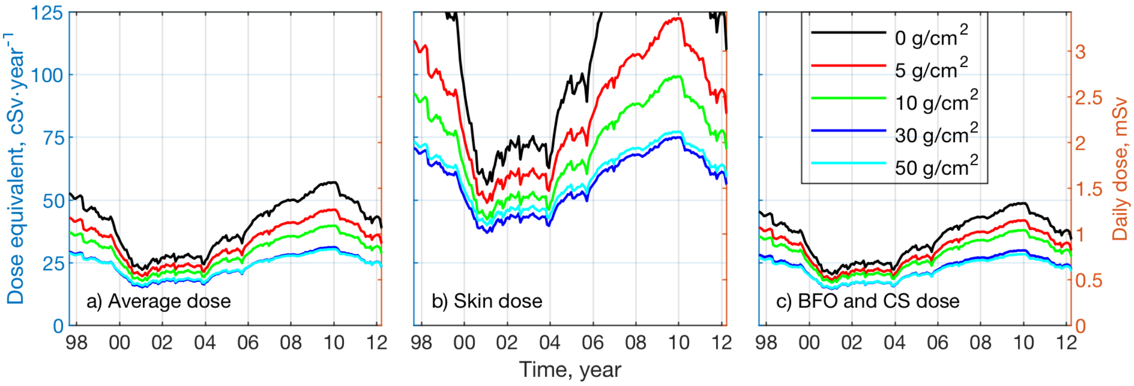

Figure 4.1: Time dependence of GCR dose equivalent for different shielding thicknesses (indicated by the different colors). Panel (a) shows the dependence of the average dose, (b) the dependence of the skin dose (0.5 mm layer at the surface of the phantom), (c) the dependence of the BFO and CS dose (1 mm layer at 5 cm under the phantom surface).

Figure 4.1 shows the time dependences of GCR doses from 1998 to 2012 behind aluminum shielding of different thicknesses. The average dose is detected in the entire phantom. The skin dose is detected in the 0.5 mm surface spherical layer of the phantom. The dose in BFO and CS is detected in the 1 mm spherical layer located 5 cm under the phantom surface. The absorbed dose during the 2001 solar maximum is higher behind thinner shielding, but during the 2010 solar minimum, it is higher behind thicker shielding. An increase of the shielding from 0 g·cm^{-2} up to 30 g·cm^{-2} results in the decrease of the dose equivalent. The dose equivalent calculated for shielding of 30 g·cm^{-2} and 50 g·cm^{-2} is very similar. It should be noted that GCR variations due to solar activity are different at different energies. Figure

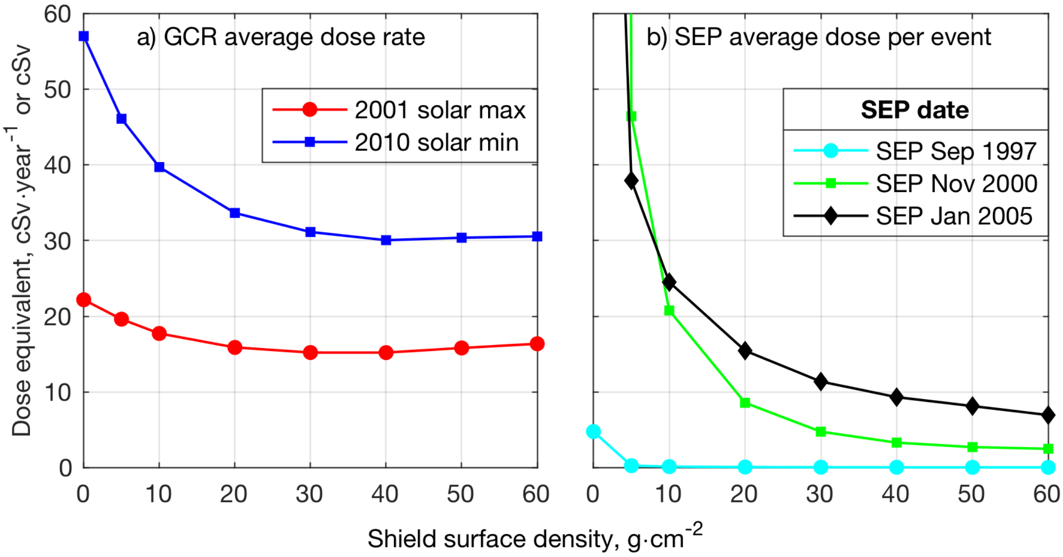

Figure 4.2: (a) Dependence of the GCR dose equivalent on the shielding thickness. (b) Dependence of the SEP dose equivalent on the shielding thickness for three large solar particle events.

4.2b presents the dependence of the dose equivalent on the shielding thickness for three "typical" SEP events. Note that the y-axis shows the total dose per event, while Figure 3a shows the dose rate per year from GCR radiation exposure. Dose calculations are presented for three SEP events: (1) September 1997, (2) November 2000, and (3) January 2005. The common feature is that the dose equivalent decreases monotonically with increased thickness of shielding. It can be seen that for shielding thicknesses over 20 g·cm^{-2}, the SEP-produced radiation dose is lower than the annual GCR dose for all considered SEP events. The average dose equivalent due to the "weak" event in September 1997 (cyan curve) is 5 cSv for unshielded phantom and almost zero if there is shielding. The "large" SEP events in November 2000 (green triangles) and January 2005 (black triangles) cannot be entirely suppressed even with 60 g·cm^{-2} aluminum shielding. These two dependencies demonstrate the influence of SEP particle spectra on the dose equivalent dependence on the shielding thickness. Proton flux at energies less than 200 MeV during November 2000 event is significantly higher than during January 2005 event (Figure 1.2) and results in higher dose equivalent values behind shielding thinner than 10 g·cm^{-2}. However, the situation changes to opposite behind shielding over 10 g·cm^{-2} due to larger flux of protons with energy over 200 MeV in January 2005 event, comparing to November 2000 event.

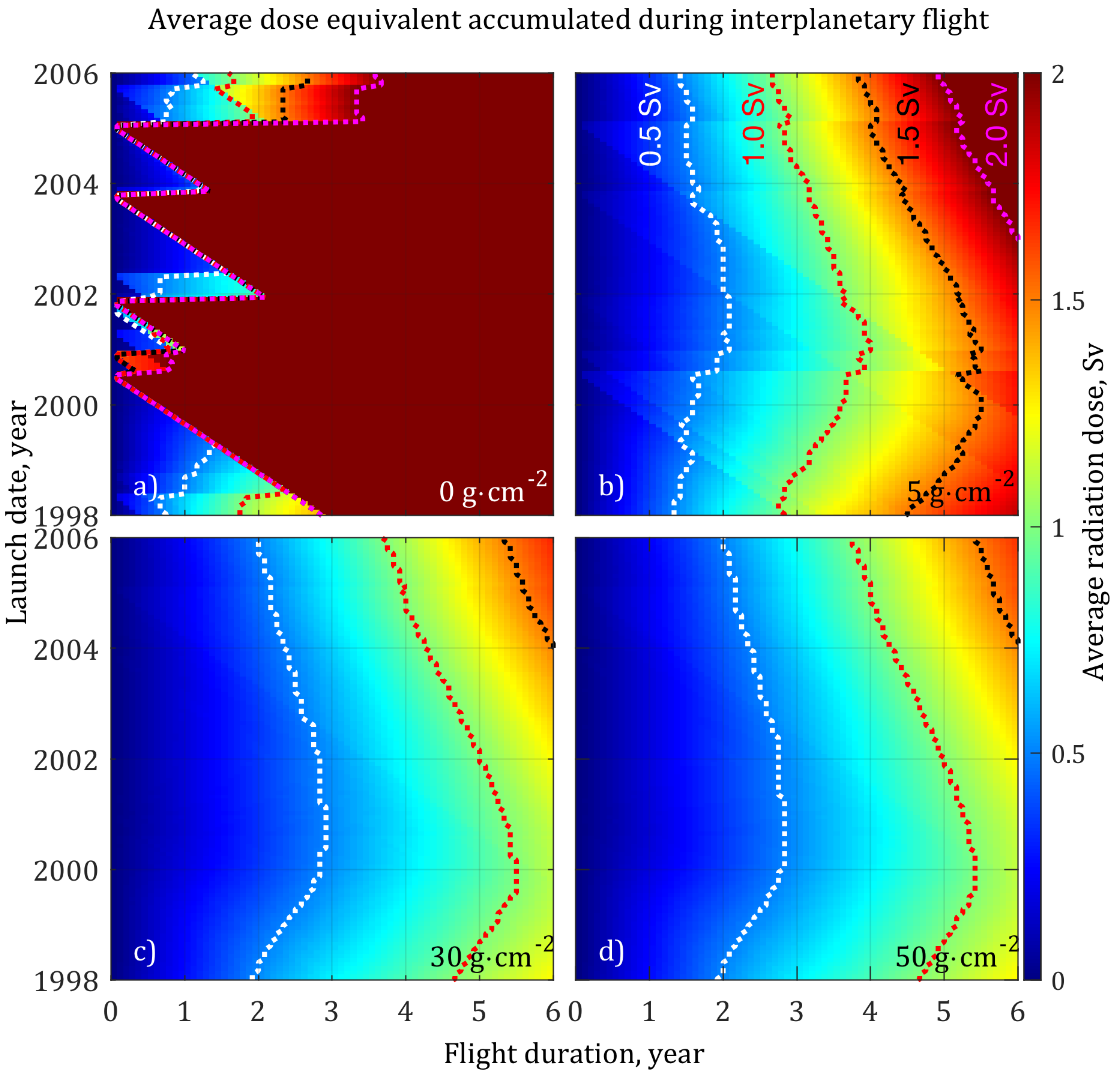

Figure 4.3: Dependence of the net average dose equivalent accumulated during an interplanetary flight on the mission duration (x-axis) and launch date (y-axis). Panel a) shows the dose dependence for an unshielded phantom; panel b) behind shielding of 10 g·cm^{-2}, c) 30 g·cm^{-2} and d) 50 g·cm^{-2}. Dotted curves show levels of 0.5 Sv (white), 1 Sv (red), 1.5 Sv (black) and 2 Sv (magenta), respectively.

Figure 4.3 shows the accumulated net dose equivalent from GCR and SEP particles as a function of the launch date and mission duration. These dependencies include 56 solar particle events during the period from 1998 to 2006. For each solar event, the fluence spectra of hydrogen, helium, carbon, nitrogen, oxygen, neon, magnesium, silicon, sulfur and iron ions are considered.

The SEP deposit a huge dose of radiation in the phantom when it is unshielded (Figure 4.3a). The radiation dose without shielding will exceed 2 Sv after any solar event. For the launch in 2006, after a 4-year flight without solar events, the accumulated dose equivalent exceeds 1 Sv. However, such a low shielding scenario is unrealistic and can only be used to model the extravehicular activity, which makes up a small proportion of an astronaut's time in space. For 5 g$\cdot$cm^{-2} shielding (Figure 4.3b), the SEP contribution can be seen for launch dates before 2001 and 2005, but the net dose reaches the value of 1 Sv that can be considered critical for a 4.5-year mission launched around 2006. For 30 g$\cdot$cm^{-2} shielding (Figure 4.3c) and 50 g$\cdot$cm^{-2} shielding (Figure 4.3d), the maximum radiation dose value of 1.5 Sv is reached in a 6-year mission launched around 2006. The dose of 1 Sv is reached for a 5.5-year mission launched in 2000, behind a shielding of 30 g$\cdot$cm^{-2}. Shielding of 50 g$\cdot$cm^{-2} has approximately the same efficiency as that of 30 g$\cdot$cm^{-2}, but the neutron component in the net dose is large by a factor of $\approx$2, compared to the 30 g$\cdot$cm^{-2} shielding.

4.2 Astronauts radiation dose composition during the flight to Mars

This section presents results of radiation exposure due to GCR in an interplanetary flight calculated with spherical geometry setup irradiated with circular and ring sources.

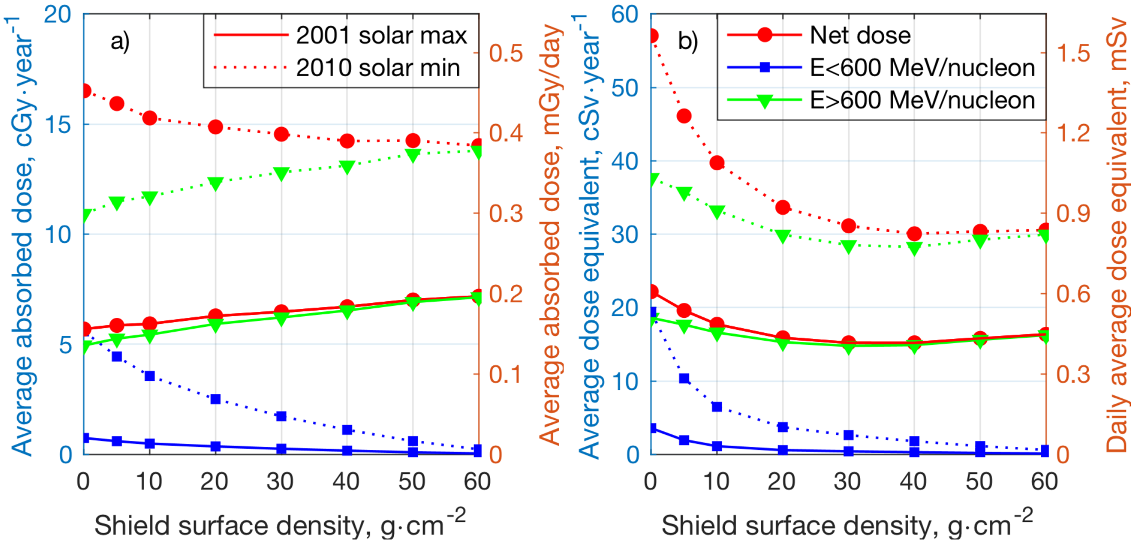

Figure 4.4: (a) GCR absorbed dose and (b) dose equivalent as a function of the thickness of shielding. Dependences during solar maximum are shown with solid lines and during solar minimum with dotted lines. The net dose is shown by the red circle markers, the dose from GCR particles with energy lower than 600 MeV·nucleon^{-1} by the blue square markers, and the dose from GCR particles with energy higher than 600 MeV·nucleon^{-1} by the green triangle markers.

The average absorbed GCR dose during the 2010 solar minimum decreases (Figure 4.1a) but is significantly higher than during the 2001 solar maximum. The net dose equivalent during solar maximum has a weak minimum at 30 g·cm^{-2}(Figure 4b) that can be considered as an optimal shielding thickness. The radiation particle spectra determine the dependencies of the dose on shielding thickness. The dependence of the GCR spectra on the phase of the solar cycle is stronger for low-energy particles than for high-energy particles. To examine the contribution of low- and high-energy GCR particles to the radiation dose, we divided the GCR particles into two groups shown on Figure 4.4: (1) particles with energies lower than 600 MeV·nucleon^{-1} (blue curves), and (2) particles with energies higher than 600 MeV·nucleon^{-1} (green curves).

The net doses (red curves in Figure 4.4) during the solar maximum are determined mostly by high-energy particles (green curves). The absorbed doses increase with shielding thickness because of the production of secondary particles in the shield. The dose equivalent has a local minimum at 30 g·cm^{-2}.

During solar minimum, these dependencies are modified with a low-energy particle contribution (blue curves) that decreases with thickness. As a result, the increase of shielding thickness leads to a decrease in the net absorbed dose and dose equivalent.

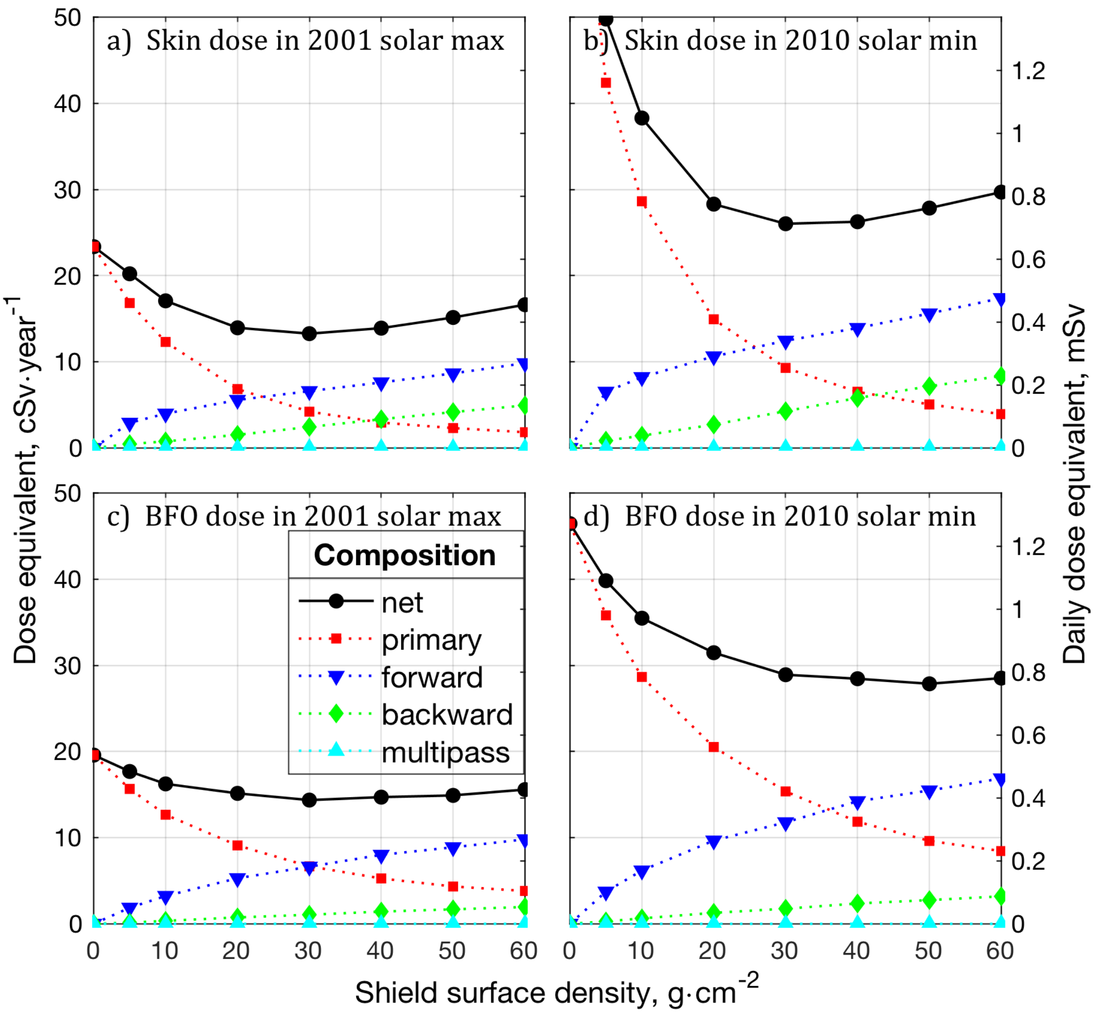

Figure 4.5: Dependence of dose on shielding thickness during 2001 solar maximum (panels a, c) and the 2010 solar minimum (panels b, d). Panels (a) and (b) show the dependence of the skin dose and panels (c) and (d) show the dependence of the BFO dose on shielding thickness.

While the SEP radiation dose is mostly due to primary particles, secondary particles significantly contribute to the GCR radiation dose. All particles are divided into four large groups: (1) primary particles, (2) secondary particles propagating forward (having velocity component along the initial direction of primary particles), (3) secondary particles propagating backward (having velocity component opposite to the initial direction of primary particles), and (4) secondary multipass particles that pass through the phantom two or more times. We refer to primary particles as the particles launched from the source and to secondary particles as the particles that pass into the phantom and are not primary. Figure 5 shows the contribution of primary, forward propagating, backward propagating and multipass particles to the net dose equivalent.

Figure 4.5 clearly shows that the net GCR dose equivalent is lower during solar maximum (black curves). There are also several features that are common to all panels. The first is that the primary particle contribution (red curves) decreases monotonically with an increase of shielding thickness. The second is that the contribution of secondary (blue and green curves) particles monotonically increases with an increase of shielding thickness.

Forward propagating secondary radiation (blue curves) is almost the same in skin and BFO, which means that high-energy secondary particles create it. This component is determined by the spacecraft shielding thickness and cannot be reduced. Backward propagating secondary radiation (green curves) is higher in the skin than in BFO. This difference is due to 5 g·cm^{-2} extra water shielding of BFO that efficiently absorbs backward propagating radiation. It means that backward propagating radiation has relatively low kinetic energy. This is one more demonstration and explanation of why distributing hydrogen-contain materials along the inner walls of a spacecraft is an efficient way to reduce GCR radiation. Dose equivalent from backward propagating radiation can be considered as the maximal achievable attenuation of the GCR dose equivalent, as forward propagating radiation is produced by high-energy particles and cannot be effectively shielded by hydrogen-rich materials.

It is also worth noting that the radiation dose from multi-pass particles (cyan curves) increases with thicker shielding, but is much lower than the other components.

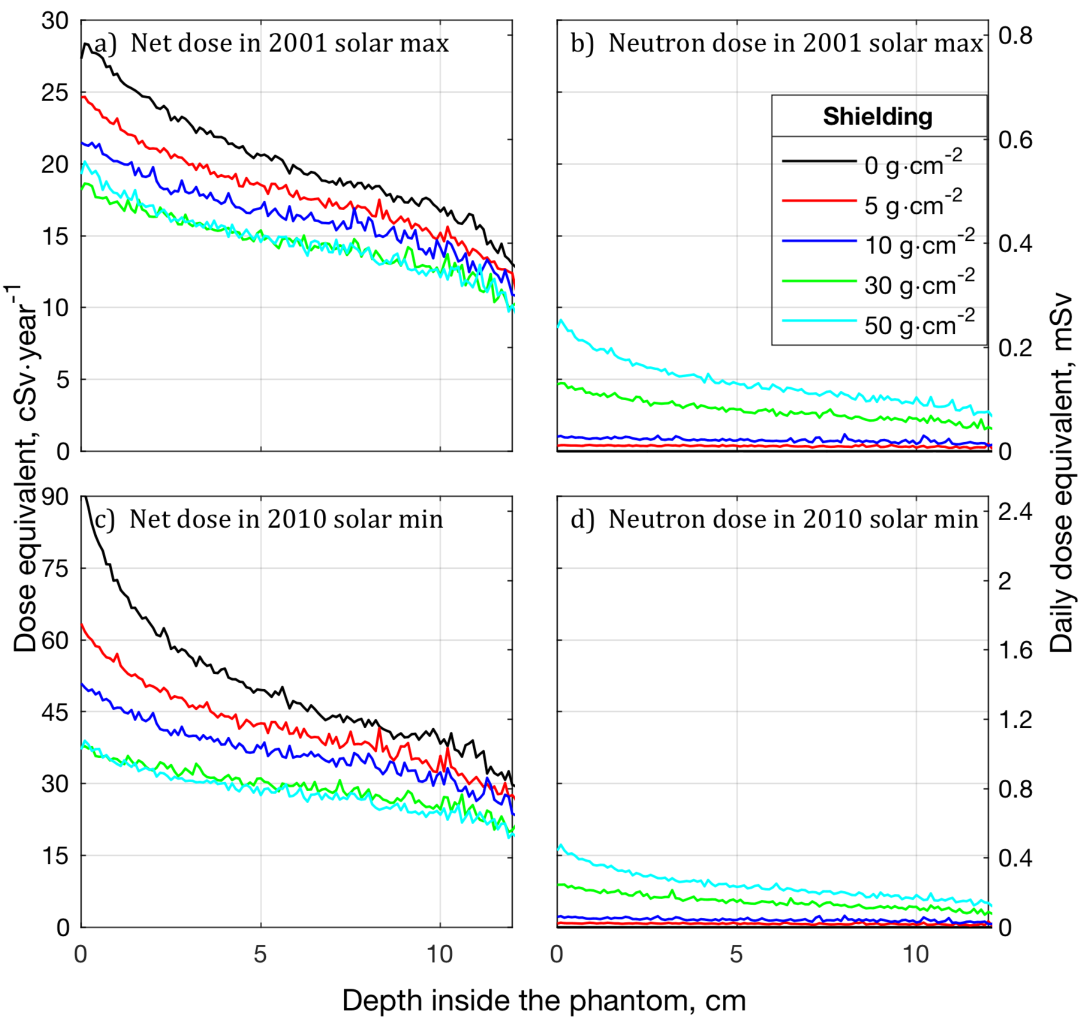

Figure 4.6: Depth distribution of GCR dose equivalent inside a water phantom behind shielding of different thicknesses. Panels (a, b) show the dependence during solar maximum and panels (c, d) during solar minimum. Panels (a, c) illustrate the distribution of the net dose, whereas panels (b, d) show the distribution of the secondary neutron dose.

Figure 4.6 shows the distribution of the radiation dose inside the phantom. As we take the constant step of 1 mm by depth, the volume of the element decreases with the depth, and the number of particles per considered volume is small and reaches counting statistics. This explains oscillations seen at a depth of ≈10 cm and more.

The net dose equivalent (Figure 4.6a,c) decreases with depth inside the phantom behind all chosen thicknesses of shielding. It can be seen that the net dose distribution (Figure 4.6a,c) behind any shielding during solar maximum (Figure 4.6a) is lower than the radiation dose distribution behind the thickest shielding during solar minimum (Figure 4.6c). The dose of secondary neutrons increases by a factor of two during solar minimum (Figure 4.6b,d), when the GCR flux is significantly increased in comparison to solar maximum. The radiation dose from GCR, with energies greater than 600 MeV$\cdot$nucleon^{-1}, also increases by a factor of two during solar minimum (Figure 4), which means that these high-energy GCR particles produce secondary neutrons .

The net dose decreases with an increase of thickness of shielding up to 30 g$\cdot$cm^{-2}, whereas the dose of secondary neutrons (Figure 4.6b,d) increases for all selected thicknesses of shielding. Although there is not much difference in the net dose behind 30 g$\cdot$cm^{-2} and 50 g$\cdot$cm^{-2}, the dose of secondary neutrons is two times higher behind 50 g$\cdot$cm^{-2} shielding. During the solar maximum in 2010, behind 50 g$\cdot$cm^{-2} shielding, secondary neutrons contributed up to 50% of the net dose for skin, up to 30% for BFO (5 cm depth), and up to 20% for deeper (greater than 10 cm depth) phantom regions. Therefore it is of vital importance to measure the neutron dose. Otherwise, the measured net dose would be significantly lower than in reality, and the risk for an astronauts' health might be underestimated.

The results shown in Figure 4.5 can be summarized as general recommendations for spacecraft design:

- A long-duration mission should be scheduled only for the period of solar maximum to reduce the influence of high-energy GCR radiation.

- Spacecraft shielding should be thick enough ($\approx$10-30 g$\cdot$cm^{-2}) for efficient attenuation of SEP radiation.

- Spacecraft shielding should not be thicker than $\approx$10-30 g$\cdot$cm^{-2} to prevent the production of secondary particles.

Composites have often been discussed for use in deep space habitats. Materials such as a carbon composite with significant hydrogen may potentially improve shielding and allow for a longer duration flight.

The latest experimental results show that brain irradiation with much lower equivalent doses can cause permanently reduced organism activity. Also, the skin dose equivalent is higher than the average, so the probability of chronic effects for the skin is higher.

Although the average dose equivalent behind shielding thicker than 30 g·cm^{-2} remains approximately the same, the dose composition changes significantly. Particularly, the dose of secondary neutrons increases with increased shielding thickness. During solar maximum, the dose equivalent from secondary neutrons can contribute up to 50% for the skin, up to 30% for the BFO, and up to 20% for deeper phantom regions. The influence of neutrons on an organism is not clearly understood, which can be a reason for concern. This provides another argument not to increase shielding thickness over 30 g·cm^{-2}.

According to our simulations, the optimal shielding thickness is ≈30 g·cm^{-2}. The dependence of the skin dose equivalent on the shielding thickness has a local minimum at 30 g·cm^{-2} at any phase of solar activity. The dependences of average and BFO dose equivalent on thickness have a local minimum at 30 g·cm^{-2} only during solar maximum. During solar minimum, the average and BFO dose equivalent is constant behind shielding greater than 30 g·cm^{-2} and significantly higher than during solar max.

The shortest Earth-to-Mars flight times will be in 2030 and 2050, corresponding to the period of solar maximum. Current work shows that for the previous solar cycle, the smallest dose equivalent would be accumulated for a flight started in 2000 during solar maximum. The dose equivalent will be 0.5 Sv after a 3-year flight and 1 Sv after a 5.5-year flight if the average astronaut's shielding is around 30 g·cm^{-2}. Some organs can be more sensitive to the radiation, and the critical dose value can be smaller than 1 Sv.

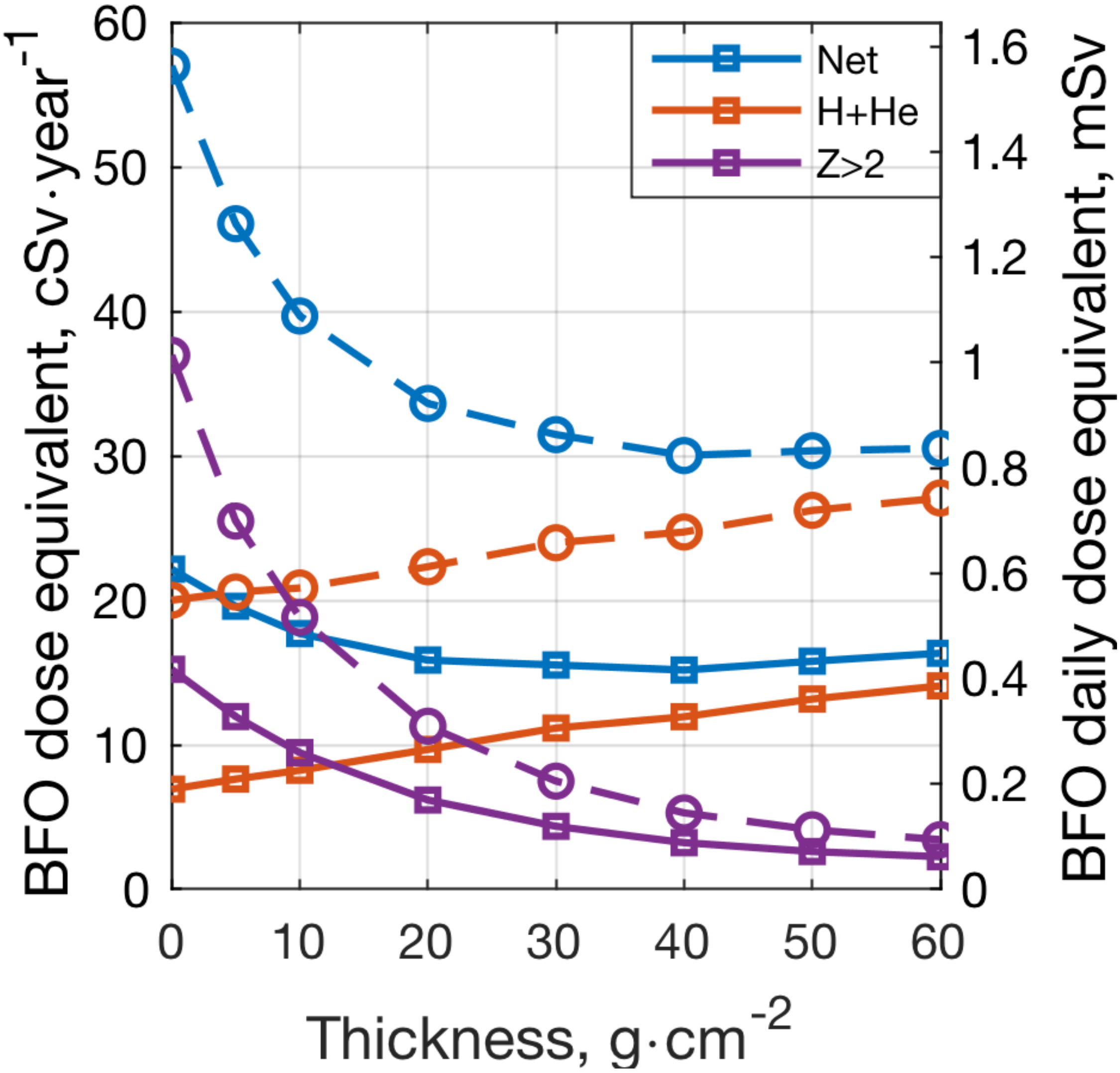

Figure 4.7: Dependence of the BFO dose equivalent due to GCR particles on the thickness of aluminum shielding with an inner radius of 50 cm. Solid curves show dependences for the period of the 2001 solar maximum and dashed curves for the period of the 2010 solar minimum. The net dose is shown in blue, the dose from GCR protons and alpha particles in red, and the dose from GCR heavier particles (from lithium to nickel) in violet. The figure is published in Dobynde and Shprits, 2019.

Figure 4.7 shows the dependence of the radiation dose equivalent on aluminum shielding thickness for the net dose (blue curve), the dose due to the light GCR particles (protons and alpha particles), and the dose due to heavy GCR particles (Z¿2). It can be seen that most of the radiation dose is due to heavy GCR particles if the shielding thickness is lower than ≈10 g·cm^{-2}. Light GCR particles (protons and alpha particles) make up most of the radiation dose behind aluminum shielding with a thickness of over ≈10 g·cm^{-2}. Considering that the most common average shielding for crewed space missions is more than ≈10 g·cm^{-2} (Tessa et al., 2009, Jadrníčková et al., 2009, Badavi, Nealy, and Wilson, 2011) and that Monte Carlo calculations for a full set of GCR particles are time-consuming, we next present calculation results of the dose equivalent due to the GCR proton and alpha particles only. We also focus on the period of solar maximum, as the GCR radiation doses are smallest during this period of the solar cycle.

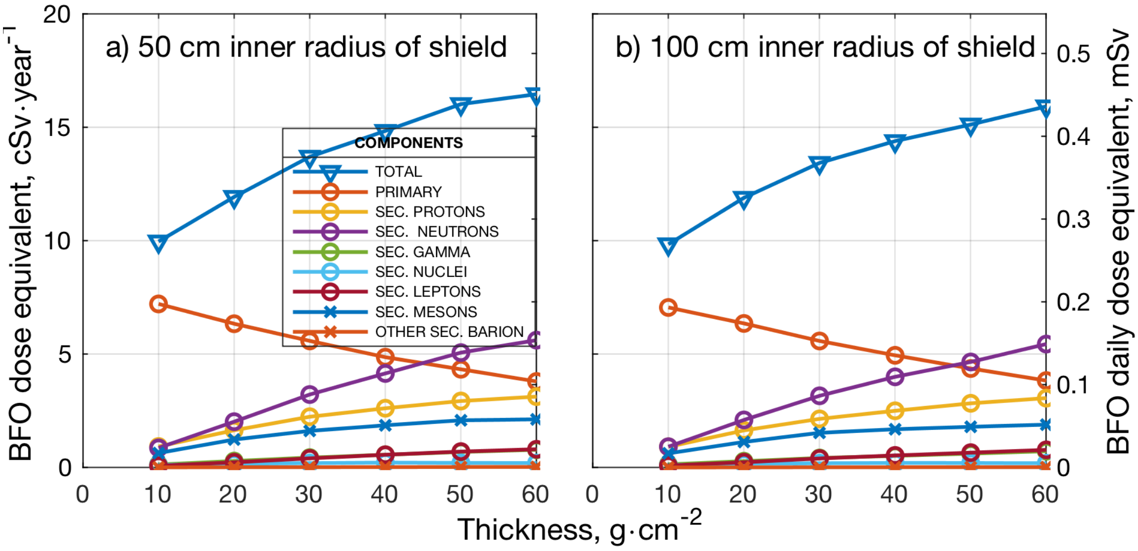

Figure 4.8: Dependence of the BFO dose equivalent due to GCR protons and alpha particles on the thickness of aluminum shielding during the period of the 2001 solar maximum. The inner radius of the shielding sphere is 50 cm (a) and 100 cm (b). Dependences for different particle species are shown in different colors or markers according to the legend. The figure is published in Dobynde and Shprits, 2019.

Figure 4.8 shows the net dose equivalent dependence on the shielding thickness and contribution of secondary particles of different species to the net dose. It can be seen that the primary particle contribution decreases with increasing shielding thickness, while the secondary particle contribution increases. Among the secondary particles, the highest contribution to the net BFO dose equivalent is due to secondary neutrons, protons, and mesons. We made two sets of dose calculations: one for shielding with an inner radius of 50 cm and the second for shielding with a 100 cm inner radius. For the same shielding thickness, the radiation dose from secondary particles is slightly higher in the shielding with a smaller radius.

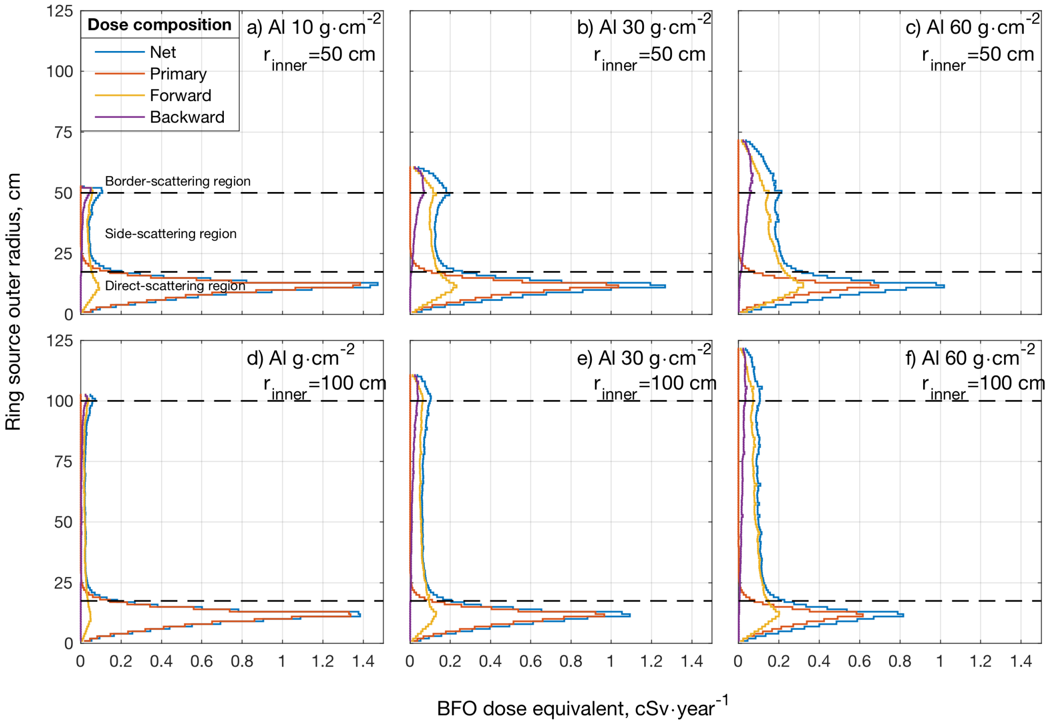

Figure 4.9: Dependence of the BFO dose equivalent due to GCR protons and alpha particles on the ring source radius during the period of the 2001 solar maximum. Dependences for the net dose and its components are shown in different colors according to the legend. Horizontal lines separate direct-, side- and border-scattering regions. The figure is published in Dobynde and Shprits, 2019.

Figure 4.9 shows the contribution to the BFO dose equivalent from different ring sources. For the following discussion and analysis, we divide the ring radiation sources into three groups: a region of direct-scattering from 0 cm to 18 cm, a region of side-scattering from 18 cm to 50 cm or 100 cm (the inner radius of shielding), and a region of border-scattering from the inner radius of shielding to the outer radius of shielding. We also refer to the particles that come from a region of side-scattering and border-scattering as “indirectly scattered” particles.

The radiation dose from primary particles (red curves in Figure 4.9) is mostly due to primary particles that have initial momentum directed to the phantom, which corresponds to the ring sources in the range from 0 cm to 18 cm (direct-scattering region marked in red in Figure 3.1b). The highest dose is due to the source with a radius of ≈13 cm, which is equal to the radius of the “BFO” spherical layer (1 mm layer at 5 cm depth under the phantom surface). It can be seen that dose equivalent from primary particles does not depend on the radius of the spherical shielding.

Primary particles from the ring sources with radii larger than 18 cm rarely hit into the phantom. However, they generate many secondary particles (yellow and violet curves) that hit into the phantom and significantly increase the radiation dose. In this work, we distinguish secondary particles that have a momentum component along the initial propagation direction of the primary particles and address them as “forward-scattered secondary particles” (yellow curves in Figure 4.9). We also address the secondary particles that have a momentum component opposite to the initial propagation direction of the primary particles as “backward-scattered secondary particles” (violet curves in Figure 4.9).

It is interesting to note that the radiation dose due to forward-scattered secondary particles does not change significantly with an increase in ring source radius for sources in the side-scattering region (the region between the black dashed lines) if the shell thickness is lower than 30 g$\cdot$cm^{-2}. This means that an increase in the dose, associated increase in the number of primary particles with an increase in ring source radius is exactly compensated by the decrease in the number of particles scattered in the direction toward the phantom.

Most of the radiation dose due to backward-scattered particles (violet curves in Figure 4.9) is due to the border-scattering region. Together with the dose due to forward-scattered particles it results in the dose increase for the ring sources with approximately the same radius as the inner radius of the spherical shielding (upper black dashed line) if the shell thickness is lower then 30 g$\cdot$cm^{-2}.

A possible reason is that the “actual” shielding thickness (see inset in Figure 4.10) along the initial direction of primary particle propagation is larger for the ring sources with larger radii, as shown in Figure 4.9. More secondary particles are generated in the thicker shield and increase the radiation dose.

Our results provide interesting information about radiation dose due to secondary neutrons. Figure 4.11 demonstrates that most of the secondary neutrons are generated by primary particles that pass away from the phantom and are scattered

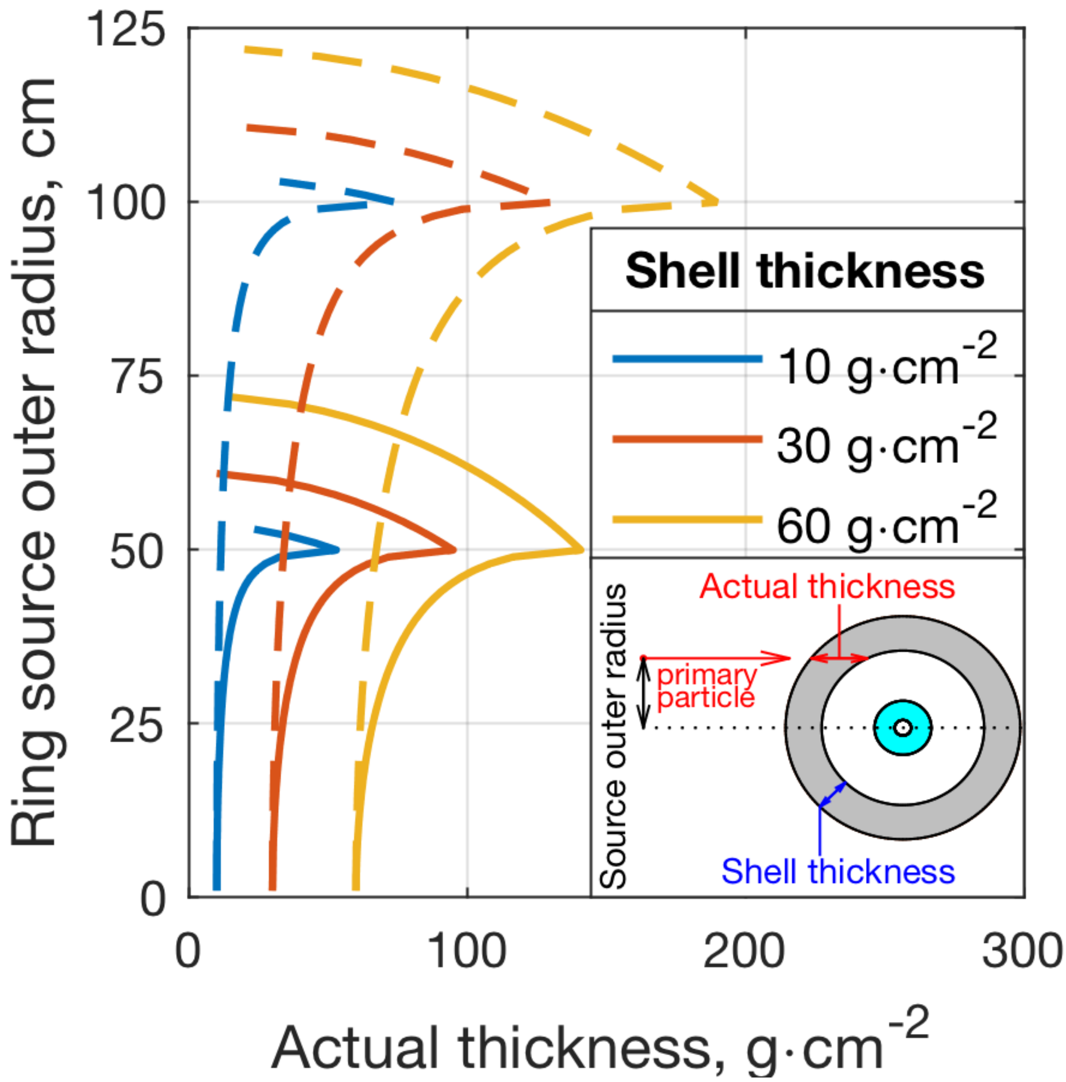

Figure 4.10: Actual shielding thickness along the initial direction of primary particles as a function of the ring source radius. Solid curves show dependences for shielding with an inner radius of 50 cm and dashed curves for a 100 cm inner radius. Dependences for different shielding thicknesses are shown in different colors according to the legend. The inset in the right corner schematically shows the cross-section of the calculation setup. The shell thickness is shown in blue, and the actual shielding thickness along the initial direction of primary particle propagation is shown in red. The figure is published in Dobynde and Shprits, 2019.

in the direction toward the phantom. Moreover, the radiation dose from secondary neutrons increases with an increase in ring source radius and has a maximum around the value of the inner radius of the shielding sphere, where the "actual" shielding thickness is the largest.

In Figure 4.12, we plot the dependence of the radiation dose associated with direct-, side- and border-scattering regions and the resulting total dose as a function

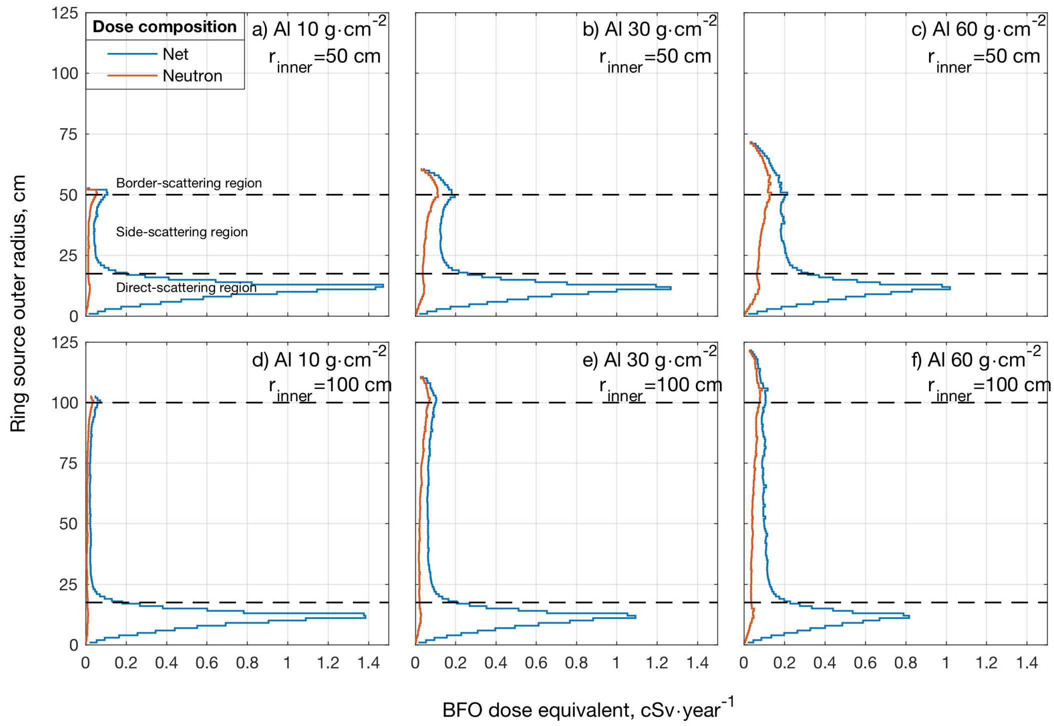

Figure 4.11: Dependence of the BFO dose equivalent due to GCR protons and alpha particles on the ring source radius during the period of the 2001 solar maximum. Dependences for the net dose are shown in blue and for the secondary neutrons in red. Horizontal lines separate direct-, side- and border-scattering regions. The figure is published in Dobynde and Shprits, 2019.

of shield thickness. The dose equivalent associated with the direct-scattering region (the red curve in Figure 4.12a) is higher for the shielding sphere with a radius of 50 cm. In this region, the radiation dose is due to the primary and the secondary forward-scattered particles. The radiation dose due to the primary particles is the same because the actual shielding thickness for both shielding spheres is almost the same. The radiation dose due to the secondary forward-scattered particles is higher for the shielding sphere with a radius of 50 cm. That is because the angular size of the phantom, which is measured from a point on the inner surface of the shielding, is larger in the case of the shielding sphere with the radius of 50 cm than of 100 cm so more secondary particles are scattered toward the phantom and increase the radiation dose. A side-scattering region deposits a slightly higher radiation dose in the case of the shielding with a 100 cm inner radius. This result correlates with a basic estimation based on the angular size of the phantom and the number of primary

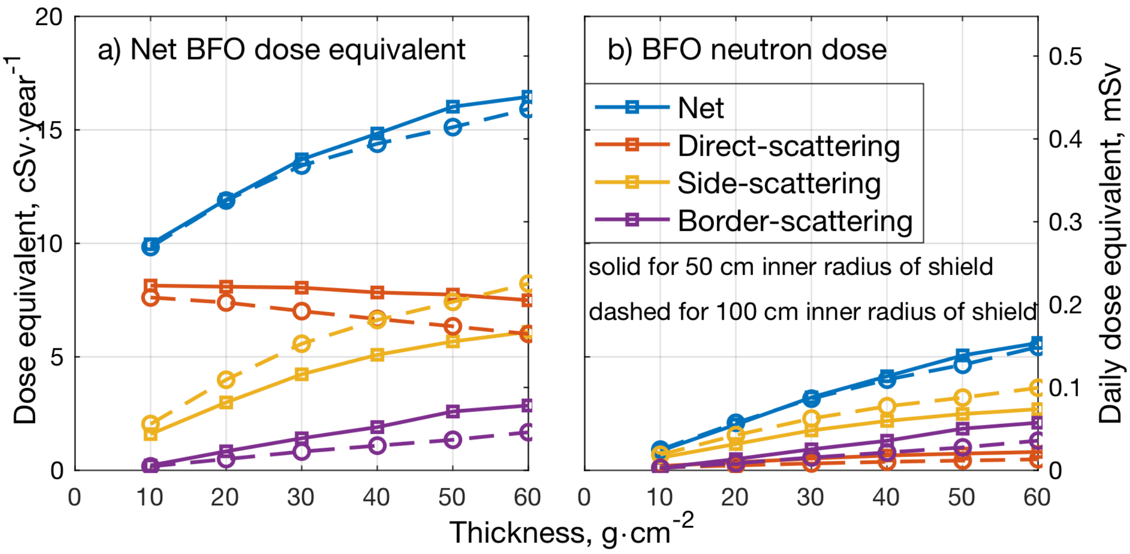

Figure 4.12: Dependence of the net dose equivalent (a) and dose equivalent due to secondary neutrons on the aluminum shielding thickness for shielding with 50 cm (solid curves) and 100 cm (dashed curves) calculated for exposure to GCR protons and alpha particles during the period of the 2001 solar maximum. Different colors show dependences of the net dose and its components on the shielding thickness, according to the legend. The figure is published in Dobynde and Shprits, 2019.

particles coming from the source. Particles from the border-scattering region make a two-times higher dose in the case of the shielding with the 50 cm inner radius because the angular size of the phantom is four times larger and the number of primary particles is two times smaller.

The same differences can be seen in secondary neutron dose dependences (Figure 4.12b). The net neutron dose almost does not depend on the inner radius of the shielding sphere, although the contribution from the side- and border-scattering regions differs. The contribution of neutrons from the direct-scattering region is much smaller than the net BFO dose equivalent from secondary neutrons.

These results are significant to understand the limitations of the widely used methodology of radiation dose calculation that implements depth-dose curves and shielding functions. In this methodology, actual spacecraft geometry is processed into a shielding distribution function using the ray-tracing technique. For each thickness bin of the shielding function, the radiation dose is calculated using quasi-infinite layer geometry. This methodology is widely used to model the radiation dose for realistic spacecraft geometry, as it is much faster than the Monte-Carlo calculations. Unfortunately, side-scattering is excluded from consideration with the main assumption of this method. Namely, particles do not deviate significantly from rays, and the shielding structure does not change significantly around the ray. These conditions work well for thicknesses smaller than $\approx$10 g$\cdot$cm^{-2}, or in the case of small energy of the primary particle (¡ $\approx$500 MeV$\cdot$nucleon^{-1}). These results clearly demonstrate that the methodology of radiation dose calculations using depth-dose curves and shielding functions makes an underestimation of the GCR radiation dose if the shielding thickness is larger than $\approx$10 g$\cdot$cm^{-2}, because of indirect scattering of secondary particles. Result presented in this paper show that the underestimation could reach up to 90% of the actual neutron dose (red curves in Figure 4.12b). However, the shielding function methodology gives a good prediction for the primary GCR particle dose and works well for radiation dose calculations from solar energetic particles and trapped radiation in all thickness regions and GCR dose calculations for shielding thickness lower than $\approx$10 g$\cdot$cm^{-2}.

4.3 LEO orbit as a natural lab for studying biological risks during the flight to Mars and after

This section presents results of radiation exposure due to GCR during an interplanetary flight and flight along ISS orbit calculated with spherical geometry setup irradiated with circular source.

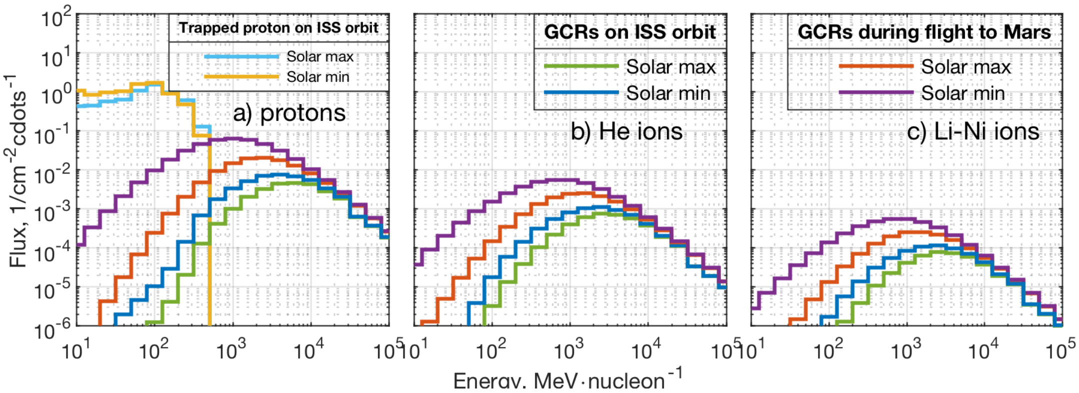

Figure 4.13: Binned integrated particle spectra in the near-Earth interplanetary space and on the actual ISS orbit during different phases of solar activity.

Figure 4.13 shows the binned integral spectra of primary particles for GCR protons and TP(a), helium ions (b), and all ions from lithium to nickel (c). The GCR flux variation associated with the solar activity is significant at energies lower than ≈10 GeV·nucleon^{-1}. At the same phase of the solar cycle, GCR fluxes on the ISS orbit (green and blue lines) are lower than in the near-Earth interplanetary space (red and violet lines). At high energies over ≈10 GeV·nucleon^{-1}, the total fluxes differ by a factor of 0.7. “High-energy” GCR particles are almost unaffected by the magnetic field of the Earth at the scale of the radius of the Earth, and the difference is due to the “geometric shielding” of the Earth. The angular size of the space Ω_{shielded} covered with the Earth as seen from the ISS, can be calculated from the geometric position of the ISS as follows:

$$\Omega_{\text{shielded}} = 2\pi R_{\text{ISS}} \left(R_{\text{ISS}} - \frac{{R_{\text{ISS}}}^2}{R_{\text{Earth}} + H_{\text{ISS}}} \right) \tag{4.1}$$

where R_{Earth} is the radius of the Earth, H_{ISS} is the altitude of the ISS, and R_{ISS} is the distance between ISS position and the touchpoint of a tangent line build from the position of the ISS to the Earth:

$$R_{\text{ISS}} = \sqrt{(R_{\text{Earth}} + H_{\text{ISS}})^2 - R_{\text{Earth}}{}^2} \tag{4.2}$$

Being divided by 4π it results in ≈ 0.7, depending on H_{ISS} and R_{Earth}.

At the energies lower than 10 GeV·nucleon^{-1}, the difference in the GCR fluxes is higher because of the deflection of the GCR particles by the Earth's magnetic field. The minimal possible difference is between GCR spectra in the interplanetary space during solar maximum and GCR spectra on the ISS orbit during solar minimum. Potentially, modifying the trajectory on LEO, increasing orbit inclination, or altitude might reduce the difference. However, trajectory optimization would be addressed in future research. Besides GCR, the trapped proton radiation should be taken into account on the ISS orbit. The spectra of trapped protons decay exponentially with the particle energy. It significantly increases the net proton spectra at energies up to $\approx$450 MeV (yellow and cyan lines). In the following, we consider dose dependences on the aluminum shielding thickness in the interplanetary space during solar maximum and on the ISS orbit during solar minimum. Figure 4.14a

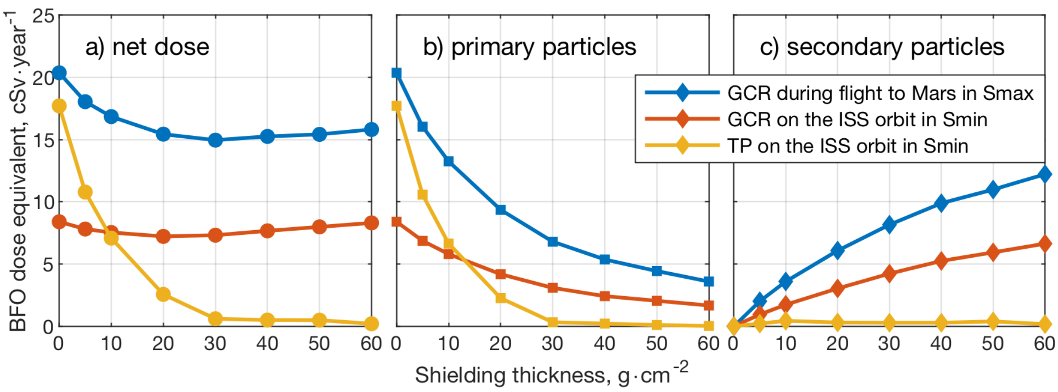

Figure 4.14: Dependences of the BFO dose equivalent on the shielding thickness in the near-Earth interplanetary space during solar maximum and the ISS orbit during solar minimum.

shows the dependence of the BFO dose equivalent on the shielding thickness. The BFO dose equivalent was calculated in a 1 mm layer at a distance of 5 cm under the phantom surface. The difference in the net BFO dose (Figure 4.14a) in interplanetary space and on the ISS orbit is significant behind thin shielding up to 30 g·cm^{-2}.

The difference is due to the dose from primary particles (Figure 4.14b) resulting from the difference in GCR fluxes at low energies and due to the trapped proton contribution at the ISS orbit.

Aluminum shielding of 30 g·cm^{-2} efficiently stops trapped proton (yellow curve) and reduces the dose from primary GCR particles. Secondary particles induced by GCR (Figure 4.14c) make a major contribution to the radiation dose behind shielding of 30 g·cm^{-2} and thicker. The difference in GCR fluxes in interplanetary space and on the ISS orbit is of a ≈0.7 factor at energies over ≈10 GeV·nucleon^{-1} and larger at lower energies. These differences in spectra result in a twice-higher BFO dose equivalent in the interplanetary space comparing to the ISS orbit. Thus, it can be concluded that the radiation dose equivalent accumulated in BFO during a 1-year flight to Mars during solar minimum is approximately equal to that of a ≈2-year flight on the ISS during solar maximum. To examine the identity of the radiation environment behind 30 g·cm^{-2} shielding, we next show the dependence of the dose equivalent on the particle energy for different species of particles.

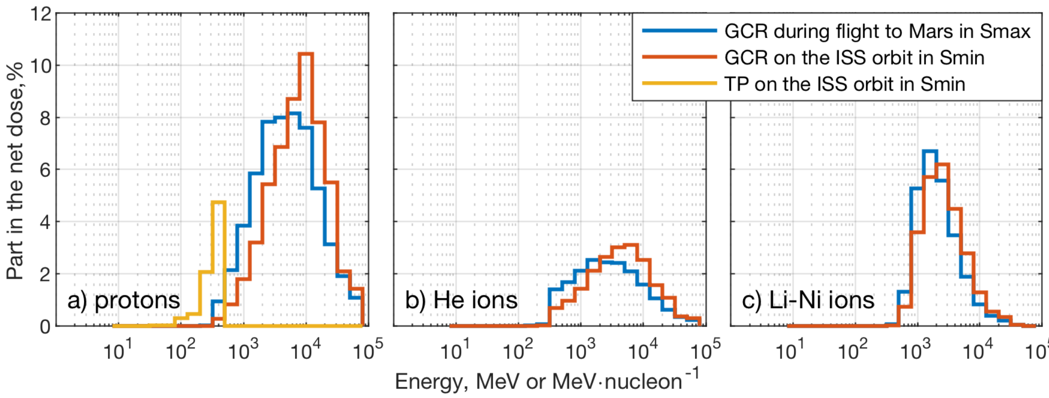

Figure 4.15: Binned integral contribution to the net BFO dose equivalent behind 30 g·cm^{-2} aluminum shielding as a function of primary particle energy.

Figure 4.15 shows the contributions to the BFO dose equivalent behind aluminum shielding of 30 g·cm^{-2} as a binned integral dependence on the primary particle energy. The dose equivalent distributions for helium and heavier ions are very similar to each other. The dose equivalent dependence of protons on the ISS orbit is modified by the trapped protons (yellow line). However, behind 30 g·cm^{-2} shielding, trapped protons contribute ≈7% to the net BFO dose equivalent. This contribution is higher behind thinner shielding and is lower behind thicker shielding.

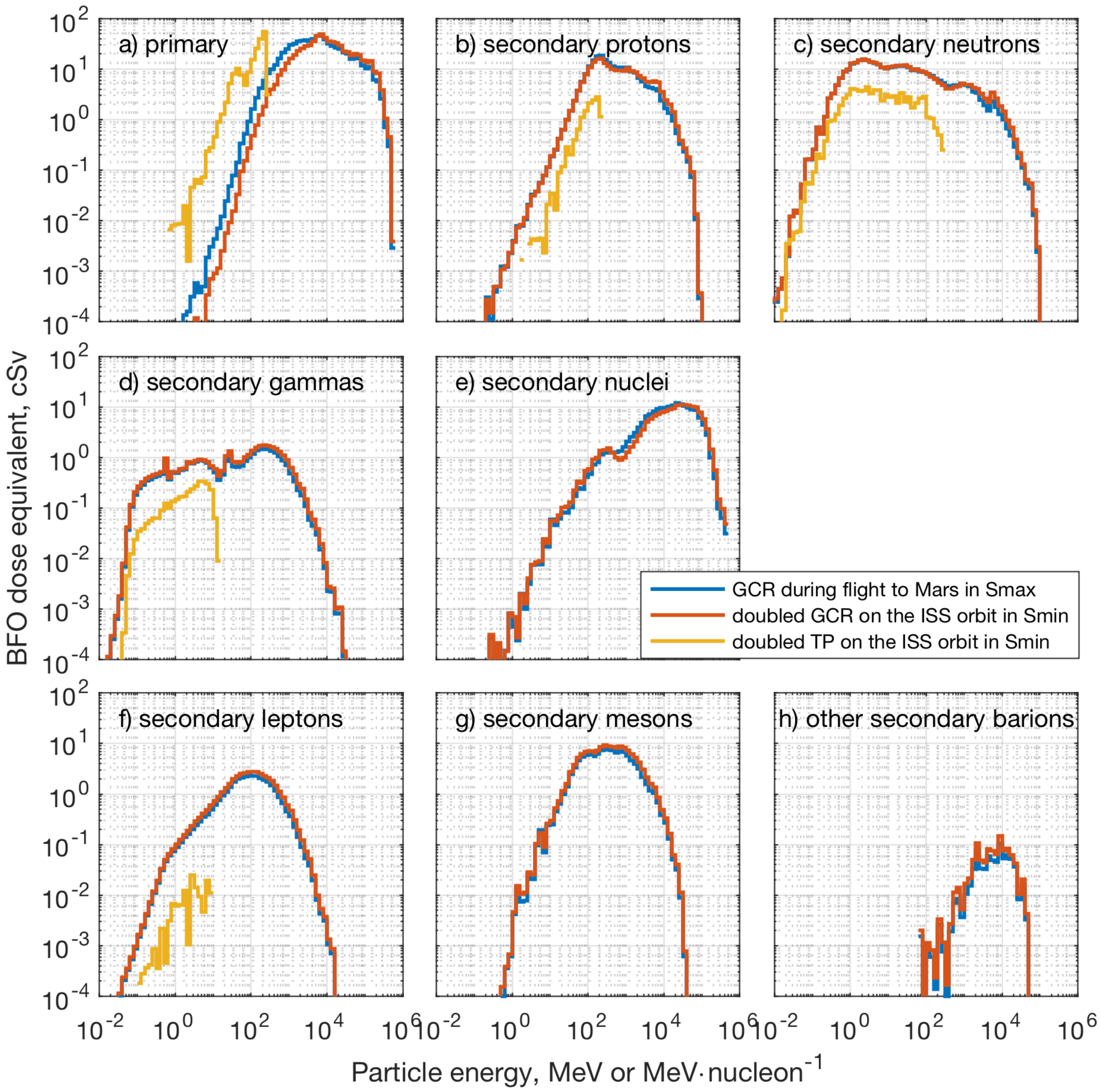

Figure 4.16: Binned integral dose equivalent distribution over particle energy for all particle species that hit the phantom behind 30 g·cm^{-2} aluminum shielding.

Figure 4.16 shows the binned integral BFO dose equivalent spectra for all species of radiation particles, which hit the phantom shielded with 30 g·cm^{-2} aluminum shell. All particles are divided into primary and secondary particles, which have been produced in the shielding: protons, neutrons, gammas, nuclei, leptons, mesons, and other baryons. The dependences for the secondary particles (except nuclei) are almost the same for the ISS orbit and the interplanetary space. The largest differences are in the dependencies of the primary particles and secondary nuclei. The differences are due to the differences in the primary particle flux spectra.

The results in Figure 4.13 show that the best match in radiation particle spectra on the way to Mars during solar minimum is with the radiation particle spectra on the ISS orbit during solar maximum. In section 4.1, it is shown that the optimal thickness for GCR shielding during the interplanetary flight is 30 $g{\cdot}cm^{-2}$. The results in Figure 4.14a demonstrate that the same net BFO dose equivalent is accumulated during the 1-year flight to Mars and a 2-year flight on the ISS orbit if the aluminum shielding exceeds 30 $g{\cdot}cm^{-2}$. Figures 4.14b and c show that the secondary radiation deposits most of the BFO dose equivalent behind such shielding. The most significant differences in the net BFO dose equivalent are associated with trapped proton radiation on the ISS orbit. Most energetic trapped protons make up 7% of the BFO dose behind 30 $g{\cdot}cm^{-2}$ aluminum shielding, as shown in Figure 4.15. The detailed comparison of the BFO dose equivalent spectra shows that they are very similar for all species of secondary radiation. The largest differences are in the BFO dose equivalent spectra of primary particles at the energies up to 300 $MeV{\cdot}nucleon^{-1}$ and are related to the trapped proton radiation. The shielding distribution on the ISS strongly depends on the position of the phantom and its orientation (see section 3.3 and 4.4). For points that are the most distant from the module walls, the shielding distribution is Gaussian-like, with a median shielding of $\approx$30 $g{\cdot}cm^{-2}$. Near the module wall, the shielding distribution is anisotropic with two peaks at $\approx$5 $g{\cdot}cm^{-2}$ and 60 $g{\cdot}cm^{-2}$. Near the module wall, there is also a significant contribution from trapped protons, but in the middle of the station, irradiation conditions are similar to the interplanetary space.

The net dose rates measured by RAD (Hassler et al., 2014b) during the interplanetary flight and on the Mars surface differ by a factor of two. The same difference is found between interplanetary space and the ISS orbit, so radiological experience obtained on the ISS could potentially be transferred to the base on the Mars surface.

4.4 Radiation dose assessment on the surface of phantom during MATROSHKA-R space experiment

This section presents depth-dose curves calculated using slab geometry setup along actual ISS orbit for GCR and TR, and calculations of radiation exposure in MATRESHKA-R experiment.

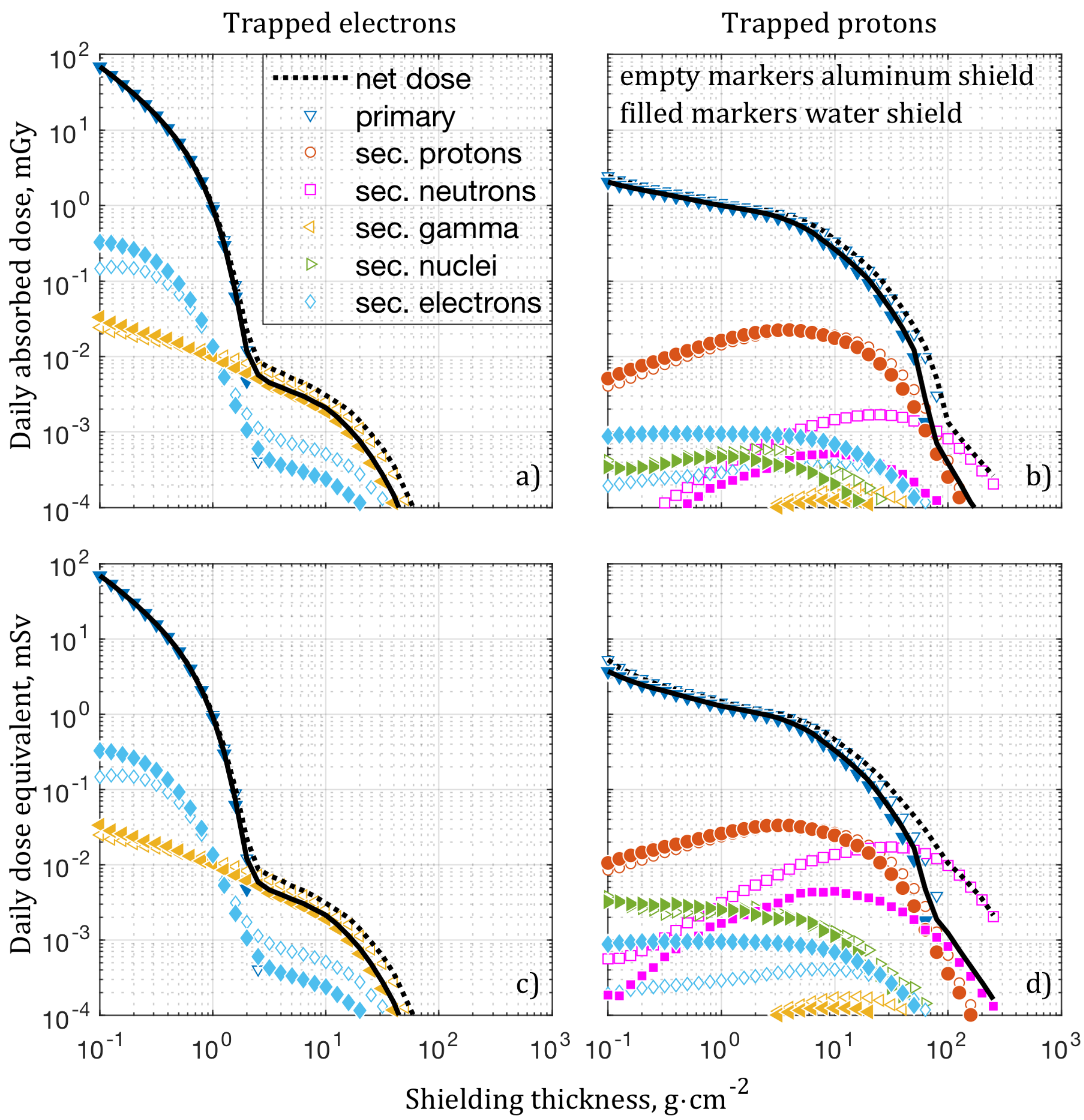

Figure 4.17: Calculated trapped radiation depth-dose curves on the ISS orbit behind aluminum-only (dotted curve for the net dose and empty markers for components) and water-only shielding (solid curve for the net dose and filled markers for components) averaged over the second session of the MATROSHKA-R experiment for absorbed dose (a,b) and dose equivalent (c,d) for trapped electrons (a,c) and trapped protons (b,d). The figure is published in Dobynde et al., 2019.

Depth-dose curves for trapped radiation are shown in Figure 4.17. For both trapped protons and electrons, there is a boundary thickness value, where primary particle and secondary particle radiation doses are equal. By primary, we mean space radiation particles, and by secondary, we mean any particle generated in the geometry setup. Primary particle radiation is dominant behind shielding that is thinner than the boundary, and secondary radiation is dominant behind thicker shielding. Trapped electrons (Figure 4.17a,c) produce secondary gamma and electrons that have a quality factor of 1, so the boundary thickness values for the absorbed dose (Figure 4.17a) and dose equivalent (Figure 4.17c) coincide and are equal to 2 $g{\cdot}cm^{-2}$. Aluminum-only shielding is less efficient in attenuating primary electrons (empty blue triangles), comparing to shielding with a fraction of water. 2 $g{\cdot}cm^{-2}$ aluminum-only shielding produces more gammas (empty yellow triangles) compared to water-only shielding (filled markers). As a result, water-only shielding attenuates the net dose better than aluminum, although behind water shielding with a thickness up to 1 $g{\cdot}cm^{-2}$ the dose from secondary electrons (filled cyan diamonds) is higher than behind aluminum-only shielding.

For trapped protons, the boundary value differs for absorbed dose (Figure 4.17b) and dose equivalent (Figure 4.17d) and also depends on the shielding material. For aluminum-only shielding, boundary thickness values are 100 $g{\cdot}cm^{-2}$ for the absorbed dose and 50 $g{\cdot}cm^{-2}$ for the dose equivalent. The difference is mostly due to the secondary neutron radiation (magenta squares) that has a high radiation quality factor. Secondary neutrons also increase the dose equivalent behind aluminum-only shielding compared to water-only shielding. It is also interesting to note that the dose from secondary electron radiation is higher behind water-only shielding (filled cyan diamonds).

The depth-dose curves depend on the fraction of aluminum in the net shielding (Figure 4.18). For the same shield thickness, the smallest dose is behind water-only shielding (green crosses), and the largest dose is behind aluminum-only shielding (blue triangles). The difference between curves depends on the shielding thickness: the larger the shielding thickness, the greater is the difference in depth-dose

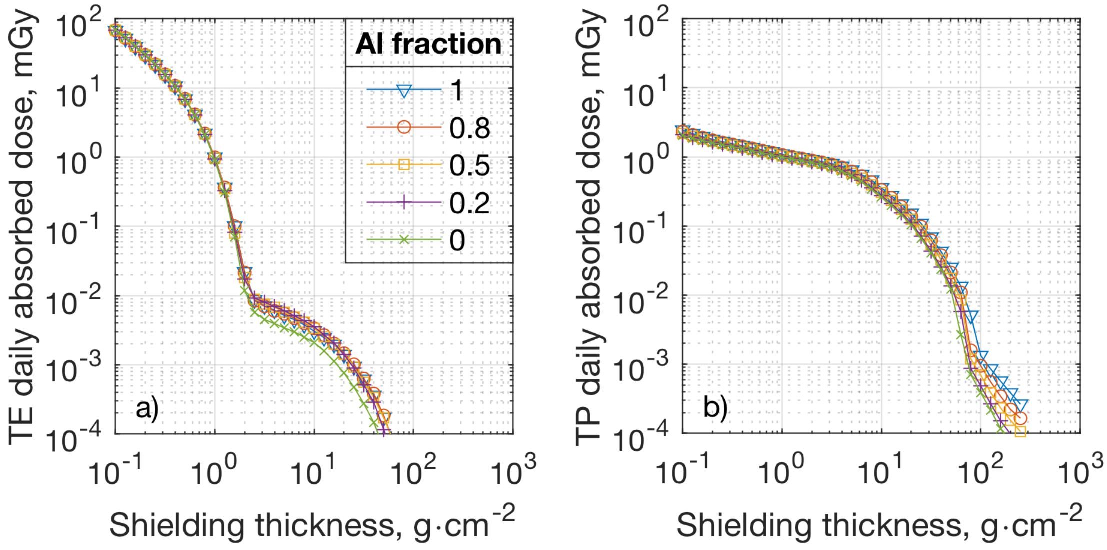

Figure 4.18: Calculated depth-dose curves on ISS orbit averaged over the second session of the MATROSHKA-R experiment for trapped electrons (a) and trapped protons (b). Depth-dose curves for different shielding compositions are shown in different colors. The figure is published in Dobynde et al., 2019.

curves. For trapped electrons, the difference in absorbed dose behind water-only and aluminum-only shielding is 6% behind 1 g·cm^{-2}, 20% behind 10 g·cm^{-2} and 91% behind 100 g·cm^{-2}. The trapped electron radiation dose values are minimal behind 1 g·cm^{-2} shielding and thicker, so it does not have a significant contribution to the net radiation dose value in the considered geometry model. The difference in the trapped proton depth-dose curves also increases with shielding thickness and is 3% behind 1 g·cm^{-2}, 15% behind 10 g·cm^{-2} and 86% behind 100 g·cm^{-2}. The dependence of the absorbed dose on the shielding composition is more critical for trapped proton radiation because the net shielding varies in the range from 3 g·cm^{-2} to 200 g·cm^{-2} (Figure 3.3b-1).

The second main component of the radiation on the ISS orbit is GCR. Depth-dose curves for GCR (Figure 4.19) are different from the trapped radiation. Primary GCR particles (blue triangles) have major contributions to the net radiation dose behind shielding thinner than 10 g·cm^{-2}. In the thickness range from 0.1 g·cm^{-2} to 1 g·cm^{-2} the radiation does not depend on the shield thickness, because of the high kinetic energy of GCR particles. Behind shielding thicker than 1 g·cm^{-2} the radiation dose from primary particles decreases with increasing shielding thickness.

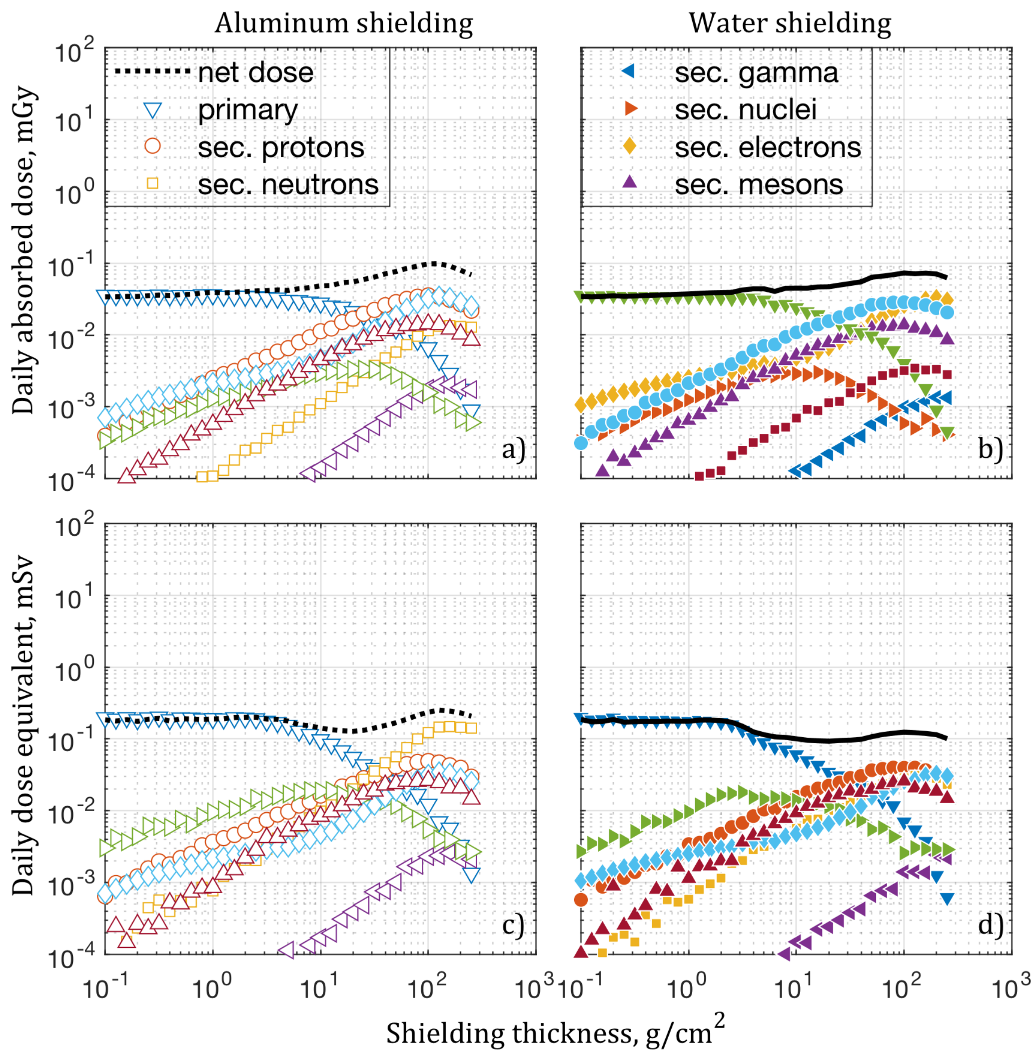

Figure 4.19: Calculated GCR depth-dose curves on the ISS orbit behind aluminum-only (a,c) and water-only shielding (b,d) averaged over the second session of the MATROSHKA-R experiment, for absorbed dose (a,b) and dose equivalent (c,d). The net dose is shown with black lines. The contribution of primary particles is shown with blue triangles and of secondary radiation particles specified in the legend. The figure is published in Dobynde et al., 2019.

The net absorbed dose (black curves in Figure 4.19a,b) increases with the increase in shield thickness in the range from 0.1 g·cm^{-2} to 150 g·cm^{-2} and then decreases for larger thicknesses. This increase is due to the increased amount of secondary particles, mainly protons (red circles) and electrons (cyan diamonds) that are generated in the shielding. Secondary particles have major contributions to the net absorbed dose behind shielding thicker than 10 g·cm^{-2}. The absorbed dose from secondary neutrons (magenta squares) is maximal behind approximately 150 g·cm^{-2}

shielding but is significantly lower than other secondary particles. Secondary radiation components are slightly lower behind water shielding (Figure 4.19b) than behind aluminum shielding (Figure 4.19a), except for the neutron component (magenta squares) that is significantly lower behind water shielding.

The net depth-dose equivalent (black curves in Figure 4.19c,d) has a local minimum around 20 g$\cdot$cm^{-2}, which correlates with the local minimum position in previously reported results Mrigakshi et al., 2013 Slaba et al., 2017. This minimum is a result of the decrease in primary particle dose (blue triangles) and increases of secondary radiation with the increase in thickness. Same trends cause the increase in the absorbed dose dependences on the thickness (Figure 4.19a,b), but because of the high-quality factor, the dose equivalent of primary particles in the low-thickness region is much higher than the dose equivalent of secondary particles.

Secondary neutrons (magenta squares) make up to 50% of the GCR dose equivalent behind aluminum shielding (Figure 4.19c) thicker than 100 g$\cdot$cm^{-2}. The net dose equivalent value behind 100 g$\cdot$cm^{-2} aluminum shielding exceeds the dose equivalent behind the smallest presented aluminum shielding of 0.1 g$\cdot$cm^{-2}. Behind water shielding (Figure 4.19d), the contribution of secondary neutrons to the dose equivalent is much smaller. It is of the same order as secondary protons (red circles), secondary electrons (cyan diamonds), and secondary mesons (purple triangles). There is also a maximum in the net dose behind water shielding of around 100 g$\cdot$cm^{-2}, but it is lower than the dose behind 0.1 g$\cdot$cm^{-2} water shielding.

Depth-dose curves for different values of the aluminum fraction in the net shielding are shown in Figure 4.20. For the same net thickness, the radiation dose is lower behind the shielding with a lower fraction of aluminum. The largest difference in the absorbed dose (Figure 4.20a) is between 100 g$\cdot$cm^{-2} water-only and aluminum-only shielding. The differences are more significant in the depth-dose equivalent curves (Figure 4.20b). There are notable differences in the dose equivalent dependencies for a shielding thicker than 10 g$\cdot$cm^{-2}. The largest dose equivalent is behind aluminum-only shielding (blue triangles). Reducing the aluminum fraction in the net shielding

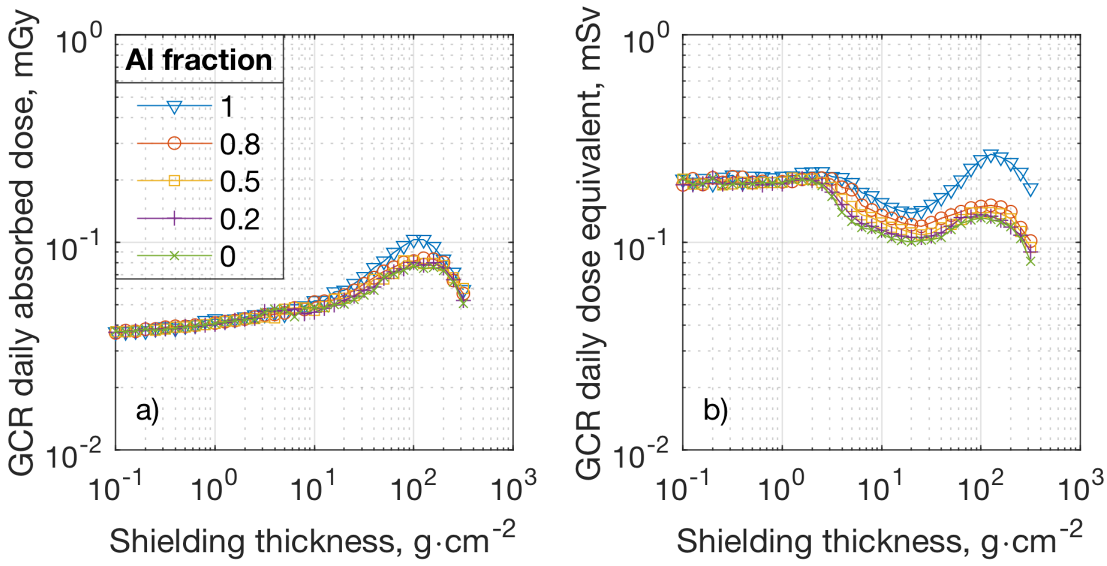

Figure 4.20: Calculated GCR depth-dose curves on ISS orbit averaged over the second session of the MATROSHKA-R experiment for absorbed dose (a) and dose equivalent (b). Depth-dose curves for different shielding compositions are shown with a different color. The figure is published in Dobynde et al., 2019.

down to 0.8 (red circles) significantly reduces the dose equivalent value. Further decreases of the aluminum fraction reduce the dose rates but not significantly. The large difference between aluminum-only and 0.8 aluminum shielding is due to the reduction of the dose from secondary neutrons. Secondary neutrons have a significant contribution to the net dose equivalent behind aluminum-only shielding thicker than 10 g·cm^{-2}, up to a half of the net dose equivalent behind 100 g·cm^{-2} shielding (Figure 4.19b). The increase of the water fraction in the net shielding from 0 to 0.2 decreases the number of generated neutrons and effectively stops neutrons generated in the aluminum layer.

Figure 4.21a shows the binned dependencies of the absorbed dose on the shielding thickness for points 3 and 18. The vertical dashed lines show the median net dose equivalent. The vertical solid lines show the median net shielding i.e., half of the rays have a shielding greater than this value. We will call the thickness region up to median the low-thickness region and the thickness region greater than the median shielding the high-shielded region. Trapped proton radiation has a significant contribution to the radiation dose in point 18 that is closest to the shell. Trapped proton radiation is also dominant in the low-thickness region of point 3 that is most

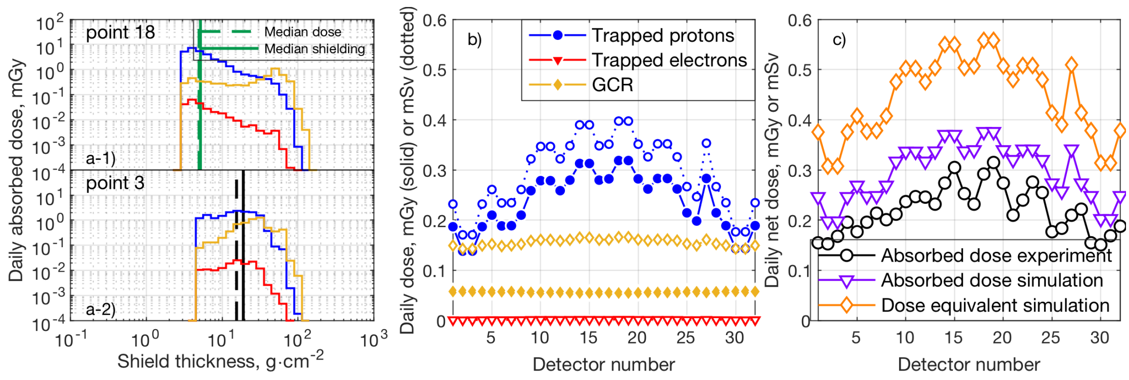

Figure 4.21: (a) Calculated binned absorbed dose (legend on Figure 4.21b) on the ISS orbit during the second session of the MATROSHKA-R experiment. Vertical lines show the median level of the net shielding (dashed) and the median level of the net dose (solid) for point 18 that is closest to the shell (green lines), and for point 3 that is the most distant from the shell (black lines). (b) Calculated absorbed dose (solid curves) and dose equivalent (dotted curves) components distribution on the phantom's surface. (c) Net dose distribution on the phantom's surface without neutron contribution. Experimental data error is within 10% Kartashov and Shurshakov, 2018. The figure is published in Dobynde et al., 2019.

distant from the shell. However, in the high-shielded region, doses of GCR and trapped protons are approximately equal. The radiation dose from trapped electrons (red triangles) is only a minor contribution to the net dose. Figure 4.21b shows the calculated absorbed dose (filled markers) distribution at the phantom's surface. The trapped electron contribution (red triangles) is the smallest, and its dose does not affect the net dose significantly. The GCR dose (yellow diamonds) slightly increases in points with high shielding (detectors 1-5 and 27-32) and increases behind less shielded regions (detectors 6-26). The GCR absorbed dose is 0.06 mGy·day^{-1}, which is equal to the value obtained by Gustafsson et al., 2010. The absorbed dose from trapped protons (blue circles) is the most modulated. The trapped proton dose is larger in low-shielded points (detectors 9-24) and smaller in high-shielded points (detectors 1-5 and 27-32), opposite to the radiation dose from GCR.

Our simulations also give the composition of the dose equivalent (empty markers on Figure 4.21b) that were not measured in the experiment. It can be seen that the GCR contribution to the net dose equivalent is higher than the absorbed dose. In most shielded points, it is equal to 45%. The average quality factor is 1.3 for trapped protons and 2.7 for GCR.

Figure 4.21c show the experimentally determined (black circles) and calculated (green squares) absorbed dose and the dose equivalent (cyan diamonds) distribution at the surface of the tissue-equivalent spherical phantom. The neutron contribution was not measured in this experiment session. The calculation results of surface dose distribution are also presented without a secondary neutron contribution. It can be seen that the simulation results are in good agreement with the experimental results. Calculated dose values are, on average 20% greater than the measured ones. This is likely due to the described trapped protons in the AP8 model. The AP8 model provides proton spectra for earlier phases of the solar cycle activity. The largest overestimation is in points 1, 5, 9, 13, 17, 21, 25, and 29 that are located on the phantom's bottom (Fig 3.3a). The overestimation can be caused by the module geometry simplification and the exclusion of other modules from the geometry model. The maximal radiation dose is detected in points that are closest to the ISS shell; the smallest dose is found in the most distant points. The difference between the maximum and minimum dose rate is around a factor of 2 for both experiment and simulation results. Unlike the experimental results, the calculated radiation dose has a high symmetry about points 16-17, which originates from the simulation setup symmetry. A possible cause can be a potential mismatch between the phantom orientation in the experiment and the simulation model, and between the simulation, ISS model geometry compared to the real ISS geometry.

The method we applied for dose calculations has two main scopes for further improvement. The first is the main assumption of the ray-tracing method that the radiation dose is deposited only by particles that travel along the rays to the point of interest. The second is that depth-dose curves were calculated in geometry without back shielding, so there is no dose of particles scattered from back shielding. These issues can result in underestimation of the dose from GCR inside a heavily shielded spacecraft. For the dose estimations on the ISS, the current versions of ray-tracing and depth-dose curves predict the radiation dose with good accuracy, except for the neutron dose. The neutron dose is underestimated at least by a factor of 2, comparing to results by Koshiishi et al., 2007 and by Machrafi et al., 2009. The method should be improved for precise calculations of the secondary neutron dose.

4.5 Improvement of the ray-tracing method for dose calculation in near-surface phantom layers or the case of strongly inhomogeneous shielding

This section presents a lateral spread of energy deposition calculated with slab geometry setup and its implementation with an improved ray-tracing method for calculating dose distribution in spherical phantom.

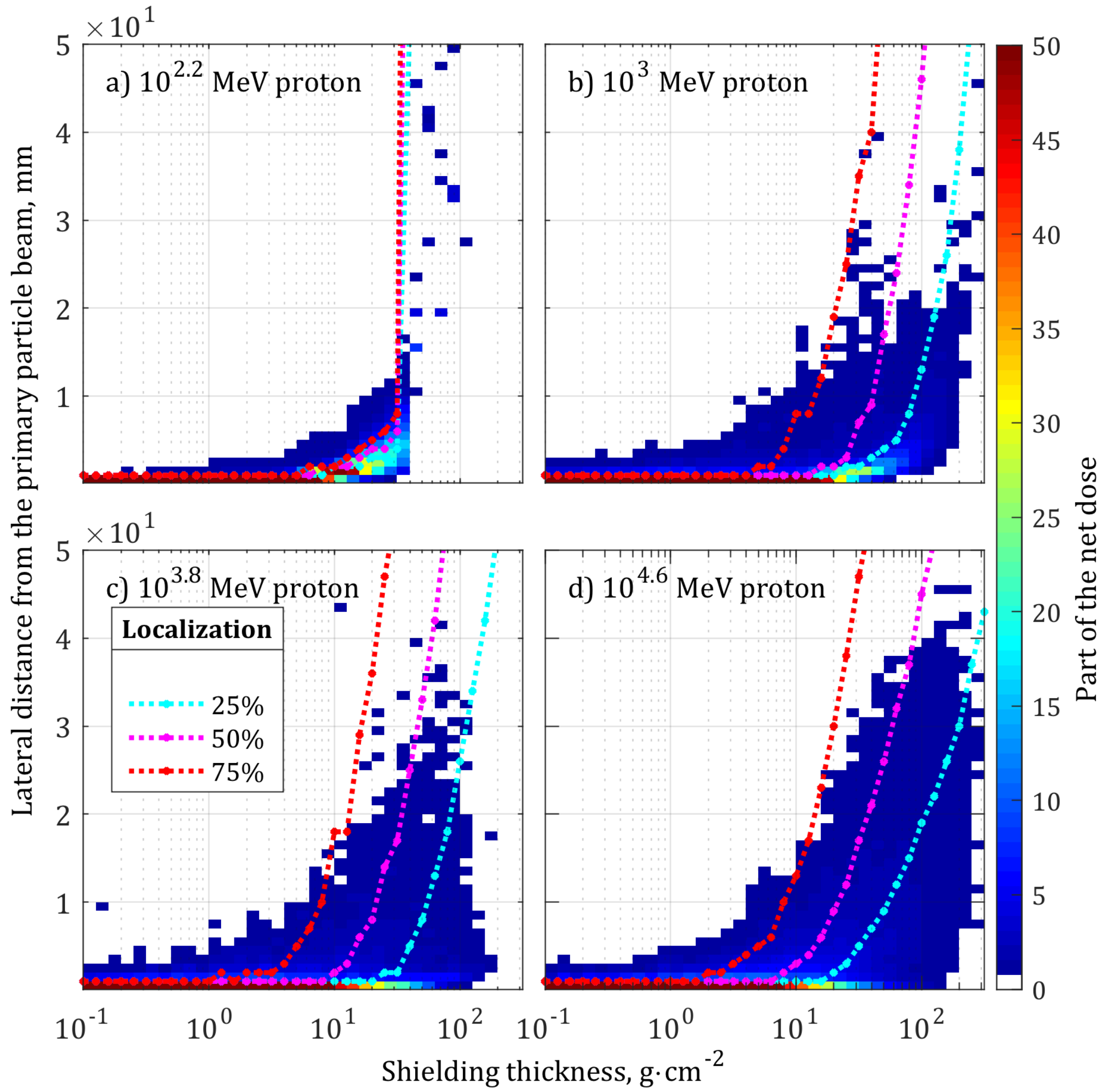

Figure 4.22: Radial dose distribution in detector water plate behind aluminum shielding of different thickness created with $10^{2.2}$ MeV protons (a), 10^3 MeV protons (b), $10^{3.8}$ MeV protons (c), and $10^{4.6}$ MeV protons (d).

It can be seen in figure 3.3b that high-energy protons have a complex track structure with a lot of secondary particles, which hit the detector water slab at a distance from the initial primary particle detector. This "energy diffusion" is due to secondary particles and increases with the increase of primary particle energy and shielding thickness. Figure 4.22 shows calculated energy diffusion as a function of shielding thickness and primary proton energy. Dotted lines show localization of the dose with a step of 25% of the net deposited dose. Deposited energy is localized near the initial direction for all presented proton energies if shielding thickness is less than ≈2 g·cm^{-2}. It means that the main assumption of the ray-tracing methodology is satisfied, and the method could be applied. If the shielding thickness exceeds 2 g·cm^{-2}, the deposited energy is distributed near the initial direction. For the same shield thickness, the higher is the particle energy, the large is localization area. Protons with energy about 10 GeV (energy bin with the maximal GCR radiation dose (see figure 4.15)) deposit only 25% of the net dose near their initial momentum direction after passing through a 30 g·cm^{-2} aluminum shielding (that is the average estimate for a spacecraft shielding thickness). It means that for this energy and thickness combination the main assumption of the ray-tracing method is not satisfied.

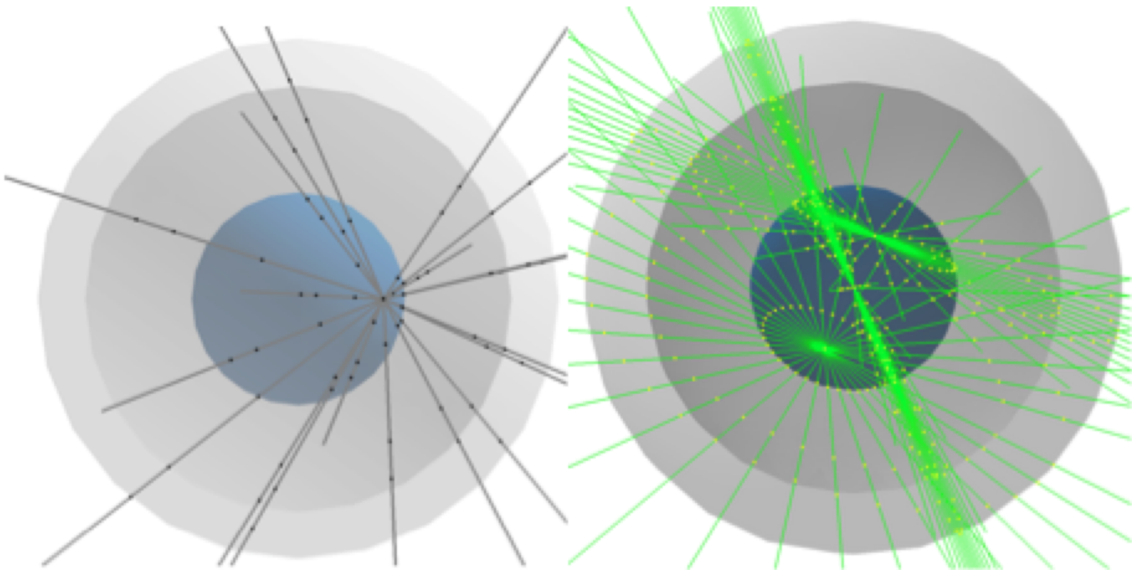

Figure 4.23: Geometry processing (a) in the regular ray-tracing methodology and (b) in extended ray-tracing methodology.

Figure 4.5 shows the dose equivalent as a function of the ring source radius. However, there is a way to improve the ray-tracing method to take into account this energy diffusion. Figure 4.23a shows a regular ray-tracing method when rays are traced from the point of interest in all directions to define the shielding-distribution function. Now, to take into account energy diffusion shown in figure 4.22 one needs to consider rays that start from the points on regular rays and are perpendicular to them, as shown in figure 4.23b. Shielding thickness and composition is determined along each new ray and radiation dose at the corresponding distance is added to the dose in the point of interest.

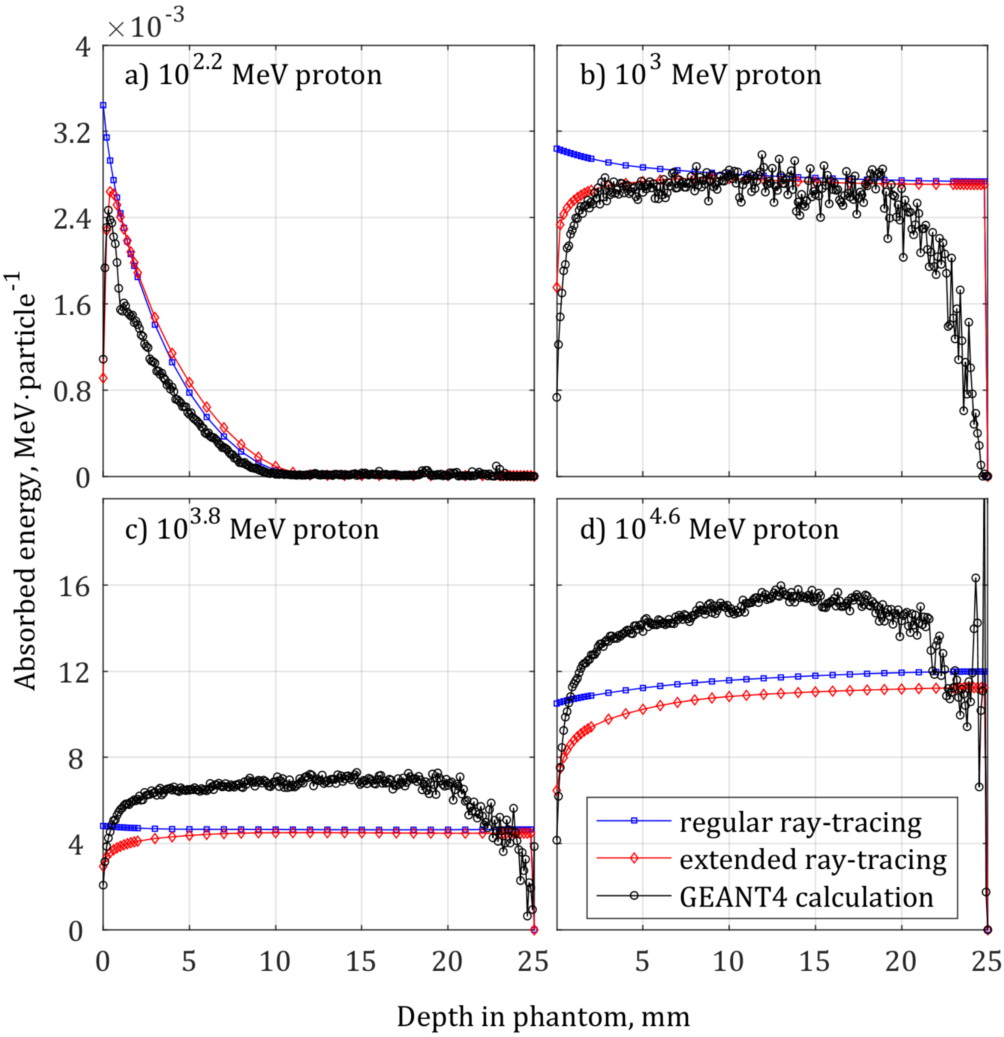

Figure 4.24: Radial dose equivalent distribution in the spherical water phantom created with $10^{2.2}$ MeV protons (a), 10^3 MeV protons (b), $10^{3.8}$ MeV protons (c), and $10^{4.6}$ MeV protons (d) and calculated with different methods listed in the legend

Figure 4.24 shows dose equivalent distribution inside water phantom shielded with 30 g·cm^{-2} aluminum sphere. The direct GEANT4 Monte-Carlo calculations predict a decrease of the radiation dose in the near-surface phantom layers comparing to the inner layers. The contribution of side-scattered particles is excluded, as it cannot be described even with the improved ray-tracing method. It can be seen that the regular ray-tracing method reproduce the dose distribution inside the phantom, but overestimate it near the surface. In contrast, improved ray-tracing repeat dose decrease in the near-surface layer. In contrast to the regular ray-tracing, it requires to define shielding and composition along more rays and more calculation time. However current progress in hardware development makes this improved method perspective for radiation dose calculations: it is significantly faster then Monte-Carlo codes and has a better precision comparing to regular ray tracing.

Chapter 5

Conclusions

The main goal of the provided work was to develop a method to significantly reduce radiation exposure of astronauts due to GCR, SEP, and TR during space flights. The complexity of the problem required to select the most important aspects. The results of the work give answers to five questions selected in the beginning:

- determination of the optimal combination of launch dates and spacecraft shielding to allow the longest possible mission duration before reaching the radiation dose limit of astronauts;
- calculation of the relative contributions of the different species to the net radiation dose and their dependence on spacecraft shielding;
- quantitive comparison of the radiation environment within a spacecraft, flying inside and outside of the Earth magnetosphere;
- calculation of depth-dose curves for urgent dose assessment and its validation;
- definition of the limitations of the depth-dose method in terms of particle energy and shielding thickness.

Results, methods, and skills obtained during the work can now be applied to address more specific but also important questions of radiation protection, like:

- considering hydrogen-rich composite materials for usage instead and in addition to conventional materials used in spacecraft to reduce radiation exposure of astronauts;
- modeling radiation exposure in a realistic model of the spacecraft using a combination of Monte-Carlo and shielding function methods to reduce calculation time keeping a high level of assessment precisions;

- transition from post-flight dose assessment to real-time monitoring and forecasting.

All parts of the work are either already published (second and fourth) or are under review in journals (first and third) or would be published after extra work (fifth).

One of the main outcomes of the work is defining optimal conditions for the space flight. A long-duration interplanetary crewed flight should be scheduled for the period of solar maximum at the decay phase to reduce the influence of GCR and SEP radiation. Spacecraft shielding should be thick enough (≈20-30 g·cm^{-2}) for efficient attenuation of SEP radiation, but not be thicker than ≈30 g·cm^{-2} to prevent the production of secondary particles (mainly neutrons). For the previous solar cycle, these flight conditions allow a 5.5-year flight before reaching the career expose limit of 1 Sv. If the career exposure limit were reduced in the future, the maximum flight time would be shorter, while the optimal flight conditions would be the same.

For most SEP, the radiation dose is due to primary particles. However, if the SEP spectrum has a significant component of ≈1 GeV particles, the radiation dose due to this event cannot be reduced down to zero even with 60 g·cm^{-2} aluminum shielding. The influence of SEP spectrum is nicely shown with plots in figure 1.2 and 4.2b. Radiation dose due to "larger" event in November 2000 can be reduced with aluminum shielding to smaller values than dose due to "smaller" but more "energetic" event in January 2005. It is demonstrated that most of the GCR dose equivalent is created with heavy GCR particles (Z>2) if the aluminum shielding is lower than ≈10 g·cm^{-2}, due to radiation dose from primary particles. Light GCR particles (protons and alphas) make most of the dose equivalent if the shielding thickness is larger than ≈10 g·cm^{-2}, due to radiation dose from secondary particles.

Skin and lightly self-shielded organs are exposed to higher doses, than BFO or CS. This work shows that the skin dose equivalent due to GCR is minimal behind 30 g·cm^{-2} aluminum shielding at any phase of solar activity. The dependences of average and BFO dose equivalent on thickness have a local minimum at 30 g·cm^{-2} only during solar maximum. During solar minimum, the average and BFO dose equivalent are constant behind shielding greater than 30 g·cm^{-2} and significantly higher than during solar maximum. The BFO radiation dose is mostly created with secondary protons, neutrons, and mesons if the shielding thickness is over ≈30 g·cm^{-2}. Even if the BFO dose equivalent is the same behind shielding of 30 g·cm^{-2} and 60 g·cm^{-2} of aluminum, the radiation dose due to secondary neutrons is twice higher behind 60 g·cm^{-2} shielding.

Most of the secondary neutron dose equivalent behind shielding thicker than ≈30 g·cm^{-2} is due to "indirectly scattered" particles (up to 90% in the case of 60 g·cm^{-2} shielding) and especially due to "border-scattering" region (Figure 3.1b). Also, most of the backscattered particles come from this region. The reason is an increase in "actual" shielding thickness in the "side-scattering" region comparing to "nominal" shielding thickness (see figure 4.10). The contribution of "indirectly scattered' particles has been demonstrated using ring sources for shielding irradiation. According to author knowledge, this configuration has not been ever used before.

Calculations with ring sources also show, that while the radiation dose is almost the same in the shielding spheres with the same "nominal" thickness and different inner radii, the contribution to the net dose equivalent due to direct-, side- and border-scattering regions differs. This shows how important is the spacing between phantom and shielding and configuration of the shielding. Also, these calculations show the importance of spherical geometry setup for radiation dose calculations, especially in the case of GCR. The assessment of the dose with shielding function and depth-dose curves, calculated using slab geometry setup, exclude "side-scattering" particles due to methodology assumption. Thus, the optimal shielding of 30 g·cm^{-2} obtained in this research is a more realistic value than 20 g·cm^{-2} reported recently by Slaba et al., 2017 and has a better background. Moreover, the same work by Slaba et al., 2017 predicts local minimum only for 1 mm thick water detector, while there is no minimum for water slab with the thickness of 30 cm, which is a more realistic simplification for astronauts phantom.

The value of 30 g·cm^{-2} is also found to be a border value for comparing the radiation environment inside a spacecraft on the ISS orbit and in the interplanetary space. If the average spacecraft shielding is more than 30 g·cm^{-2}, the radiation environment inside a spacecraft is mostly crated with “high-energy” GCR. It is similar on the ISS orbit during solar minimum and in the interplanetary space during solar maximum. If the shielding is less than 30 g·cm^{-2} dose due to TR and “low-energy” GCR significantly contribute to the dose equivalent and the “identity” between flight on the LEO and interplanetary flight is significantly reduced. However, the average ISS shielding estimations give the value of ≈30 g·cm^{-2}. Together with the results of this work, it allows the application of the current and future ISS radiological experience for radiation analysis for crewed missions to the Moon and Mars. There is a number of advantages for radiological studies on LEO comparing to on-ground experiments. For both the ISS orbit and interplanetary flight, there is a similar radiation composition inside the spacecraft, similar dose rates, and similar synergetic effect of radiation exposure, micro-gravitation, and hypomagnetic conditions. The potential duration of the experiments can be comparable to the duration of the flight to Mars and can be long enough for genomic instabilities studies. The differences in the radiation environment inside the spacecraft in the interplanetary space outside the Earth's magnetosphere and on the ISS orbit could potentially be reduced by optimizing the spacecraft shield thickness and composition and by choosing an appropriate orbit.

Although results in the section 4.2 indicate, that the methodology of radiation dose calculation with depth-dose curves and shielding functions could not be used for GCR radiation dose assessments in the case of shielding thickness over 30 g·cm^{-2}, this method is still a powerful tool to assess radiation doses due to most of SEP and TR. The lower calculation time, comparing to Monte-Carlo calculations, motivated us to calculate depth-dose curves for trapped protons, trapped electrons, and GCR on the ISS orbit in 2004-2005, during the second session of the MATROSHKA-

R experiment. The GEANT4 Monte-Carlo code (version 10.00.P02) was used to simulate particle propagation through double-layer aluminum-water shielding and calculated the energy deposition in a 1 mm detector water layer. The calculated depth-dose curves can be used with shielding-and-composition functions to calculate the radiation dose at the point of interest.

These depth-dose curves were used to calculate the radiation dose distributions at the surface of the spherical water phantom during the second session of the MATROSHKA-R experiment. The simulation results are in good agreement with the experimental data on the absorbed dose distribution. The difference is likely due to the use of the AP8 model that gives proton fluxes for the previous solar cycle, and due to mismatches in the phantom orientation inside the module and the exclusion of other modules from the simulation geometry. Trapped protons constitute a major contribution to the absorbed dose. Variations in the trapped proton dose are determined from shielding variations in low-thickness regions.

GCR give a 19-36% contribution to the net absorbed dose. There is a 6% variation in GCR dose at the phantom's surface. The GCR absorbed dose is lower at less shielded points and higher in more shielded points. Trapped electrons are efficiently stopped by the ISS shielding and make less than a 1% contribution to the net radiation dose at any point at the phantom's surface. The calculated neutron dose is lower than in other works. This is likely due to the assumptions used in the ray-tracing method and the setup used for depth-dose curve calculations. These issues will be addressed in future works.

The good agreement between the simulation results and the experimental data verifies the applicability of the applied method for dose calculations for the ISS and other low-Earth orbit missions. For the interplanetary space, this method can be used to calculate radiation doses from solar energetic particles (SEP), as they have almost similar energy range as trapped proton radiation. The method needs to be further improved to describe and predict radiation doses from GCR radiation, especially for the interplanetary missions.

For slab shielding geometry, we demonstrate the dependence of radial energy distribution on shielding thickness and radiation particle energy. Obtained results clearly show that methodology of radiation dose calculation using ray-tracing and shielding functions can be applied only for protons with energy less then 1 GeV (energy region of SEP and trapped proton radiation) for all shielding thickness and for only thin shielding (less then $\approx$10 g$\cdot$cm^{-2} if proton energy exceeds 1 GeV (energy region of GCR). We suppose modification of the methodology to take into account "dose diffusion" and increase calculation accuracy in the near-surface layer of the water phantom. The modified method needs further development and would be improved in the future.

Chapter 6

Bibliography

Agostinelli, S. et al. (2003). "GEANT4 - A simulation toolkit". In: *Nuclear Instruments and Methods in Physics Research, Section A: Accelerators, Spectrometers, Detectors and Associated Equipment* 506.3, pp. 250–303. ISSN: 01689002. DOI: 10.1016/S0168-9002(03)01368-8. arXiv: 1005.0727v1.

Badavi, Francis F. (2014). "Validation of the new trapped environment AE9/AP9/SPM at low Earth orbit". In: *Advances in Space Research* 54.6, pp. 917–928. ISSN: 18791948. DOI: 10.1016/j.asr.2014.05.010. URL: http://dx.doi.org/10.1016/j.asr.2014.05.010.

Badavi, Francis F., John E. Nealy, and John W. Wilson (2011). "The Low Earth Orbit validation of a dynamic and anisotropic trapped radiation model through ISS measurements". In: *Advances in Space Research* 48.8, pp. 1441 –1458. ISSN: 0273-1177. DOI: 10.1016/j.asr.2011.06.009. URL: http://www.sciencedirect.com/science/article/pii/S0273117711004352.

Baiocco, G et al. (Apr. 2018). "A water-filled garment to protect astronauts during interplanetary missions tested on board the ISS". In: *Life Sciences in Space Research* 18. DOI: 10.1016/j.lssr.2018.04.002.

Ballarini, F. et al. (2006). "GCR and SPE organ doses in deep space with different shielding: Monte Carlo simulations based on the FLUKA code coupled to anthropomorphic phantoms". In: *Advances in Space Research* 37.9, pp. 1791–1797. ISSN: 02731177. DOI: 10.1016/j.asr.2006.03.007.

Barthel, Joseph and Nesrin Sarigul-Klijn (Aug. 2019). "Importance of Spherical Shell Models for Radiation Shielding Designs on Space Missions". In: *Journal of Spacecraft and Rockets* 56, pp. 1–4. DOI: 10.2514/1.A34410.

Berger, T et al. (2013). “The MATROSHKA experiment: results and comparison from extravehicular activity (MTR-1) and intravehicular activity (MTR-2A/2B) exposure”. In: *Radiat.Res.* 180.1938-5404 (Electronic), pp. 622–637. ISSN: 0033-7587. DOI: 10.1667/RR13148.1.

Cerro, Jeffrey et al. (2015). “Development of logistics for building radiation storm shelters and their operational evaluation”. In: *AIAA SPACE 2015 Conference and Exposition*. DOI: 10.2514/6.2015-4402.

Cucinotta, Francis A. et al. (2013). “How Safe Is Safe Enough? Radiation Risk for a Human Mission to Mars”. In: *PLoS ONE* 8.10. ISSN: 19326203. DOI: 10.1371/journal.pone.0074988.

Dementyev, A. V. and N. M. Sobolevsky (1999). “SHIELD - universal Monte Carlo hadron transport code: scope and applications”. In: *Radiation Measurements* 30.5, pp. 553–557. ISSN: 13504487. DOI: 10.1016/S1350-4487(99)00231-0.

Denisov, A. N. et al. (2010). “On the problem of lunar radiation environment”. In: *Cosmic Research* 48.6, pp. 509–516. ISSN: 00109525. DOI: 10.1134/S0010952510060031.

Denisov, A. N. et al. (2011). “Assessment of the radiation environment on the Moon”. In: *Acta Astronautica* 68.9-10, pp. 1440–1447. ISSN: 00945765. DOI: 10.1016/j.actaastro.2010.01.025. URL: http://dx.doi.org/10.1016/j.actaastro.2010.01.025.

Dobynde, M.I. and Y.Y. Shprits (2019). “Radiation environment created with GCRs inside a spacecraft”. In: *Life Sciences in Space Research*. URL: http://www.sciencedirect.com/science/article/pii/S2214552418300804.

Dobynde, M.I. et al. (2019). “Ray-tracing simulation of the radiation dose distribution on the surface of the spherical phantom of the MATROSHKA-R experiment onboard the ISS”. In: *Life Sciences in Space Research* 21, pp. 65 –72. ISSN: 2214-5524. DOI: https://doi.org/10.1016/j.lssr.2019.04.001. URL: http://www.sciencedirect.com/science/article/pii/S2214552418300804.

Drake, Bret G, Stephen J Hoffman, and Kevin D Watts (2009). "Human Exploration of Mars Design Reference Architecture 5.0 Addendum 2". In: *Nasa* March. DOI: 10.1109/AERO.2010.5446736.

Durante, M. and A. Kronenberg (2005). "Ground-based research with heavy ions for space radiation protection". In: *Advances in Space Research* 35.2, pp. 180–184. ISSN: 02731177. DOI: 10.1016/j.asr.2004.12.034.

Fermi, ENRICO (1949). "On the Origin of the Cosmic Radiation". In: *Physical Review* 75.8, pp. 1169–1174. ISSN: 0031-899X. DOI: 10.1103/PhysRev.75.1169. URL: https://link.aps.org/doi/10.1103/PhysRev.75.1169.

Forbush, Scott (1958). "COSMIC-RAY INTENSITY VARIATIONS DURING TWO SOLAR CYCLES". In: *Journal of Geophysical Research* 63, pp. 651–669.

Forstner, Johan L. Freiherr von et al. (2019). "Tracking and Validating ICMEs Propagating Toward Mars Using STEREO Heliospheric Imagers Combined With Forbush Decreases Detected by MSL/RAD". In: *Space Weather* 17.4, pp. 586–598. DOI: 10.1029/2018SW002138. eprint: https://agupubs.onlinelibrary.wiley.com/doi/pdf/10.1029/2018SW002138. URL: https://agupubs.onlinelibrary.wiley.com/doi/abs/10.1029/2018SW002138.

Fung, S. F. (1996). "Recent development in the NASA trapped radiation models". In: *Geophysical Monograph Series* 97, pp. 79–91. ISSN: 23288779. DOI: 10.1029/GM097p0079.

Gaza, R. (July 2018). "International Science Aboard Orion EM-1: The Matroshka AstroRad Radiation Experiment (MARE) Payload". In: *42nd COSPAR Scientific Assembly*. Vol. 42. COSPAR Meeting, F2.3–20–18.

Ginet, G. P. et al. (2013). "AE9, AP9 and SPM: New Models for Specifying the Trapped Energetic Particle and Space Plasma Environment". In: *Space Science Reviews* 179.1-4, pp. 579–615. ISSN: 0038-6308. DOI: 10.1007/s11214-013-9964-y. URL: http://link.springer.com/10.1007/s11214-013-9964-y.

Golge, S., P. M. O'Neill, and T. C. Slaba (2015). "NASA galactic cosmic radiation environment model: Badhwar - O'Neill (2014)". In: *Proceedings of Science* 30-July-20. ISSN: 18248039.

Grigoriev, A. I. et al. (1983). *Model of human body forcalculation of tissue dose.* Tech. rep. State Standart 25645.203-83.

Gustafsson, K. et al. (2010). "PHITS simulations of the Matroshka experiment". In: *Advances in Space Research* 46.10, pp. 1266–1272. ISSN: 02731177. DOI: 10.1016/j.asr.2010.05.028. URL: http://dx.doi.org/10.1016/j.asr.2010.05.028.

Hanson, Julie A, Martha Clowdsley, and Sheila Thibeault (2019). "Human Factors Ground Test Assessment and Protocol Development for Space Radiation Protection Concepts". In: *Proceedings of the Human Factors and Ergonomics Society 2019 Annual Meeting*, pp. 1782–1786. DOI: 10.1177/1071181319631243.

Hassler, Donald M et al. (2014a). "Mars' surface radiation environment measured with the Mars Science Laboratory's Curiosity rover." In: *Science (New York, N.Y.)* 343.6169, p. 1244797. ISSN: 1095-9203. DOI: 10.1126/science.1244797. URL: http://www.ncbi.nlm.nih.gov/pubmed/24324275.

Hassler, Donald M. et al. (2014b). "Mars' surface radiation environment measured with the Mars science laboratory's curiosity rover". In: *Science* 343.6169, pp. 1–11. ISSN: 10959203. DOI: 10.1126/science.1244797.

Hu, Shaowen et al. (2009). "Modeling the acute health effects of astronauts from exposure to large solar particle events". In: *Health physics* MAY. ISSN: 0017-9078. DOI: 10.1097/01.HP.0000339020.92837.61.

I. Vette, James (Jan. 1991). "The AE-8 Trapped Electron Model Environment". In: *NSSDC/WDC-A-R and S 91-24*.

ICRP (1991). "1990 Recommendations of the International Commission on Radiological Protection". In: *Annals of the ICRP* 21.1.

— (2007). "The 2007 Recommendations of the International Commission on Radiological Protection. ICRP publication 103." In: *Annals of the ICRP* 37.2-4, pp. 1–332. ISSN: 01466453. DOI: 10.1016/j.icrp.2007.10.003. URL: http://journals.sagepub.com/doi/10.1016/j.icrp.2007.10.003.

Jadrníčková, I. et al. (2009). "Variation of absorbed doses onboard of ISS Russian Service Module as measured with passive detectors". In: *Radiation Measurements* 44.9-10, pp. 901–904. ISSN: 13504487. DOI: 10.1016/j.radmeas.2009.10.075.

Kartashov, D. A. et al. (2019). "Calculation of Radiation Loads in a Space Station Compartment with Additional Protection of High-Pressure Polyethylene". In: *Cosmic Research* 57.3, pp. 169–175. ISSN: 00109525. DOI: 10.1134/S0010952519030055.

Kartashov, Dmitry and Vyacheslav Shurshakov (2018). "Analysis of space radiation exposure levels at different shielding configurations by ray-tracing dose estimation method". In: *Acta Astronautica* 144.October 2017, pp. 320–330. ISSN: 00945765. DOI: 10.1016/j.actaastro.2018.01.013. URL: https://doi.org/10.1016/j.actaastro.2018.01.013.

Kodaira, S. et al. (2014). "Verification of shielding effect by the water-filled materials for space radiation in the International Space Station using passive dosimeters". In: *Advances in Space Research* 53.1, pp. 1–7. ISSN: 02731177. DOI: 10.1016/j.asr.2013.10.018. URL: http://dx.doi.org/10.1016/j.asr.2013.10.018.

Koshiishi, H. et al. (2007). "Evaluation of the neutron radiation environment inside the International Space Station based on the Bonner Ball Neutron Detector experiment". In: *Radiation Measurements* 42.9, pp. 1510–1520. ISSN: 13504487. DOI: 10.1016/j.radmeas.2007.02.072.

Kuznetsov, N. V., H. Popova, and M. I. Panasyuk (2017). "Empirical model of long-time variations of galactic cosmic ray particle fluxes". In: *Journal of Geophysical Research: Space Physics* 122.2, pp. 1463–1472. ISSN: 21699402. DOI: 10.1002/2016JA022920.

Kuznetsov, N. V. et al. (2012). "Estimation of radiation risk for astronauts on the Moon". In: *Cosmic Research* 50.3, pp. 216–220. ISSN: 7653697. DOI: 10.1134/S0010952512030057.

Loffredo, Filomena et al. (2018). "Nomex with boron as a neutron shielding in space: Preliminary study". In: *Nuovo Cimento della Societa Italiana di Fisica C* 41.6, pp. 1–6. ISSN: 18269885. DOI: 10.1393/ncc/i2018-18220-7.

M. Sawyer, D and J I. Vette (Jan. 1977). "AP8 Trapped Proton Environment for Solar Maximum and Solar Minimum". In:

Machrafi, Rachid et al. (Apr. 2009). "Neutron dose study with bubble detectors aboard the International Space Station as part of the Matroshka-R experiment". In: *Radiation protection dosimetry* 133, pp. 200–7. DOI: 10.1093/rpd/ncp039.

Matthiä, Daniel, Thomas Berger, and Günther Reitz (2013). "Organ shielding and doses in Low-Earth orbit calculated for spherical and anthropomorphic phantoms". In: *Advances in Space Research* 52.3, pp. 528–535. ISSN: 02731177. DOI: 10.1016/j.asr.2013.03.025.

Matthiä, Daniel et al. (2013). "A ready-to-use galactic cosmic ray model". In: *Advances in Space Research* 51.3, pp. 329–338. ISSN: 02731177. DOI: 10.1016/j.asr.2012.09.022.

Mccracken, K G (2001a). "Solar cosmic ray events for the period 1561-1994 1 . Identification in polar ice , 1561-1950 correlation being less correlation is demonstrated between the recording of the cosmic radiation started and the corresponding thin nitrate layers The proton flue". In: *October* 106.2000.

— (2001b). "Solar cosmic ray events for the period 1561-1994 2 . The Gleissberg periodicity when large ¿ 30 MeV proton events with fluence greater than cm -2 were The " streaming limited for ¿ 30 MeV protons is estimated to be 6-8 x 10". In: *October* 106, pp. 599–609.

McIlwain, Carl E. (1961). "Coordinates for mapping the distribution of magnetically trapped particles". In: *Journal of Geophysical Research* 66.11, pp. 3681–3691. ISSN: 01480227. DOI: 10.1029/JZ066i011p03681. URL: http://doi.wiley.com/10.1029/JZ066i011p03681.

Mrigakshi, Alankrita Isha et al. (2013). "Estimation of Galactic Cosmic Ray exposure inside and outside the Earth's magnetosphere during the recent solar minimum between solar cycles 23 and 24". In: *Advances in Space Research* 52.5, pp. 979–987. ISSN: 02731177. DOI: 10.1016/j.asr.2013.05.007.

NASA (2015). "NASA Space Flight Human-System Standard: Crew Health". In: 1. URL: https://standards.nasa.gov/standard/nasa/nasa-std-3001-vol-1.

Norbury, John W. (2011). "Perspective on space radiation for space flights in 2020-2040". In: *Advances in Space Research* 47.4, pp. 611–621. ISSN: 02731177. DOI: 10.1016/j.asr.2010.10.012. URL: http://dx.doi.org/10.1016/j.asr.2010.10.012.

Nymmik, R. A. (1996). "Models describing solar cosmic ray events". In: *Radiation Measurements* 26.3 SPEC. ISS. Pp. 417–420. ISSN: 13504487. DOI: 10.1016/1350-4487(96)00052-2.

Nymmik, R A, M I Panasyuk, and a a Suslov (1996). "Galactic cosmic ray flux simulation and prediction." In: *Advances in space research : the official journal of the Committee on Space Research (COSPAR)* 17.2, pp. 19–30. ISSN: 0273-1177. DOI: 10.1016/0273-1177(95)00508-C.

Nymmik, R. A. et al. (1992). "A model of galactic cosmic ray fluxes". In: *International Journal of Radiation Applications and Instrumentation. Part* 20.3, pp. 427–429. ISSN: 13590189. DOI: 10.1016/1359-0189(92)90028-T.

Nymmik, R.A. (1999). "Probabilistic model for fluences and peak fluxes of solar energetic particles". In: *Radiation Measurements* 30.3, pp. 287 –296. ISSN: 1350-4487. DOI: https://doi.org/10.1016/S1350-4487(99)00065-7. URL: http://www.sciencedirect.com/science/article/pii/S1350448799000657.

— (2000). "Time lag of galactic cosmic ray modulation: conformity to general regularities and influence on particle energy spectra". In: *Advances in Space Research* 26.11, pp. 1875–1878. ISSN: 02731177. DOI: 10.1016/S0273-1177(99)01242-9. URL: https://linkinghub.elsevier.com/retrieve/pii/S0273117799012429.

Olsher, Richard H. (2006). "A practical look at Monte Carlo variance reduction methods in radiation shielding". In: *Nuclear Engineering and Technology* 38.26, pp. 225–230. ISSN: 1738-5733.

O'Neill, Patrick M. (2010). "Badhwar-O'Neill 2010 galactic cosmic ray flux model - Revised". In: *IEEE Transactions on Nuclear Science* 57.6 PART 1, pp. 3148–3153. ISSN: 00189499. DOI: 10.1109/TNS.2010.2083688.

Pelowitz, D. et al. (May 2013). *MCNP6 User's Manual.*

Petoussi-Henss, N. et al. (2010). "Conversion Coefficients for Radiological Protection Quantities for External Radiation Exposures". In: *Annals of the ICRP* 40.2-5. Ed. by C.H. Clement, pp. 1–257. ISSN: 0146-6453. DOI: 10.1016/j.icrp.2011.10.001. URL: http://journals.sagepub.com/doi/10.1016/j.icrp.2011.10.001.

Petrovay, Kristóf (2010). "Solar cycle prediction". In: *Living Reviews in Solar Physics* 7. ISSN: 16144961. DOI: 10.12942/lrsp-2010-6. arXiv: 1907.02107.

Ploc, Ondřej et al. (2013). "PHITS simulations of the Protective curtain experiment onboard the Service module of ISS: Comparison with absorbed doses measured with TLDs". In: *Advances in Space Research* 52.11, pp. 1911–1918. ISSN: 02731177. DOI: 10.1016/j.asr.2013.08.025.

Rahmanifard, Fatemeh et al. (2017). "Inferring the Heliospheric Magnetic Field Back through Maunder Minimum". In: *The Astrophysical Journal* 837.2, p. 165. ISSN: 1538-4357. DOI: 10.3847/1538-4357/aa6191. URL: http://dx.doi.org/10.3847/1538-4357/aa6191.

Reitz, Guenther et al. (2009). "Astronaut's organ doses inferred from measurements in a human phantom outside the international space station." In: *Radiation research* 171.October, pp. 225–235. ISSN: 0033-7587. DOI: 10.1667/RR1559.1.

RSA (2004). "Limitation of astronauts exposure during near-Earth space flights, Methodical Recommendations". In: ISSN: MR 2.6.1.44-03-2004.

Sato, T. et al. (2011). "Evaluation of dose rate reduction in a spacecraft compartment due to additional water shield". In: *Cosmic Research* 49.4, pp. 319–324. ISSN: 0010-9525. DOI: 10.1134/S0010952511040083. URL: http://link.springer.com/10.1134/S0010952511040083.

Sato, Tatsuhiko et al. (2017). "Recent Improvements of Particle and Heavy Ion Transport code System: PHITS". In: *EPJ Web of Conferences* 153, pp. 1–6. ISSN: 2100014X. DOI: 10.1051/epjconf/201715306008.

Sato, Tatsuhiko et al. (2018). "Features of Particle and Heavy Ion Transport code System (PHITS) version 3.02". In: *Journal of Nuclear Science and Technology* 55.6, pp. 684–690. ISSN: 00223131. DOI: 10.1080/00223131.2017.1419890. URL: https://doi.org/10.1080/00223131.2017.1419890.

Sawyer, D. M. and J. I. Vette (1976). "AP-8 trapped proton environment for solar maximum and solar minimum". In: pp. 1–9.

Schwadron, N. A. et al. (2014). "Does the worsening galactic cosmic radiation environment observed by CRaTER preclude future manned deep space exploration?" In: *Space Weather* 12.11, pp. 622–632. ISSN: 1542-7390. DOI: 10.1002/2014SW001084.

Schwadron, N. A. et al. (2018). "Update on the Worsening Particle Radiation Environment Observed by CRaTER and Implications for Future Human Deep-Space Exploration". In: *Space Weather* 16.3, pp. 289–303. ISSN: 15427390. DOI: 10.1002/2017SW001803.

Shepherd, Simon J., Sergei I. Zharkov, and Valentina V. Zharkova (2014). "Prediction of solar activity from solar background magnetic field variations in cycles 21-23". In: *Astrophysical Journal* 795.1. ISSN: 15384357. DOI: 10.1088/0004-637X/795/1/46.

Shurshakov, V. A. et al. (2014). "Study of dose distribution in a human body in international space station compartments with the tissue-equivalent spherical phantom". In: *Journal of Radiation Research* 55.suppl 1, pp. i61–i61. ISSN: 0449-3060. DOI: 10.1093/jrr/rrt220.

Sihver, L. et al. (2009). "Simulations of the MTR-R and MTR experiments at ISS, and shielding properties using PHITS". In: *IEEE Aerospace Conference Proceedings*. ISSN: 1095323X. DOI: 10.1109/AERO.2009.4839360.

Simon, Matthew et al. (2014). "Design of two radworks storm shelters for solar particle event shielding". In: *AIAA SPACE 2014 Conference and Exposition* August, pp. 1–17. DOI: 10.2514/6.2014-4473.

SINP, Skobeltsyn Institute Of Nuclear Physics (2015). *Database of Solar Energetic Particles(SEP) fluences, measured from august 1997 till 2006.* http://dec1.sinp.msu.ru/~chapai/projects/database/.

Slaba, Tony C, Christopher J Mertens, and Steve R Blattnig (2013). "Radiation Shielding Optimization on Mars". In: *Nasa/Tp–2013-217983* April.

Slaba, Tony C. et al. (2017). "Optimal shielding thickness for galactic cosmic ray environments". In: *Life Sciences in Space Research* 12, pp. 1–15. ISSN: 22145532. DOI: 10.1016/j.lssr.2016.12.003. URL: http://dx.doi.org/10.1016/j.lssr.2016.12.003.

Striepe, Scott A., Lisa C. Simonsen, and John E. Nealy (1992). "Radiation exposure predictions for long-duration-stay Mars missions". In: *Astrodynamics Conference, 1992* 29.6, pp. 1–7. DOI: 10.2514/6.1992-4584.

Szántó, P. et al. (2015). "Onboard cross-calibration of the Pille-ISS Detector System and measurement of radiation shielding effect of the water filled protective curtain in the ISS crew cabin". In: *Radiation Measurements* 82.October, pp. 59–63. ISSN: 13504487. DOI: 10.1016/j.radmeas.2015.08.007.

Tessa, C. La et al. (2009). "Estimate of the space station shielding thickness at a US-Lab site using ALTEA measurements and fragmentation cross sections". In: *Nuclear Instruments and Methods in Physics Research Section B, Beam Interactions with Materials and Atoms* 19.267, pp. 3383–3387. DOI: 101016/jnimb200906107.

Trovati, S et al. (2006). "Human exposure to space radiation: role of primary and secondary particles." In: *Radiation protection dosimetry* 122.1-4, pp. 362–366. ISSN: 0144-8420. DOI: 10.1093/rpd/ncl438.

Tylka, Allan et al. (Jan. 1998). "CREME96: a revision of the Cosmic Ray Effects on Micro-Electronics code". In: *Nuclear Science, IEEE Transactions on* 44, pp. 2150 –2160. DOI: 10.1109/23.659030.

Vette, I (1991a). "The Model Trapped Electron Environment". In: *Environment*.

— (1991b). "The NASA / National Data Space Science Trapped Radiation Environment Model Program". In:

Vuolo, Marco et al. (Aug. 2017). "Exploring innovative radiation shielding approaches in space: A material and design study for a wearable radiation protection spacesuit". In: *Life Sciences in Space Research* 15. DOI: 10.1016/j.lssr.2017.08.003.

Wilson, J et al. (2016). "3DHZETRN: A Computer Efficient GCR/SPE Shield Design Code". In: *2016 Human Research Program Investigators Workshop*, pp. 1–17.

Wilson, John W. et al. (2014). "Advances in NASA radiation transport research: 3DHZETRN". In: *Life Sciences in Space Research* 2, pp. 6–22. ISSN: 22145532. DOI: 10.1016/j.lssr.2014.05.003. URL: http://dx.doi.org/10.1016/j.lssr.2014.05.003.

— (2015). "3DHZETRN: Shielded ICRU spherical phantom". In: *Life Sciences in Space Research* 4, pp. 46–61. ISSN: 22145532. DOI: 10.1016/j.lssr.2015.01.002. URL: http://dx.doi.org/10.1016/j.lssr.2015.01.002.

Zeitlin, C. et al. (2013). "Measurements of Energetic Particle Radiation in Transit to Mars on the Mars Science Laboratory". In: *Science* 340.6136, pp. 1080–1084. DOI: 10.1126/science.1235989.

Zeitlin, C. et al. (2019). "Comparisons of High-Linear Energy Transfer Spectra on the ISS and in Deep Space". In: *Space Weather*. ISSN: 15427390. DOI: 10.1029/2018SW002103.

Zharkova, V. V. et al. (2015). "Heartbeat of the Sun from Principal Component Analysis and prediction of solar activity on a millenium timescale". In: *Scientific Reports* 5.April, pp. 1–11. ISSN: 20452322. DOI: 10.1038/srep15689. URL: http://dx.doi.org/10.1038/srep15689.

Zirakashvili, V.N. (2014). "Cosmic ray propagation and interactions in the Galaxy". In: *Nuclear Physics B - Proceedings Supplements* 256-257. Cosmic Ray Origin

– Beyond the Standard Models, pp. 101 –106. ISSN: 0920-5632. DOI: `https://doi.org/10.1016/j.nuclphysbps.2014.10.012`. URL: `http://www.sciencedirect.com/science/article/pii/S0920563214002060`.